Chapter 4

Modal analysis technique and experimental procedure

4.1 Introduction

In this chapter, the general theory and techniques used in the modal analysis of structures are first described. The experimental work and procedures of obtaining the modal parameters of the model concrete slab are then explained in detail. The preparation of the experiments is described in Chapter 3 and the results are presented in Chapter 5.

4.2 Modal analysis technique

Modal testing and analysis can be used to achieve a complete dynamic description of a structure. The method involves exciting the structure and measuring its response in terms of displacement, velocity, or acceleration, the latter being the most common measurement. This and the force signal are then Fourier transformed into the frequency domain, from which frequency response functions (also called transfer functions) are established. The frequency response function (FRF) is analysed to find the natural frequencies, mode shapes, and the system parameters of equivalent mass, stiffness, and damping ratio. In this section, the underlying theory and signal analysis techniques used to obtain the FRFs are discussed.

4.2.1 Underlying theory

The frequency response of a system can be represented in terms of: (1) modulus and phase angle against frequency, (2) real and imaginary components of response with varying frequency, or (3)

vector diagram of the real component versus the imaginary component of the response. The first of these is most commonly used in modal analysis of structures, as described below.

A multi degree of freedom system can be represented as n equivalent SDOF systems [Craig (1981)]. For a SDOF system, the equation of motion under harmonic force $F(t) = pe^{iwt}$ is given by:

$$m\ddot{u} + c\dot{u} + ku = pe^{iwt} \tag{4.1}$$

the solution of which can be derived in the usual way to give the amplitude of response as:

$$X = H(\omega)\frac{p}{k} \tag{4.2}$$

Here, H(ω) is known as the *complex frequency response* where:

$$H(\omega) = \frac{1}{1 - r^2 + i2\zeta r} \tag{4.3}$$

with

$$r = \frac{\omega}{\omega_n} \qquad \omega_n = \sqrt{\frac{k}{m}} \qquad \zeta = \frac{c\omega_n}{2k}$$

The amplitude of the response, X, can be expressed as: [Rao (1995)]

$$X = X_m e^{i\phi} = X_m \cos\phi + iX_m \sin\phi \equiv X_R + iX_I \tag{4.4}$$

where X_m, X_R, and X_I denote the magnitude, the real, and the imaginary parts of X respectively. These are:

$$X_R = \frac{p}{k}\left\{\frac{1 - r^2}{(1 - r^2)^2 + (2\zeta r)^2}\right\} \tag{4.5}$$

$$X_I = -\frac{p}{k}\left\{\frac{2\zeta r}{(1 - r^2)^2 + (2\zeta r)^2}\right\} \tag{4.6}$$

$$X_m = \sqrt{X_R^2 + X_I^2} = \frac{p}{k}\left\{\frac{1}{\sqrt{(1 - r^2)^2 + (2\zeta r)^2}}\right\} \tag{4.7}$$

The phase angle ϕ can be obtained as:

$$\tan\phi = \frac{X_I}{X_R} = \frac{2\zeta r}{1 - r^2} \tag{4.8}$$

This implies that the response can be expressed as

$$u(t) = u_R(t) + iu_I(t) \equiv (X_R + iX_I)\, e^{i\omega t} = X_m e^{+i\phi} e^{i\omega t} = X_m e^{i(\omega t + \phi)} \tag{4.9}$$

where $u_R(t)$ is in phase with the applied force and $u_I(t)$ lags behind the applied force by 90°. The total response lags behind the applied force by an angle ϕ, as shown in figure 4.1 [Rao (1995)]. The response of the system can be represented in the time domain or the magnitude of the response

can be represented in the frequency domain. The phase angle can also be plotted as a function of frequency ratio. In the experimental testing, the peak amplitude of response occurs at the condition of resonance (i.e. r=1) giving:

$$X_{peak} = \frac{1}{2\zeta}\frac{p}{k} \tag{4.10}$$

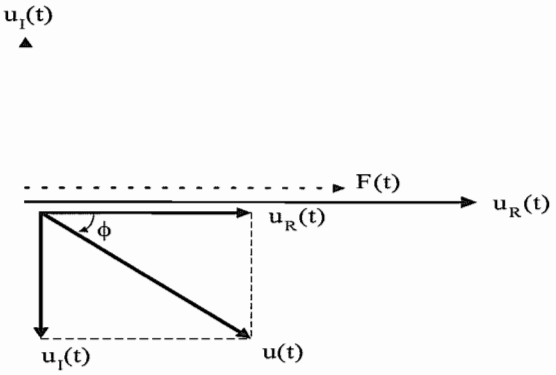

Figure 4.1: Plot of the response lagging behind the force

4.2.2 Fourier analysis of signals

Signal processing is required in modal analysis to represent the response of the system, under a known excitation, in a convenient form. Often, the time-response of a system will not give much useful information. However, the frequency-response will show one or more discrete frequencies, around which the energy is concentrated. The process of converting the analogue time-domain signal into a digital frequency-domain signal is carried out inside a spectrum analyser, where the energy of a signal is separated into various frequency bands through a set of filters. The method used is called the fast Fourier transform (FFT), which uses the Fourier analysis as explained below.

Any signal, $x(t)$, which is periodic over an interval, T, can be decomposed into a constant part and an infinite series of harmonic force contributions. When superimposed, these result in the original total time signal function. This harmonic decomposition results in a Fourier series for the signal as follows [Ewins(1984)]:

$$x(t) = \sum_{-\infty}^{\infty} X_n e^{i\omega_n t} \tag{4.11}$$

where

$$X_n = \frac{1}{T}\int_0^T x(t)e^{-i\omega_n t}dt \tag{4.12}$$

in which ω_n is the fixed repetition frequency of the excitation corresponding to the period T, and the integer i is the index number of the harmonic components. The frequencies of the harmonic

components are multiples of the frequency ω_n. By letting $T \to \infty$, equation 4.11 becomes an integral, so that for a continuous function we get the Fourier transform pair:

$$x(t) = \int_{-\infty}^{\infty} X(\omega) e^{i\omega t} d\omega \tag{4.13}$$

and

$$X(\omega) = \frac{1}{2\pi} \int_{-\infty}^{\infty} x(t) e^{-i\omega t} dt \tag{4.14}$$

In most practical applications, a signal is discretised by taking a section and dividing it into J discrete points (at $t = t_k$, $k = 1, J$). The Fourier representation of the section is then:

$$x(t_k)(= x_k) = \sum_{n=0}^{J-1} X_n e^{ik(2\pi/J)n} \tag{4.15}$$

where

$$X_n = \frac{1}{J} \sum_{k=1}^{J} x_k e^{-ik(2\pi/J)n} \qquad n = 1, J \tag{4.16}$$

Equation 4.15 is known as the discrete Fourier series of the signal and equation 4.16 is known as its discrete Fourier transform (DFT). This is the form of Fourier analysis most commonly used in digital spectrum analysers [Ewins (1984)]. It can be computed very efficiently using the fast Fourier transform (FFT) algorithm, which eliminates most of the repetition in the calculation of a DFT and permits much more rapid computation [Oppenheim et al. (1983)].

For modal analysis tests, there will usually be two separate signals entering the analyser at two input channels. In the Advantest spectrum analyser, these time-domain signals will be of force, X_a, and response, X_b, measurements. FFT is then carried out in the analyser to give the auto-power spectra, G_{aa}, for force and, G_{bb}, for the response, where:

$$G_{aa} = X_a^{\star}(\omega) \cdot X_a(\omega) \tag{4.17}$$

$$G_{bb} = X_b^{\star}(\omega) \cdot X_b(\omega) \tag{4.18}$$

Also, a complex function, G_{ab}, is calculated which is the cross-spectrum of channels a and b:

$$G_{ab} = X_a^{\star}(\omega) \cdot X_b(\omega) \tag{4.19}$$

From these calculations, three parameters can be plotted, which represent the modal analysis of the tested system.

- Transfer function (FRF) magnitude: The FRF is defined as:

$$H_{ab} = \frac{G_{ab}}{G_{aa}} \left(\equiv \frac{X_b(\omega)}{X_a(\omega)} \right) = X_R + iX_I \qquad \text{(see equation 4.4)} \tag{4.20}$$

It is common to plot the magnitude of the transfer function $\left(|H| = \sqrt{X_R^2 + X_I^2}\right)$ against frequency, from which values for peak frequency and damping can be derived (see equation 4.7).

- FRF phase angle: The phase plot is derived by:

$$\phi = \tan^{-1}\left(\frac{X_I}{X_R}\right) \qquad \text{(see equation 4.8)} \tag{4.21}$$

This is used in conjunction with the transfer function magnitude. At points of resonance, a sharp change in phase angle is observed.

- Coherence function: This function is utilised to check measurement reliability. It is a measure of the amount of response which is directly due to the imposed excitation, given by:

$$\Upsilon_{ab} = \frac{G_{ab}^{\star} \cdot G_{ab}}{G_{aa} \cdot G_{bb}} \tag{4.22}$$

Coherence always takes a value between 0 and 1. The closer the coherence function is to 1, the stronger the cause-effect relationship between input and output.

4.2.3 Related topics in signal analysis

In the Fourier transformation of any signal, there is a basic relationship between the *sampling duration*, T, the number of discrete values, J, the *sampling rate*, f_s, and the *frequency resolution* $\Delta f = \frac{1}{T}$. The range of the spectrum is 0-f_{nyq}, where f_{nyq} is the *Nyquist frequency* given by: $f_{nyq} = \frac{J}{2T}$. As the size of the transform, N, is generally fixed for a given analyser at a power of 2 (256, 512, 1024, etc.), f_{nyq} and Δf are determined solely by the sample time length, T. This fact introduces constraints and discretisation approximations, which may lead to errors. Hence, the need to limit the length of the time history. Some important features used to reduce these errors are:

Aliasing: This is the misrepresentation of the original analogue signal during digitisation. If the sampling rate is too slow, the digital representation will cause high frequencies to appear as low frequencies (figure 4.2). The problem can be avoided by maintaining the sampling rate below the Nyquist frequency, which is twice the highest frequency of interest.

Leakage: This problem arises if the finite length of the time-history does not coincide with the assumption of periodicity of the signal. Figure 4.3 illustrates this fact, where for 4.3(a), the signal is perfectly periodic in the time window, giving an accurate spectrum at the frequency of the sine wave. In figure 4.3(b), for the same wave, this periodicity assumption is not valid

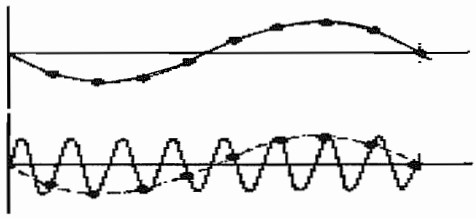

Figure 4.2: An example of Aliassing

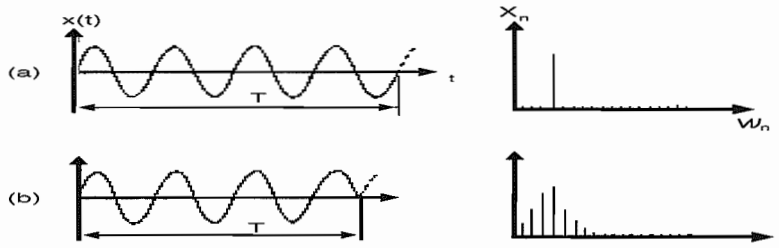

Figure 4.3: Sample length and leakage of spectrum

and the implied discontinuity causes the spectrum to be inaccurate. Energy has 'leaked' into a number of spectral lines close to the true frequency. Leakage can be corrected by the use of a window function as described below.

Windowing: This involves multiplying the original signal by a prescribed time function prior to performing the Fourier transform. This forces the signal to be zero outside the sampling period, hence reducing leakage. There are many types of windows and their use depends on the original signal. Hanning or rectangular windows are commonly used for continuous signals, while exponential windows are most effective for transient vibration applications.

Averaging: Generally, it is necessary to perform an averaging process, involving several individual time records, before a result is obtained which can be used with confidence. The two major considerations, determining the number of required averages, are the statistical reliability and the removal of external noise from the signals, hence improving coherence.

4.3 Review of modal tests on floors

This section reviews techniques and types of floor vibration tests that have been conducted, which are seen to become more complex with the improvements in technology. Initially, the most popular and easy method of exciting a floor was by the use of a heeldrop (see section 2.3), [Wiss and

Parmelee (1974), Allen and Rainer (1976), Becker (1980), Murray (1981), Allen (1990b)]. Pernica and Allen (1982) also used footsteps and a car to excite a carpark floor. Bachmann (1992b) used exercising as an excitation source in a gymnasium, where the activity rate was controlled.

Osborne and Ellis (1990) performed tests on a composite floor before and after installation of services and false floors. Their tests were in the form of heeldrop, walking, and jumping, where the floor performance was also subjectively rated. In addition, they used a rotating-mass shaker [Hudson (1964)], in which the forcing frequency could be controlled and the force input measured.

There have also been reports of experiments where the responses of structures have been measured while in use. Pernica (1983) measured the vibration response of a grandstand in a sports arena during a three hour rock concert, in order to determine the effects of audience loading, such as dancing and hand-clapping. Several studies have also been conducted on footbridges while in use [Wheeler (1982), Bachmann (1992a)]. Ellis et al. (1994) measured the response of a grandstand during a football match, in which the severe vibrations could be observed visually.

Recently, there has been a trend towards more accurate means of vibration testing, where the force input can be measured. Maguire and Severn (1987) and Caverson et al. (1994) used impact hammer testing to excite various structures. A spectrum analyser was used to obtain the transfer function, from which accurate measurements of frequency and damping were made. Pavic and Waldron (1996a) presented guidelines for the use of instrumented hammers to achieve more accurate results. Falati (1996) and Pavic et al. (1997) used electromagnetic shakers to excite floor slabs, where excitation frequency and amplitude could be controlled. Here, it was possible to impose continuous dynamic loading of known amplitude, giving better response and coherence.

The following sections outline the experimental testing programme on the model post-tensioned concrete floor, in which most of the above mentioned tests: hammer, shaker, heeldrop, and walking, were used and results analysed accordingly.

4.4 Initial setup procedure

Before commencement of vibration testing on a floor slab, careful preparation is needed. Certain quality assurance guidelines are available [DTA (1993), ISO7626/5 (1994)] of which some have been modified for civil engineering use [Pavic et al. (1997)]. The experiments explained herein follow these guidelines closely, which are described in order as: the preparatory phase, the exploratory phase, the measurement phase, and the data analysis and modal parameter estimation phase. The preliminary

preparation and exploratory phases are outlined in this section. Figure 4.4 shows an overview of the complete experimental setup, including the loading and measurement instrumentation for the shaker and hammer testing techniques.

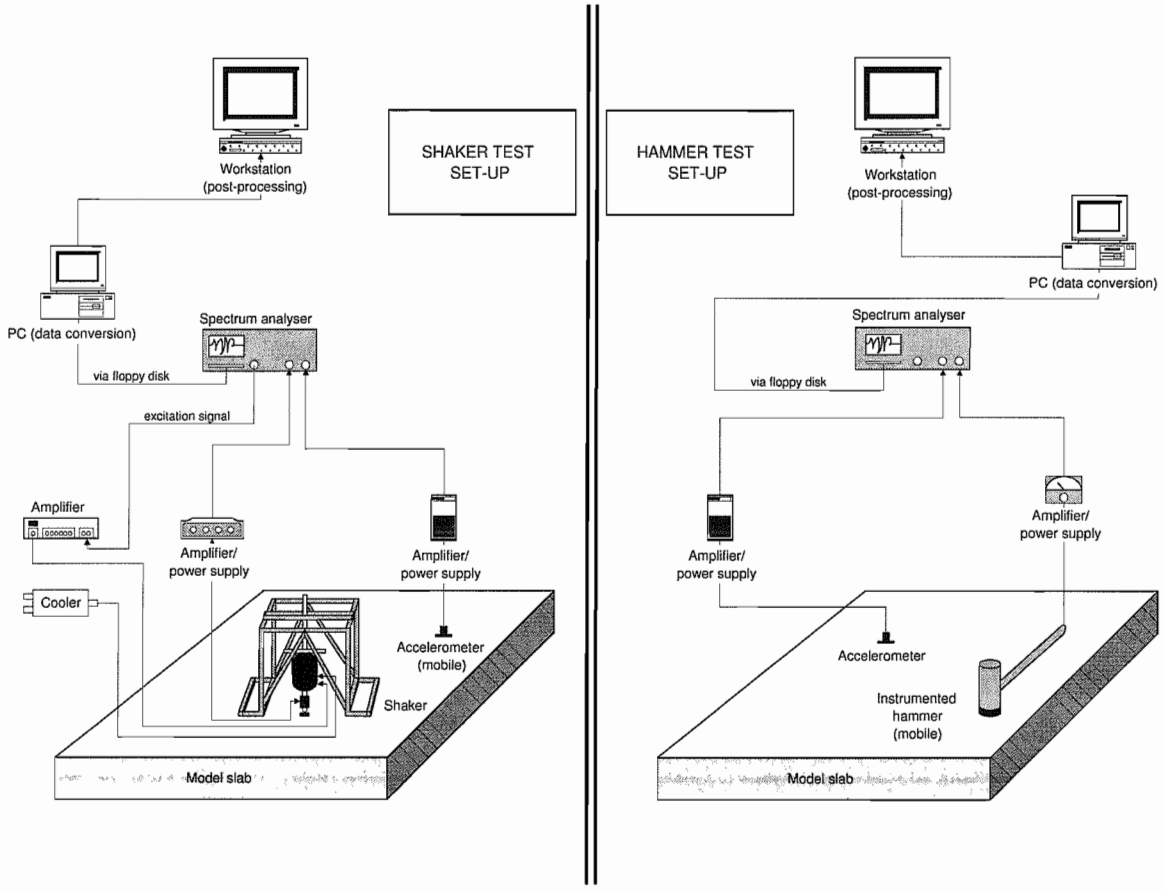

Figure 4.4: Overview of experimental setup for shaker and hammer tests

4.4.1 Location of grid points

In field testing, the floor slab under investigation is inspected and a representative panel on the structure is chosen, which exhibits the most symmetry and whose boundary conditions can easily be identified. In most cases, it may be necessary to test a few such panels and select the one that gives the best and most critical results. This test panel is then divided into a grid of equally spaced points, typically 1.5 to 2m apart. The experiment is then performed on the panel, the procedure being slightly different depending on the excitation source used, as described in section 4.5.

Under laboratory conditions, more control is available with regard to the symmetry, size, and boundary conditions of the test specimen. Also, the grid points can be much closer to each other, giving more accurate results of response and better mode shape representation. In the case of the

experimental model slab, the gridline layout is shown in figure 4.5, chosen to have the grid points closer together at the area of maximum response (i.e. the centre of the slab). The closeness of the grid points is designed to give more results, hence leading to a more accurate assessment of slab behaviour.

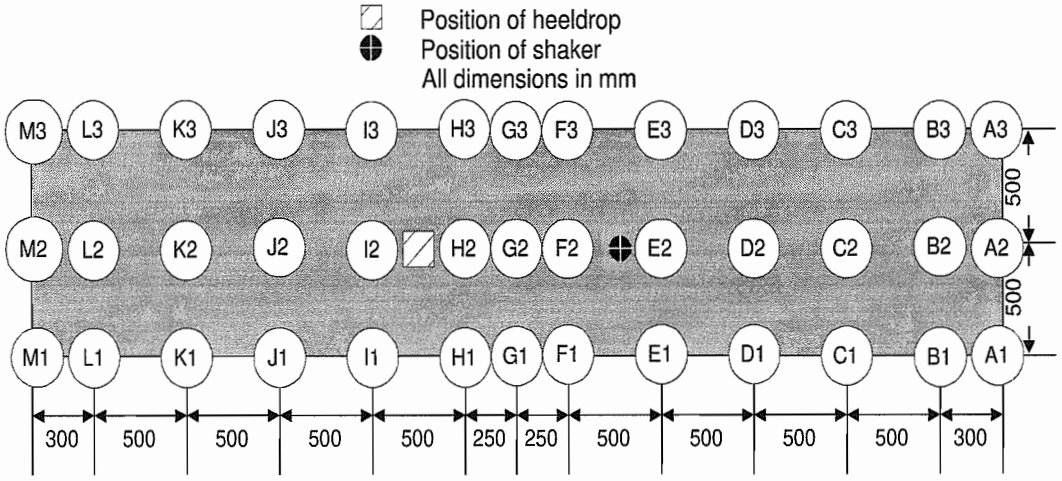

Figure 4.5: Layout of experimental grid points on the model slab

4.4.2 Location of loading

In cases where the excitation source is stationary, it is very important to apply the imposed dynamic load at a point where all desirable natural frequencies of the structure are excited. For field experiments, this point can be found by trial and error and special care is taken not to apply the load at a node. With the experimental model slab, due to the simplicity of the setup, it was easy to predict where the nodes would occur. Hence, the shaker loading frame was placed at a point where the first three natural frequencies were excited (see figure 4.5).

4.4.3 Location of measurement instrumentation

As described in section 3.3, the vibration measuring instrumentation consisted of one accelerometer (two for measuring phase), one load cell, and a spectrum analyser. In the case of shaker testing, the loading frame was stationary on the slab and the accelerometer was moved from point to point throughout all grid points. During the hammer test, it was easier to move the hammer and keep the accelerometer stationary, where it was not near a node. With the other loading types, such as heeldrop, either option could be adopted. However, as the model slab was small, it was decided that the loading was to be applied at a stationary point near the slab centre, and the accelerometer

be moved through the grid points. The actual procedure for each of the loading types is described in more detail in section 4.5.

4.4.4 Preliminary tests

Before the core of the experimental programme on the model slab was carried out, two preliminary tests were conducted with the aim of equipment familiarisation. These tests were carried out on a dance floor and an Edwardian building, as described briefly below.

Tests on an existing dance floor

The floor under inspection was *'The Longroom'* of New College in Oxford, currently being used as a dance floor. On its refurbishment into a dance-room in the early 1960s, the original floor was found to have vibration problems and limitations had been imposed on the number of people allowed to dance in the room. The tests carried out were aimed at determining the vibration characteristics of this floor. Full results of this investigation are explained in detail in [Falati (1996)]. The following is a brief summary of the test procedures.

Figure 4.6 shows the layout of the Longroom floor, including the timber beams supports and recent stiffening by a steel girder. A typical panel was chosen, which would exhibit the most symmetry, and the experiments were conducted on this panel. Limited tests were performed on the two adjacent panels in order to gain an idea of floor continuity.

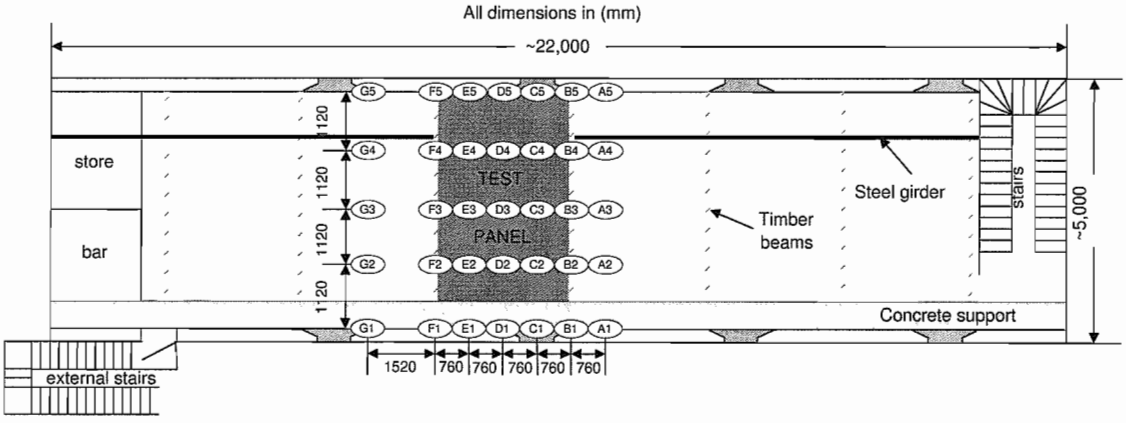

Figure 4.6: Plan of Longroom floor showing main test panel and grid points

The main aims of these tests were the commissioning of the shaker loading frame and the overall sequence of the experimental procedure. Hammer testing was also carried out and comparisons

between the hammer and shaker results were made, in order to gauge the viability of the shaker loading frame. Figure 4.6 also shows the grid points on the main test panel. The shaker was positioned at point $D3$ and during hammer testing, the accelerometer was also stationary at $D3$. The tests were carried out at night to minimise vibration interference from outdoor activities.

Table 4.1: Summary of results from Longroom tests

	Mode 1		Mode 2	
Modal property	**Hammer**	**Shaker**	**Hammer**	**Shaker**
Natural frequency (Hz)	25.94	25.68	31.83	32.00
Damping (% critical)	5.47	6.19	3.11	3.51

A summary of the damping and the natural frequency results for this floor is illustrated in table 4.1, which shows good agreement between hammer and shaker tests. Furthermore, the shaker tests were seen to give more accurate data with better coherence [Falati (1996)]. Overall, the tests were satisfactory and the shaker frame gave excellent preliminary results.

Vibration transmission tests inside an old building

The building under consideration was the *'Jenkin Building'* of Oxford University, built in 1908. It consists of three floors and a basement with footing foundations on Oxford Clay. Figure 4.7 shows an outside view of this building. A proposal was made in 1996 to establish an earthquake vibration testing laboratory on the ground floor. It was hence necessary to determine the viability of such a proposal by testing the vibration transmission throughout the building, to gauge whether the ensuing vibrations would be annoying to the occupants. The tests were carried out using the shaker loading frame and the responses were measured at various points throughout the building.

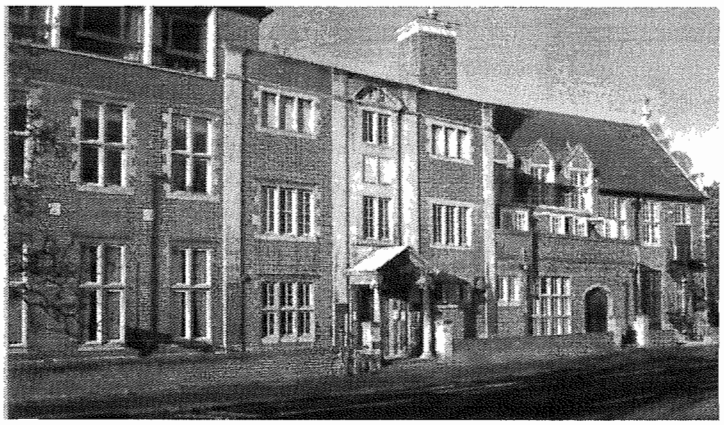

Figure 4.7: An outside view of Jenkin building

The shaker was positioned directly above one of the brick piers supporting the suspended ground floor, so that the vibration was transmitted through the foundation to the underlying soil. This would accurately represent the load path when the proposed earthquake laboratory is in operation. The accelerometer positions were near offices and vibration sensitive areas of the building, as well as near walls and columns. Also, the response at the base of the pier, on which loading was being applied, was measured to gauge the proportion of the applied load which was actually being transmitted to the foundations. It was found that this fraction was very high. The tests were conducted at night when the building was empty of occupants, hence ensuring minimum interference.

In general, it was found that due to the low relative excitation amplitude imposed by the shaker, transmission levels were small, although at places just above and next to the loading, these responses were significant. The results were used in the design of the earthquake laboratory foundations, which took the form of a solid concrete block measuring 9.1m×4.2m×1.6m deep. The laboratory has now been commissioned and vibration tests are being conducted in the building with no subsequent report of annoyance to occupants. A detailed account of the laboratory can be found in [Williams et al. (1998)]. The shaker setup and experimental procedure were again found to be satisfactory.

4.5 Loading procedure

With the test equipment commissioned and the model slab designed and built, the main part of the experimental programme was carried out. The actual testing procedure was different for each type of loading, hence they are described separately below. The measurement and processing of raw data for each experiment were similar, as described in section 4.6. Note that the following would fall under the measurement phase of the quality assurance guidelines explained in section 4.4.

4.5.1 Instrumented impact hammer

In this test, the accelerometer was mainly attached to the slab at grid point $K2$, where good response in the first three natural modes was achieved (see figure 4.5). The impact hammer, containing the force transducer, was then moved successively from point to point and at each location the model floor was impacted seven times to obtain an average analysis for the particular grid point. It was found by preliminary trials that the average of the measured data became very stable after seven hammer blows and any further blows had little effect. Special care was taken to reproduce the same

force of impact for each hammer blow, although homogeneity tests showed that the magnitude of the impact force had little or no effect on the overall results (see section 5.8). Transfer function, coherence, and phase plots were obtained on the spectrum analyser for immediate analysis and checking of results. The raw data were then recorded on floppy disks for post-processing.

4.5.2 Electromagnetic shaker

The essential difference between this test and the impact hammer test was that the accelerometer, rather than the exciter, was moved from point to point on the grid, while the vibration source was stationary. This was mainly due to the bulkiness and heaviness of the shaker test rig. Preliminary reciprocity tests (see section 5.8) showed that the same results would be achieved whether the exciter or the shaker is stationary. The position of the shaker is shown in figure 4.5.

The excitation imposed was of three distinct types. Firstly, at each experimental stage, a sine sweep of 0-100Hz (resolution of 0.12Hz) was carried out and the response of the floor was measured at the first three modes of vibration. Then, to achieve more accurate results at the first mode, a sine sweep of 0-50Hz (resolution of 0.06Hz) was conducted and again the response was measured at every grid point. The number of readings at each point was restricted to seven, which was seen to give a good average of the data.

The shaker was then altered to produce a sine-wave excitation at a single frequency, equal to one of the first three natural frequencies, hence exciting the slab at only that frequency. For measurements of damping by the logarithmic decrement method, the shaker was suddenly switched off and the subsequent free vibration of the floor was measured in the time domain. More emphasis was placed on the first natural frequency of the slab, as it would generate the largest response and is within the range of human annoyance. Hence, the slab was excited at its fundamental frequency with three different loading amplitudes and the logarithmic decay at each of these was measured.

The effect of the mass of the shaker frame on the fundamental frequency of the slab was calculated to be of the order of 2%. However, to avoid any discrepencies between shaker and hammer measurements, the hammer test was conducted with the shaker frame present on the slab.

4.5.3 Heeldrop loading

This test is described in section 2.3, but its popularity has declined recently as the drawbacks of the approach have been recognised. Most obviously, the applied loading varies from test to test

and cannot be readily determined. In the case of the experimental slab, the person conducting the heeldrop weighed 75kg and was positioned on a fixed point near the centre of the slab (see figure 4.5). The accelerometer was moved from point to point and the time domain acceleration response of the floor was monitored at nine points near the slab centre. Figure 4.8 shows a typical response measured from a heeldrop loading. The effect of the mass of the person on the measured fundamental frequency was calculated to be of the order of 4%. This was reflected in the results, as shown in chapter 5.

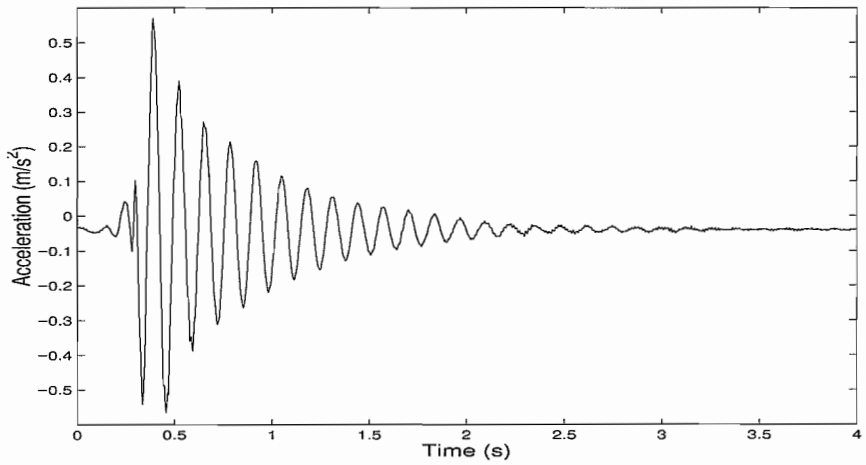

Figure 4.8: Typical response to a heeldrop measured at point $H2$ in figure 4.5

4.5.4 Human walking

For each experimental condition, human walking tests on the slab were carried out and the response measured at nine points near the slab centre (gridlines F to H in figure 4.5). The ensuing acceleration readings were averaged and compared with human perceptibility guidelines for each slab configuration. Two types of tests were conducted, vertical and horizontal walking.

In vertical walking, also described as on-the-spot walking, the person was stationary with no horizontal motion and the frequency of walking was kept to normal realistic levels of around 2Hz. A typical time history of vertical walking is shown in figure 4.9.

Horizontal walking, also described as normal or forward walking, entails the person walking on the slab with horizontal motion and changing direction at the end of the slab. While turning, the subject would try to exhibit normal walking conditions. Figure 4.10 shows a typical horizontal walking time history. The irregular part is due to the person turning, hence losing the constant momentum in his walking rate.

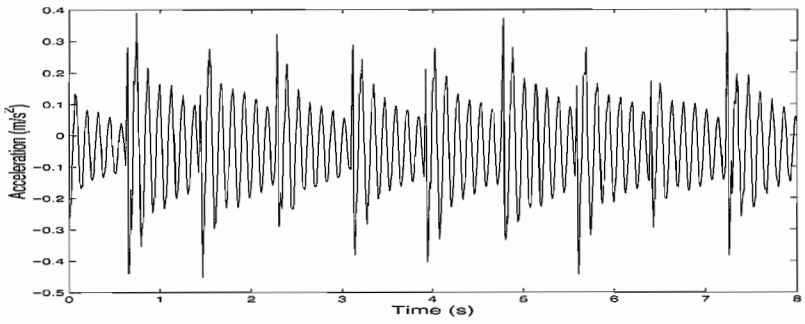

Figure 4.9: Typical slab response to vertical walking (grid point $F2$ in figure 4.5)

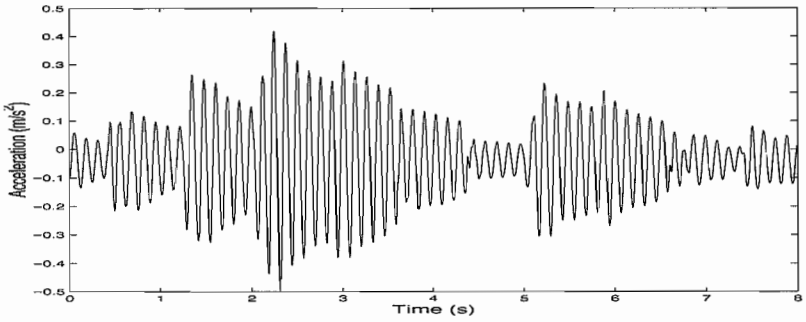

Figure 4.10: Typical slab response to horizontal walking (grid point $F2$ in figure 4.5)

4.6 Measurement procedure

The first indication of the experimental results is observed on the spectrum analyser, in the form of transfer function, phase, and coherence plots. A transfer function, as described in section 4.2, is a complex function which defines the output of the system given the input, and is basically the measured acceleration divided by the measured force at a particular point in the frequency domain. The phase plot describes the difference in phase between the force and acceleration signals. At a resonant frequency, this plot would be expected to undergo a sudden shift as the frequencies of the two signals become equal. The coherence is a measure of the accuracy of test data and a value of more than 95% is regarded as acceptable in these tests. It would be normal to accept a rather lower coherence in field testing conditions due to external vibrations other than the applied force.

Typical graphs for the transfer function, phase, and coherence, are shown in figure 4.11. The results were saved as G_{aa}, G_{bb} and G_{ab} in the frequency domain and as X_a, X_b in the time domain for further analysis. As shown in figure 4.4, these data were converted and post-processed on a network of workstations, using a suite of programs written in *Matlab*. The derivation of the floor properties, in terms of natural frequencies, damping, and mode shapes, is described in the following sections.

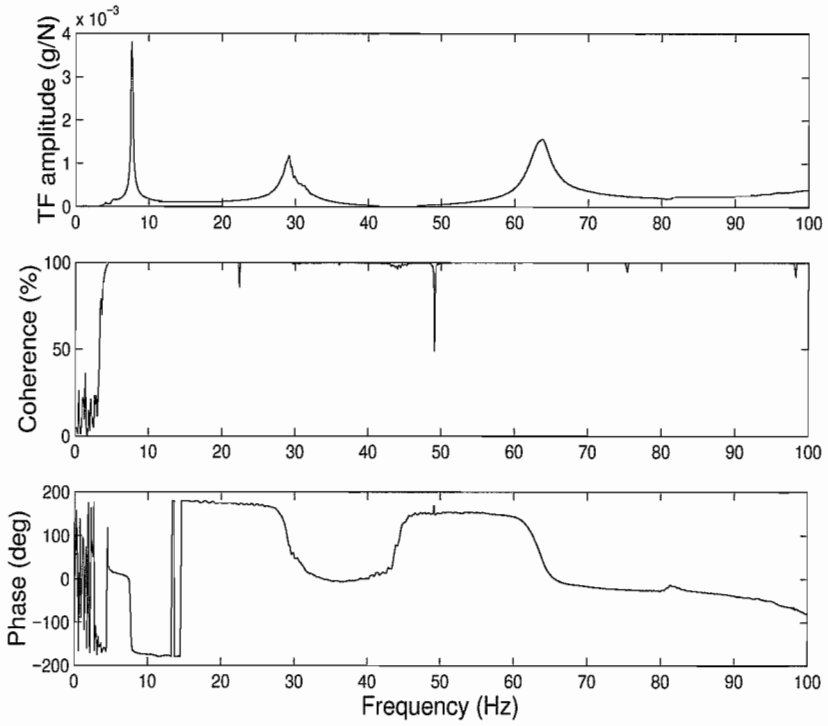

Figure 4.11: Typical plots of transfer function, phase, and coherence, taken at point $K2$

4.6.1 Natural frequencies

As shown in figure 4.11, typical test transfer functions exhibit a varying number of peaks in the frequency range. In field tests, these peaks are generally closely spaced and sometimes difficult to identify. The model slab, however, is designed as a simple structure, hence exhibiting distinct peaks at each mode. For each grid location, the first peak represents the first mode, and so on. At the first peak amplitude, the value of frequency was noted and taken as the fundamental natural frequency of the floor. This procedure was carried out for the other modes of the floor system, where each mode was represented by a corresponding resonating peak. The overall natural frequency of each mode could hence be represented as the average value of all those extracted from each grid location for that mode. In the case of the model slab, this was in most cases an average between 39 values corresponding to the 39 grid points. The results are given in section 5.3 for each slab configuration.

From single sine-wave loading at individual modes of vibration, natural frequencies were estimated from time domain data by measuring the average time between zero crossings and calculating the average frequency, which is the reciprocal of the period. In addition, a Fast fourier transform (FFT) was also performed on each reading, which agreed very closely with the calculated values. Again, in most cases, these tests were performed for all grid points giving an average of 39 individual readings for each slab configuration. The results are illustrated in section 5.3.

4.6.2 Phase between two points

These tests were carried out to determine the direction of the mode shapes. Two accelerometers were used, where one was a reference placed in position $L2$, while the second was moved from point to point on the slab (see figure 4.5). At each point, the phase difference between the two accelerometers was deduced using the spectrum analyser. The phase value for each mode at each grid location was taken at the mode's natural frequency. When the two accelerometers were in phase, a reading of -90° to +90° would be observed, whereas a reading of -90° to -180° or +90° to +180° would signal the two points out of phase. A typical phase plot between two accelerometers is shown in figure 4.12.

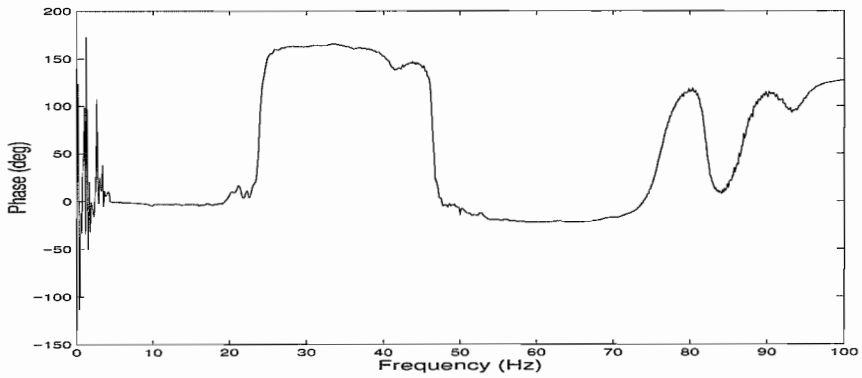

Figure 4.12: Typical phase plot with reference accelerometer on point $L2$ and second accelerometer on point $C2$ of figure 4.5

4.6.3 Mode shapes

Since acceleration is proportional to the negative of displacement at any mode, the transfer function maximum amplitude for a particular natural frequency could be used to calculate the mode shape of the floor at that natural frequency. For each mode and grid location, the transfer function maximum amplitudes were normalised to the largest value, to obtain the magnitude of the mode shape co-ordinate for that particular mode and grid point. The phase differences between the points were then incorporated, which determined the sign of the mode shape co-ordinate at each grid point. After calculating all normalised mode shape co-ordinates and their directions, it was possible to plot the mode shapes of the floor. Generally, only the first two or three modes of vibration are significant, because they are the ones most likely to be excited by ambient excitations, such as walking and jumping. They are also the most perceptible to human beings. Typical mode shape plots for the experimental slab are shown in figure 5.4 (page 96) for the first three modes.

A second possible method of obtaining mode shapes would be to excite the floor at a natural frequency and plot the normalised acceleration responses of all points, with phase differences incorporated. This method was also carried out and identical results to the above were obtained.

4.6.4 Damping ratios

Halfpower bandwidth

This method is explained in section 2.6.2. In the case of the experimental results, *Matlab* programming was used to fit a smooth spline curve over the resonant peak at the fundamental frequency. The peak of the smooth curve was then measured and damping was calculated using equation 2.35 (page 32). A typical plot using this method is shown in figure 4.13. For higher modes, the data points were seen to exhibit more scatter and hence the spline fit was not a suitable option. Here, equation 2.31 (page 32) was used and a best fit SDOF visco-elastic curve was fitted to the data, which best presented the values of frequency, damping, and stiffness at the mode. Figure 4.14 illustrates this method at the third mode of vibration.

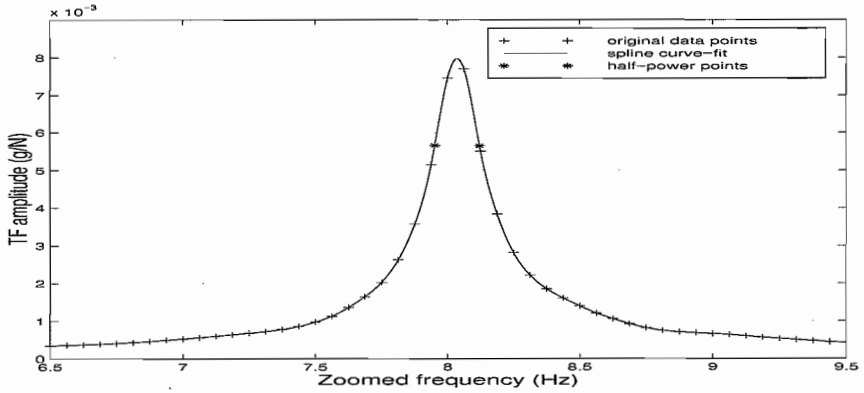

Figure 4.13: Calculation of damping ratio in frequency domain by halfpower bandwidth method (spline curve fit)

Logarithmic decrement

The logarithmic decrement, δ, represents the rate at which the amplitude of free damped vibration decreases with time, as explained in section 2.6.2. In the case of the experimental slab, the time domain acceleration response of the floor was measured either after a heeldrop or after switching the shaker off. This resulted in a response, which was of the form of an exponential decay, as shown in figure 4.15. By fitting a smooth, linear viscoelastic, exponential curve and using the logarithmic

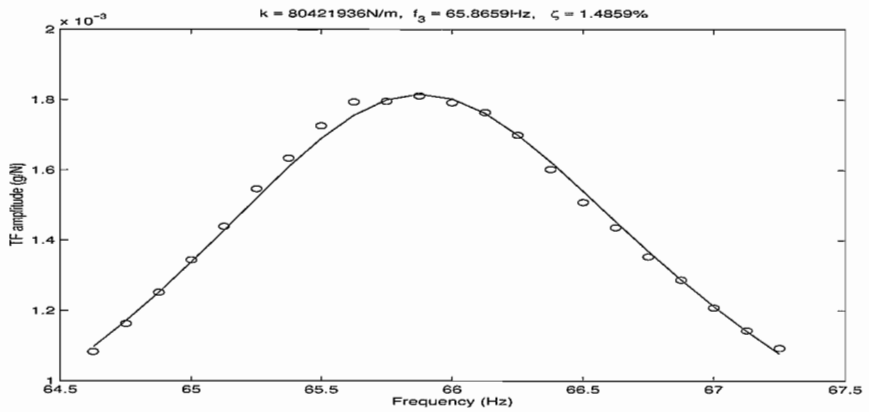

Figure 4.14: Calculation of damping ratio in frequency domain by halfpower bandwidth method (SDOF curve fit)

decrement method, the value of damping ratio at a certain grid point was obtained. It is assumed that the damping is uniform throughout the floor. To obtain better accuracy, this procedure was carried out on as many as 25 points for a given slab configuration and the average was taken, which was deemed to be the overall value of ζ for the whole floor. To calculate the value of damping for each mode separately, it was not possible to use the heeldrop test as the frequency of the input force could not be controlled. With the shaker, however, it was possible to impose a single sine load equal to the relevant natural frequency of the slab. Hence, the shaker frequency was tuned to coincide with one of the slab resonant frequencies, exciting that particular natural frequency. On switching the shaker off, it was possible to obtain a damping value for that particular mode.

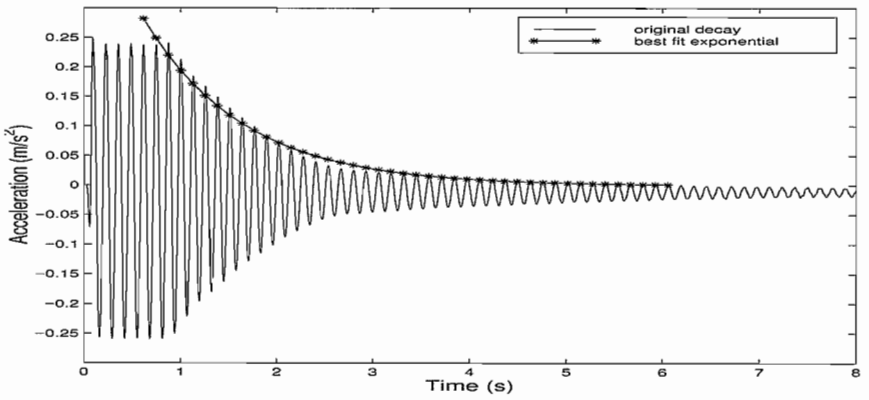

Figure 4.15: Damping ratio in time domain (logarithmic decrement method)

4.6.5 Maximum accelerations

After each alteration to the floor, a test was also carried out at which the shaker imposed a steady-state sinusoidal load at a slab natural frequency. The maximum acceleration amplitudes of the slab, at some grid points, were then measured. Responses were also measured as a result of heeldrop and walking excitations. Each acceleration reading was converted to its Root Mean Square (RMS) value for comparison with the guidelines mentioned in section 2.2.2. The results are presented in section 5.7.1 and analysed in section 6.6.1. Figure 5.5 (page 98) shows a sample acceleration of the slab when excited at its fundamental natural frequency.

4.7 Small specimen tests

During the casting process of the model slab and the visco-elastic screed, small sample specimens of the mix were taken in the form of cubes and cylinders (see section 3.5.3). The following describes the test procedure for determining the concrete material properties from these samples.

Determination of Young's modulus

Axial compression tests were carried out on two 300mm long by 150mm diameter cylinders in accordance to standard guidelines given in BS1881: Part 121 [Kong and Evans (1989)]. In each case, five loading increments were used and each of these was repeated three times to account for hysteresis losses. The tests were performed at regular intervals throughout the research programme, to obtain a record of variations over the test period. Experimental results are described in section 5.2.1.

Determination of concrete strength

As mentioned in section 3.5.1, the concrete mix for the slab was designed to have a characteristic strength, f_{cu}, of 40N/mm^2. A total of fifteen 100mm concrete cube samples were taken to confirm the actual compressive strength of the slab. The cubes were crushed in the normal way and the results are described in section 5.2.2. All cubes were seen to undergo '*normal failure*'.

Vibration tests on sample beams

Three doubly reinforced beams of 1500×200×150mm were cast during the experimental programme, as described in sections 3.5.3 and 3.6.7. The beams were tested in the laboratory to find their vibration characteristics. The purpose of these tests was to identify the changes in damping behaviour of concrete, caused by the Concredamp visco-elastic additive [Concredamp Inc. (1993)]. Figure 4.16 shows the vibration tests carried out on these beams, which were impact hammer tests using a hard tip for a large frequency range. Response measurements were taken at eleven points along the beams. These points are illustrated in figure 4.17, which also shows the location of the hammer impacts. For each test point, ten hammer blows were conducted and from the average peak fundamental frequencies, inherent damping was derived using the halfpower bandwidth method. The results of the vibration tests on the three beams are given in section 6.5.1.

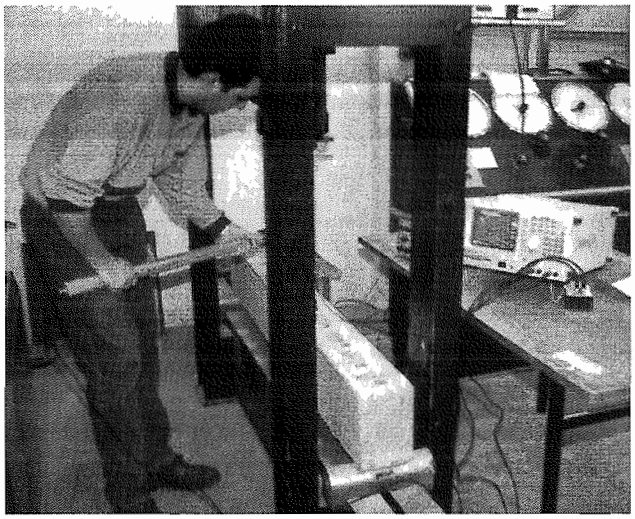

Figure 4.16: Vibration testing of sample beams by impact hammer

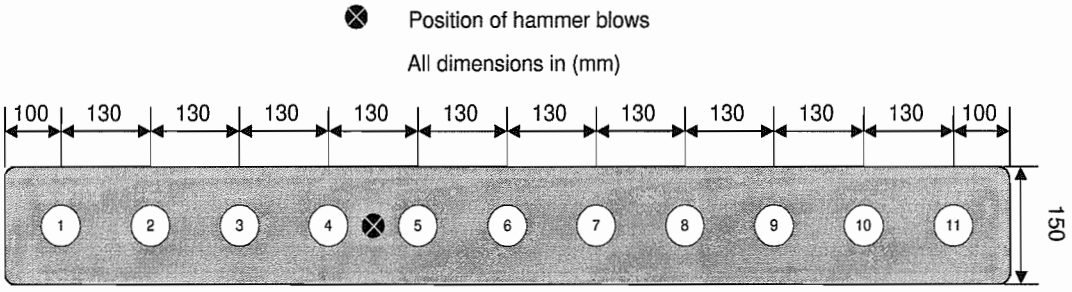

Figure 4.17: Test grid points on sample beams

Chapter 5

Experimental results

5.1 Introduction

In this chapter, the results of small specimen cylinder and cube tests are presented and the concrete properties are derived. The bulk of the chapter, however, presents summaries of the obtained values of fundamental mode natural frequency, damping, and peak accelerations for each slab stage, using the analysis techniques of chapter 4. Complete results of all tests at the first three modes are included in appendix A. In chapter 6, all the data presented here are discussed and analysed in relation to different slab conditions. Full results relating to tests with plywood TMDs and human-structure interaction are described in more detail in chapters 7 and 8 respectively.

5.2 Concrete properties

This section presents the results of tests carried out to verify the design concrete properties. The modulus of elasticity and concrete cube strengths, obtained in these tests, are compared with recommended values in BS8110 (1985), which show acceptable agreement. Factors such as creep, shrinkage, and thermal strains are ignored as the model slab is too small and the time period of testing too short for these to have any significant effect. As the properties of concrete are affected by time-dependent factors, such as stress, relative humidity, and temperatures, tests on sample cylinders and cubes were carried out regularly during the course of the experimental programme. The specimen preparation and testing techniques are described in chapters 3 and 4 respectively.

5.2.1 Modulus of elasticity

Young's modulus was derived from axial compression tests in the linear elastic region of the stress-strain graphs. As the research programme is solely concerened with serviceability loading, higher stresses at the non-linear region of the stress-strain curve were not attempted. Two cylinders were tested at regular time intervals using the procedure outlined in section 4.7. Figure 5.1 shows a typical experimental stress-strain curve. For each loading-unloading cycle, five values of Young's modulus were obtained, which over the three cycles were averaged to obtain an E value for the particular test. The derived E values for the two cylinders are plotted against time in figure 5.2. These are compared with BS8110: Parts 1 and 2 recommended values.

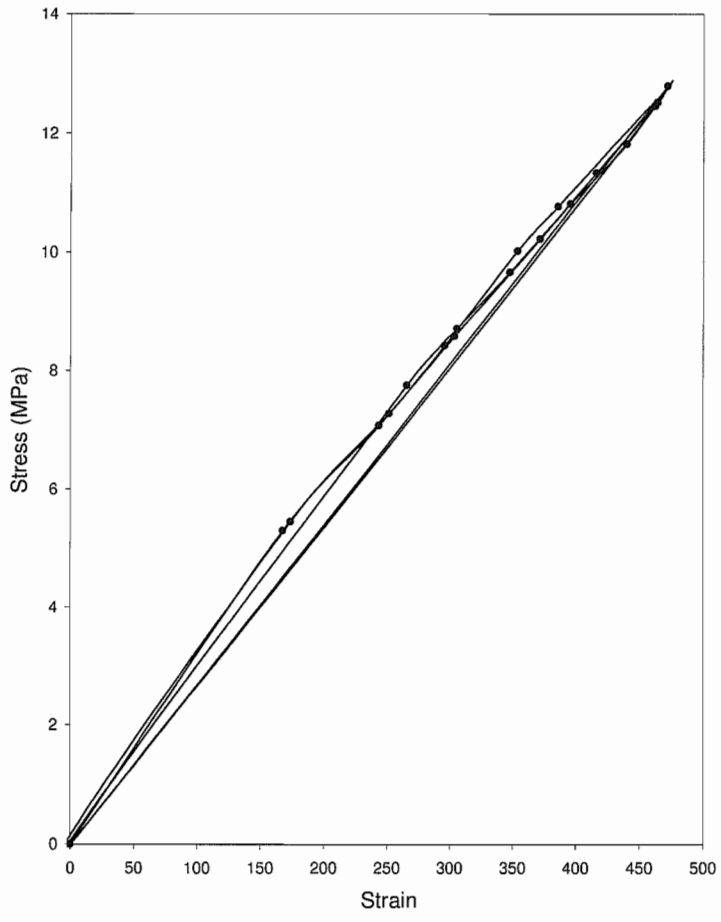

Figure 5.1: Typical stress-strain curves over three loading-unloading cycles showing hysteresis

The equation used in Part 2 for the modulus of elasticity at age t is:

$$E_{c,t} = E_{c,28}\left(0.4 + 0.6\frac{f_{cu,t}}{f_{cu,28}}\right) \qquad \text{for} \quad t \geq 3 \text{ days} \tag{5.1}$$

where the recommended values of $f_{cu,t}$ in the codes suggest a gain of strength beyond 28 days, hence affecting modulus of elasticity. BS8110: Part 1, on the other hand, assumes no increase in strength beyond 28 days. From figure 5.2 it is apparent that the experimental results fall below these two versions of the codes, but are still within the recommended range given as 22-34kN/mm^2. From the test data, a value for Young's modulus of 25.6kN/mm^2 was used in all subsequent calculations. This is the mean of the test results, all of which lie within $\pm 5\%$ of this value.

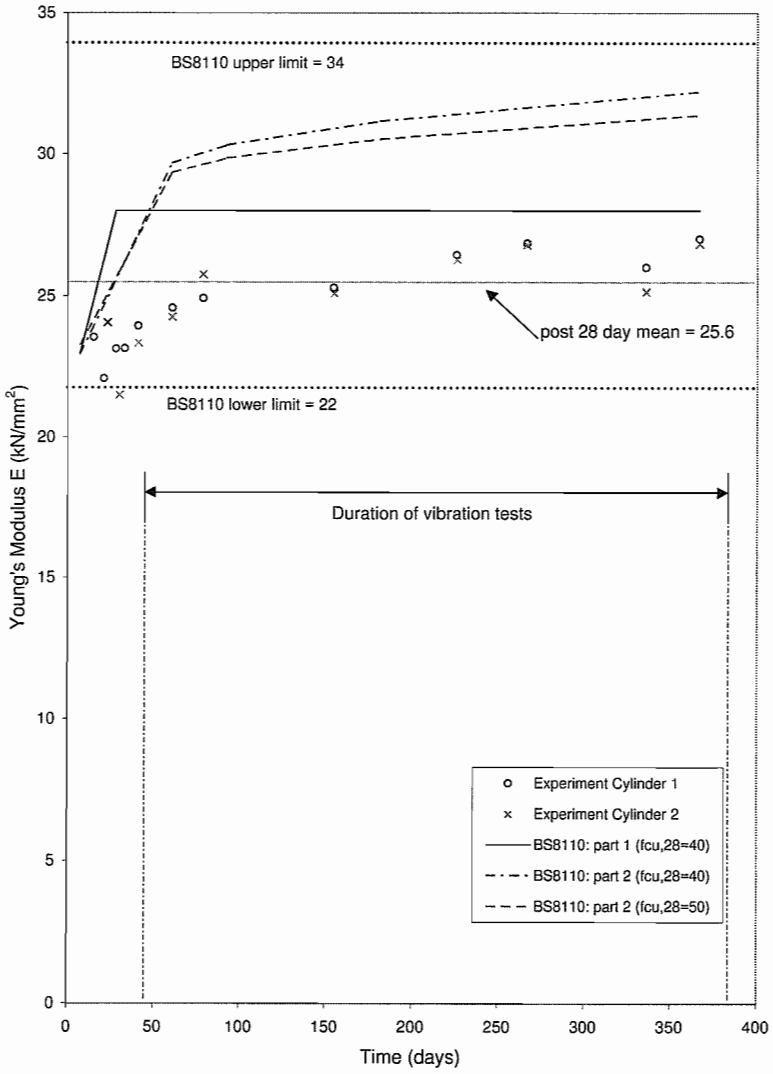

Figure 5.2: Experimental values of Modulus of Elasticity

5.2.2 Concrete cube strengths

At regular time intervals during the experimental programme, 100mm cubes were crushed to obtain values of cube strength, $f_{cu,t}$. These are plotted against time in figure 5.3. Notice that at the early stages of curing, more than one cube was crushed on the same day. Also in figure 5.3, plots of recommended values of cube strength with time from BS8110: Parts 1 and 2 are illustrated. Again, Part 1 assumes no gain in strength after 28 days. Satisfactory agreement exists between experimental values and those from the codes, particularly around the region where the design strength is between 40 and 50N/mm^2. This shows that the concrete mix has a slightly higher strength, which is close to the design target mean strength of 45N/mm^2. This is common in laboratory conditions. The average cube strength of all samples tested after 28 days was 44.8N/mm^2.

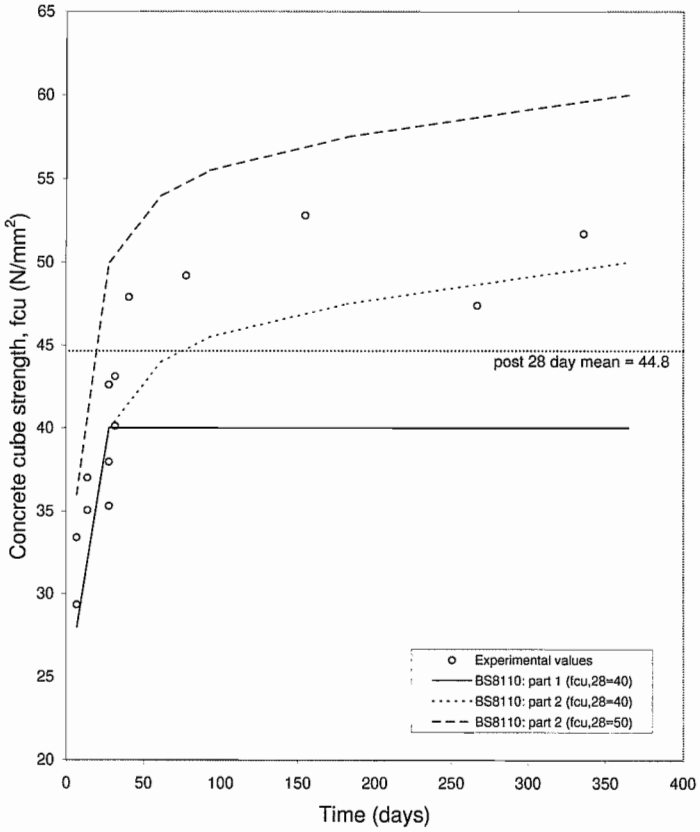

Figure 5.3: Comparison of experimental concrete cube strength with BS8110

5.3 Natural frequencies

Having derived the concrete properties, the remainder of this chapter is concerned with tests on the model slab itself. As described in chapter 4, the model slab natural frequencies were derived from both frequency and time domain data for comparison. The frequency data were in the form of FRF plots and time data were in the form of time histories.

Tables 5.1 to 5.6 show the average fundamental frequency results, obtained from frequency domain and time domain analyses, at different slab stages. Detailed results and values at higher modes are presented in appendix A, which show that the frequency domain tests were carried out at two frequency resolutions of 0.12 and 0.06Hz for accuracy (tables A.1-A.9). In general, the derived values agree well at the two frequency resolutions. Similarly, in the time domain, the slab response was measured at various loading amplitudes, excited at the natural frequencies, and the results show minimal sensitivity of natural frequency to this variation (tables A.10-A.17). Note that the results for full-height partitions are not given in the time domain, as the modes are very closely spaced making the derivation of a single natural frequency very difficult and inaccurate.

In general, it can be observed that the values obtained at the two domains agree well for a particular slab configuration. Here, second and third harmonics are considered to be too high to cause vibration problems. Hence, all further analyses are mainly concerned with the fundamental frequency of the slab, which is within the range of human sensitivity.

5.4 Damping ratios

As for natural frequency, the damping values of the slab were derived from both frequency domain and time domain measurements. The halfpower bandwidth method was used to derive the damping in the frequency-domain and the logarithmic decrement method was used for the time-domain results of shaker cut-off and heeldrop. Both these methods and their application to the experimental results are described in chapter 4. Full damping results of all tests are included in appendix A.

Tables 5.1 to 5.6 show the average fundamental mode damping results obtained using the two methods on each slab configuration. Again, in the frequency domain, two different frequency resolutions were used and the averages given were taken over a large number of points tested (tables A.18-A.26). In some cases, noticeable differences could be observed between readings from the two resolutions. Here, the value of the smaller frequency resolution is deemed to be more accurate

as the experimental points are closer together before commencement of curve-fitting. However, in most instances the readings were close and the average values taken are therefore from readings of both frequency resolution tests.

The damping values obtained from the logarithmic decrement method were seen to be influenced to a great extent by the amplitude of the applied load (tables A.27-A.34). Here, the linear SDOF visco-elastic curve, representing damping and natural frequency, was fitted at all values of amplitude between 95% and 5% of maximum response. This would give a degree of consistency to the presented results and a means of comparison between different loading amplitudes.

From tables 5.1-5.6 it is observed that the values obtained from frequency and time-domain measurements are generally in reasonable agreement for each particular slab stage. The frequency-domain results are influenced by frequency resolution and the time-domain results by amplitude of loading. It is generally agreed that with a higher frequency resolution, the results become more accurate. However, as explained in section 4.6.4, the measurement of damping in the frequency domain is prone to non-linear behaviour of the structure, making the evaluation of resonance curves difficult. In these tests, minimal non-linearity was observed at the fundamental mode and the results could be viewed with confidence (see also section 5.8). The measurement of damping in the time-domain, however, is the most common method and generally recommended [Bachmann et al. (1995)].

Table 5.1: Effect of prestress on fundamental frequency and damping

Slab configuration	**Fund. Frequency (Hz)**		**Damping (% critical)**	
	freq. domain	time domain	freq. domain	time domain
reinforced without post-tension	7.54	-	1.90	-
100kN post-tension force	7.63	7.62	1.73	1.70
175kN post-tension force	8.01	8.03	1.09	1.11
detensioned before demolishing (with screed layer)	9.16	8.98	1.84	1.82

Table 5.2: Effect of dead load on fundamental frequency and damping

Slab configuration	**Fund. Frequency (Hz)**		**Damping (% critical)**	
	freq. domain	time domain	freq. domain	time domain
100kN post-tension force with dead load of 0.25kN/m^2	7.22	7.13	1.95	2.10
175kN post-tension force with dead load of 0.25kN/m^2	7.70	7.71	1.27	1.21

Table 5.3: Effect of false flooring on fundamental frequency and damping

Slab configuration	**Fund. Frequency (Hz)**		**Damping (% critical)**	
	freq. domain	time domain	freq. domain	time domain
floor layout1 (see fig. 3.15, page 62)	7.87	7.89	1.11	1.22
floor layout2 (see fig. 3.16, page 62)	7.61	7.53	1.81	1.85

Table 5.4: Effect of stationary man on fundamental frequency and damping

Slab configuration	**Fund. Frequency (Hz)**		**Damping (% critical)**	
	freq. domain	time domain	freq. domain	time domain
one man standing near slab centre	7.92	7.65	3.80	3.88
equivalent mass of man near centre	7.69	7.66	1.41	1.49

Table 5.5: Effect of partitions (see figure 3.12, page 60, for layout) on fundamental frequency and damping

Slab configuration	**Fund. Frequency (Hz)**		**Damping (% critical)**	
	freq. domain	time domain	freq. domain	time domain
five cantilever partitions perpendicular to slab span (nos. 1-5 in fig. 3.12)	7.76	7.69	1.31	1.31
five cant. parts. perpendicular and 3 transverse to slab span (nos. 1-8 in fig. 3.12)	7.81	7.77	1.65	1.72
three parallel to slab span (nos. 6-8 in fig. 3.12)	8.00	-	1.10	-
three full-height partitions perpendicular to slab span	20.66	-	1.75	-
one full-height partition perpendicular to slab span	20.34	-	1.95	-
five cantilever and one full-height partitions	20.31	-	1.96	-

Table 5.6: Effect of visco-elastic screeds on fundamental frequency and damping

Slab configuration	**Fund. Frequency (Hz)**		**Damping (% critical)**	
	freq. domain	time domain	freq. domain	time domain
25mm thick screed of low Concredamp concentration (see section 3.6.7)	8.82	8.72	1.14	1.15
additional 25mm thick screed of high Concredamp concentration	10.14	10.15	1.17	1.33

5.5 Mode shapes

The mode shapes for each slab configuration were derived as explained in section 4.6.3. As the model slab is one-way spanning with simple supports, it exhibits beam like behaviour and its mode shapes resemble those for a simple beam. Figure 5.4 shows typical mode shapes for the first three modes of the slab when fully stressed. The non-zero end readings suggest some vertical flexibility at the supports, and may also be because the end points of measurement were not exactly on the support lines. In most instances, the addition of non-structural components did not affect the mode shapes and for each stage similar results as in figure 5.4 were obtained. The only addition which significantly affected slab stiffness, and hence mode shape, was when full-height partitions were installed. This is discussed in detail in section 6.4.1.



Figure 5.4: Typical first three mode shapes of slab

5.6 Heeldrop tests

Table 5.7 shows the derived natural frequency and damping values obtained from the exponential decay of vibrations following heeldrop loading. Time-domain frequency analysis and logarithmic decrement damping methods were used in these cases and the results agree well with comparable ones of shaker cut-off and FRF tests. Note that the damping values obtained due to heeldrop loading are high, as the decay occurs while the body of the applier is stationary on the slab. Hence, these results should be compared with those of shaker cut-off and FRF tests with a standing human present on the slab (see table 5.4 and appendix A). Also included in table 5.7, are the average peak

acceleration readings of the slab following heeldrops. These are used in some acceptibility criteria, as explained in section 6.6.3.

Table 5.7: Fundamental frequency, damping, and peak accelerations of heeldrop tests

Slab configuration	no. of tests	**Fundamental frequency (Hz)**	**Damping (% critical)**	**Peak accel. (m/s^2)**
bare slab fully prestressed	9	7.68	3.65	0.53
false floor layout 2	18	7.44	3.51	0.52
first screed layer	9	8.68	4.00	0.88
first screed layer and five cantilever partitions	9	8.59	3.72	0.97
second screed layer	13	10.02	3.22	0.85
second screed layer and false floor layout 1	12	9.95	3.18	0.67
second screed layer and false floor layout 2	8	9.82	3.30	0.83

5.7 Acceleration responses

As explained in chapter 4, the acceleration response of the slab was measured due to human walking, and due to a steady-state sine-wave excitation at the slab resonance frequency. These readings could then be checked against acceptability guidelines and the level of vibration could be rated. This procedure is described in section 6.6. In the following sections, the results obtained from the two types of loading tests are presented.

5.7.1 Excitation at resonance frequency

In this case, the acceleration response of the slab was measured as a result of imposing a steady-state excitation at the slab fundamental frequency. The acceleration was measured at the centre of the slab, where maximum response was expected. Readings were taken at nine points and converted to the Root Mean Square (RMS) values for comparison with the acceptability curves. Figure 5.5 shows a typical resonant response and its RMS acceleration value. For each case, the loading was applied at two different amplitudes for comparison (see table A.35 in appendix A). The loading amplitudes were generally small but since they were being applied at the resonant frequency, high acceleration responses were observed.

Table 5.8 shows the RMS acceleration responses, obtained for selected configurations at the fundamental mode, normalised over the loading amplitude. Similar results at the second and third natural frequencies are also given in tables A.36 and A.37 of appendix A. For the second mode, the presented values were averages of readings at 1/4 and 3/4 of slab span, where maximum response at this mode was expected. Responses obtained at the third mode were taken at slab midspan.

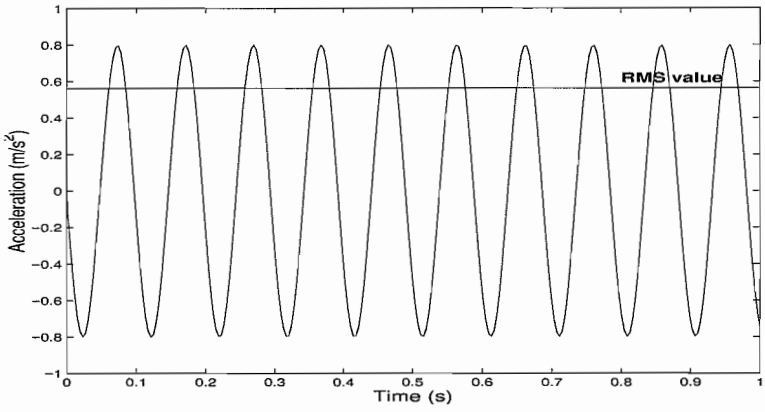

Figure 5.5: Response to sine-wave loading at fundamental frequency

Table 5.8: Summary of RMS steady-state accelerations at slab fundamental frequency

Slab configuration	RMS accel. $\left(\frac{m/s^2}{N}\right)$	Slab configuration	RMS accel. $\left(\frac{m/s^2}{N}\right)$
100kN post-tension force	0.013	5 cant. & one full-height partitions	0.002
175kN post-tension force	0.063	first screed layer (screed 1)	0.033
detensioned for demolishing	0.017	second screed layer (screed 2)	0.030
100kN force with dead load	0.040	screed 1 + man	0.008
175kN force with dead load	0.058	screed 1 + 5 cant. partitions	0.022
false floor layout 1	0.041	screed 1 + man + 5 cant. parts.	0.009
false floor layout 2	0.017	screed 2 + man	0.011
one man near slab centre	0.006	screed 2 + equiv. mass of man	0.026
equiv. mass of man	0.030	screed 2 + 5 cant. partitions	0.027
five perpendicular cant. parts.	0.034	screed 2 + man + 5 cant. parts.	0.012
5 perp. & 3 transverse parts.	0.048	screed 2 + floor layout 1	0.023
one full-height partition	0.002		

5.7.2 Walking excitation

As explained in section 4.5.4, excitation due to normal human activity was performed by a person walking at a medium pace along the slab (horizontal walking), and also as a result of a person walking on the spot near slab centre (vertical walking). Here, the results of these two walking excitations are presented.

Horizontal walking

Table 5.9 shows the RMS acceleration responses, averaged over nine points at the slab centre, as a result of normal human walking. Fast fourier transform (FFT) analysis was also carried out at each point to obtain the dominant frequency. Figure 5.6 shows a typical acceleration response to a walking excitation, and its derived frequency spectrum. Typical responses due to walking on

different slab configurations are shown in figure 5.7 and discussed in chapter 6.

Table 5.9: RMS accelerations due to horizontal walking along slab

Slab configuration	RMS accel. (m/s^2)	Dominant freq. (Hz)	Slab configuration	RMS accel. (m/s^2)	Dominant freq. (Hz)
bare slab (fully stressed)	0.13	7.75	second screed layer (screed 2)	0.04	9.85
false floor layout 2	0.09	7.50	screed 2 + floor layout 1	0.04	9.75
first screed layer (screed 1)	0.06	8.75			

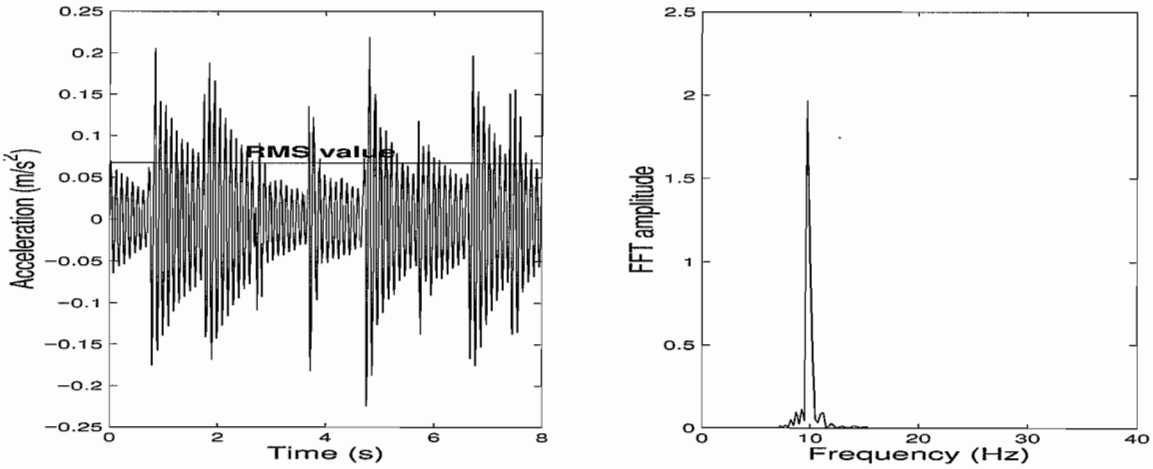

Figure 5.6: Response and frequency spectrum of normal walking along slab with both screed layers

Vertical (on the spot) walking

The RMS acceleration responses of these tests are presented in table 5.10, where average values are given of tests on nine points at the slab centre. Similarly, the FFT frequency spectrum of each point was also taken and averaged for the dominant frequency. Typical responses at different slab configurations are shown in figure 5.8. Notice that in general, the accelerations due to this type of loading are more severe compared to normal walking. This is to be expected, as in this case the loading is purely vertical without any horizontal component. This leads to an increase in loading amplitude, as the whole weight of the person is applied vertically onto the floor.

Table 5.10: RMS accelerations due to vertical walking at slab centre

Slab configuration	RMS accel. (m/s^2)	Dominant freq. (Hz)	Slab configuration	RMS accel. (m/s^2)	Dominant freq. (Hz)
bare slab (fully stressed)	0.14	7.75	second screed layer (screed 2)	0.05	10.13
false floor layout1	0.14	7.50	screed 1 + 5 cant. parts.	0.08	8.50
false floor layout2	0.11	7.38	screed 2 + floor layout 1	0.05	9.80
first screed layer (screed 1)	0.08	8.65	screed 2 + floor layout 2	0.04	9.75

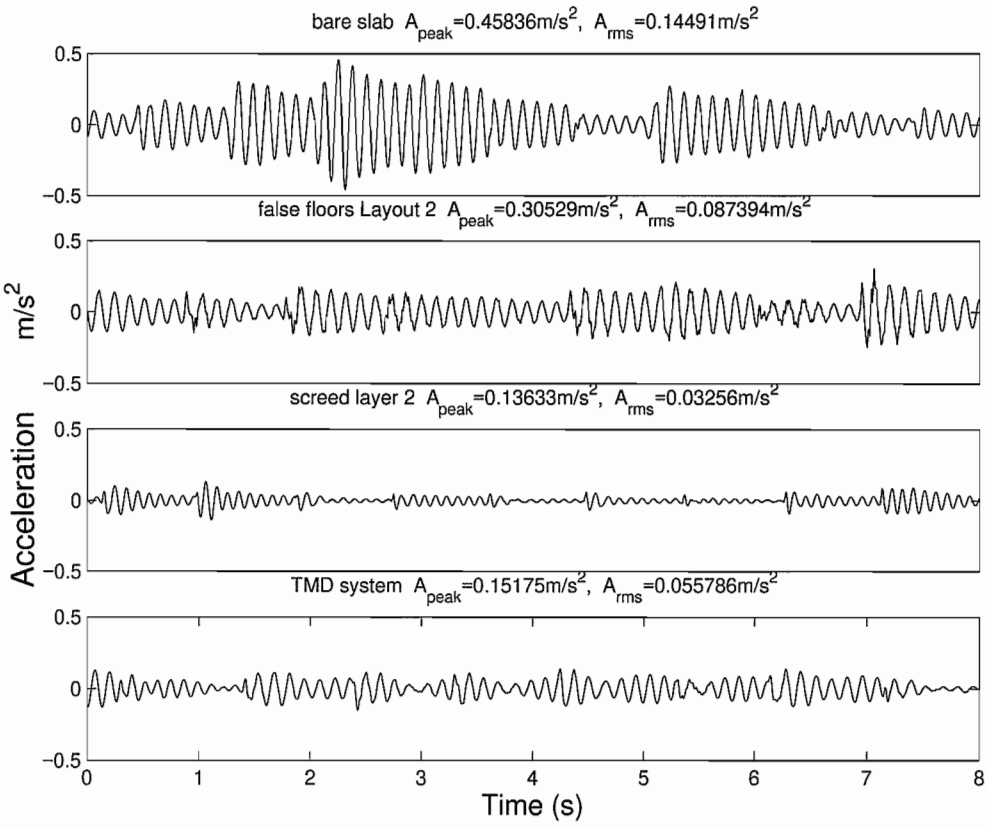

Figure 5.7: Typical response of different slab configurations due to normal walking

5.7.3 Sensitivity analysis

A sensitivity check was carried out for each of the two types of loading excitation to find the range of repeatability of the readings. Here, the accelerometer was placed at a fixed point on the slab and each excitation was repeated five times. The readings obtained should ideally be identical for each case and any differences would give an idea of the range of variability expected within the excitation and measuring system. Table 5.11 shows this range for the three loading cases. As expected, the shaker loading has a small range when compared to walking. Also, vertical walking has a smaller range than horizontal walking as it could be reproduced more accurately during testing.

Table 5.11: Sensitivity ranges of loading types

Excitation type	**maximum range**
steady-state shaker single sine-wave loading	±5%
horizontal walking	±31%
vertical walking	±20%

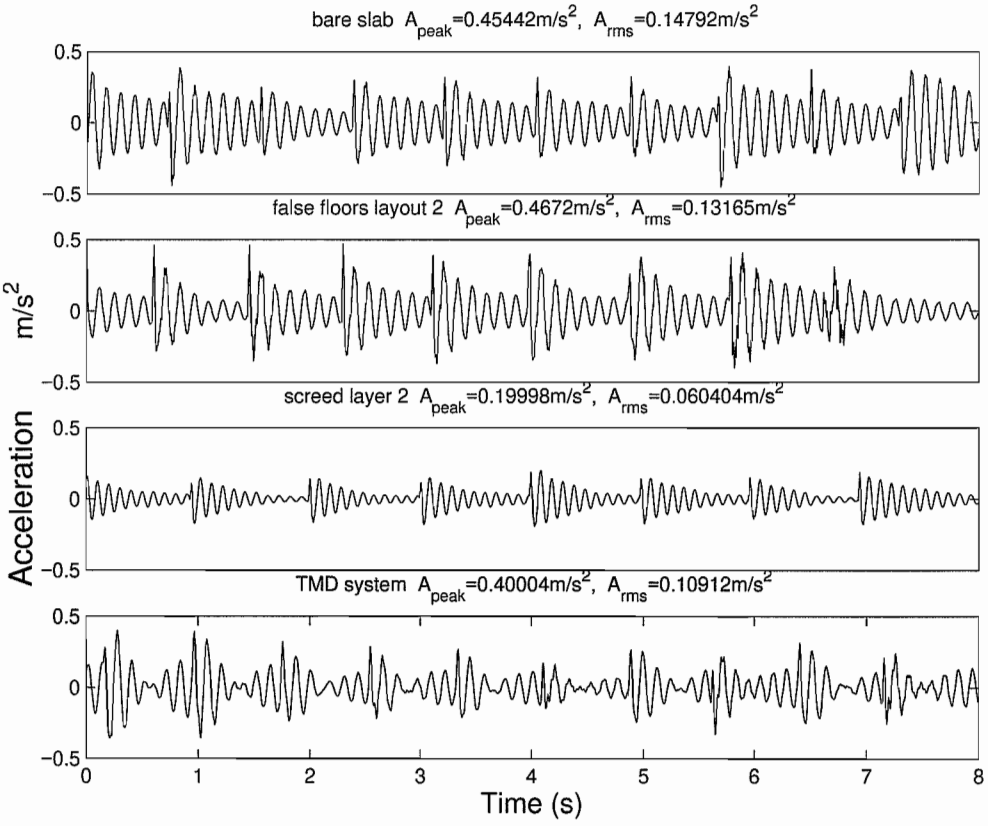

Figure 5.8: Typical response of different slab configurations due to walking on the spot (vertical walking)

5.8 Quality assurance tests

The experimental preparation and setup phases were described in chapter 4, which adhered to quality assurance guidelines layed out in DTA and ISO recommendations [DTA (1993), ISO7626/5 (1994)], and modified for civil engineering testing by Pavic et al. (1997). Here, checks are carried out on the final output results, which also follow the recommendations noted above.

Immediate repeatability check: For each test, two initial FRFs were acquired, using the selected number of averages, one immediately followed by another. For field tests on civil engineering structures, some differences will be expected between these measurements, mainly due to external noise and the low levels of excitation. In laboratory conditions, however, the external influences are minimal and one would expect the readings to be very close. For the model slab, given the relatively high excitation level and minimal noise ratio, the two FRFs were seen to be identical for all slab configurations.

Homogeneity check: In order to check whether the structure behaves linearly, excitation can be applied at two different force levels and FRFs calculated. For a linear system, two such FRFs

should be identical. For the model slab, excitation was applied at full and half amplitude forcing levels and the ensuing FRFs are shown in figure 5.9. Even though very small non-linearities can be observed, particularly at the fundamental mode, the main characteristics of the FRFs agree very closely with each other. For hammer impact excitation, hard and soft hammer blows were used and again the resulting FRFs were in good agreement.

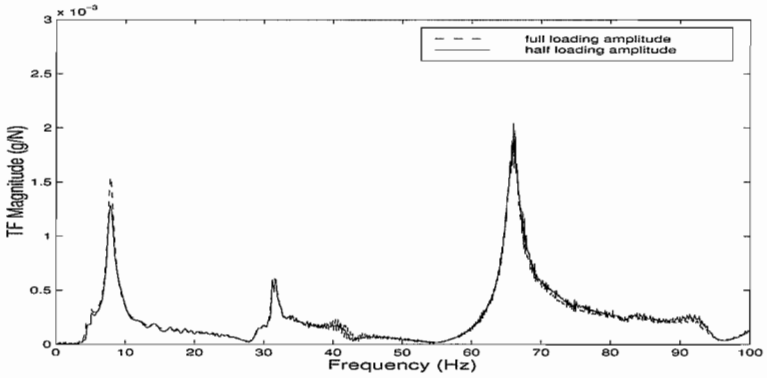

Figure 5.9: Homogeneity check on initial results

Reciprocity check: This is also another linearity check where the excitation was applied at one point on the slab and response measured at another. The excitation and response points were swapped and the measurement repeated. Maxwell's theorem states that the pairs of FRFs should be identical [Pavic et al. (1997)] and this was observed for the experimental slab.

Coherence function check: As described in section 4.6, coherence checks were carried out for each test. Due to laboratory conditions and high relative excitation levels, coherence readings at peak FRFs were in most cases as high as 98% or above.

End of test repeatability check: At the end of each testing phase, an FRF was measured using the exact setup as for the immediate repeatability check. This FRF was then compared to one taken at the start of testing and very close agreement was observed in each case. Any significant differences would have indicated problems with noise, changing environmental conditions, or with characteristics of the structure changing slowly through the test (e.g. due to temperature variations or time-dependent changes in material properties).

The above checks were performed on the experimental results of this chapter. As expected, the results were seen to be of high quality due to laboratory conditions. The above checks would become very useful in field testing conditions, particularly in environments with high external noise and weather fluctuations. Further checks were also performed, such as shaker efficiency, accelerometer sensitivity, and load-cell accuracy; these are described in section 3.7.

Chapter 6

Analyses of results

6.1 Introduction

In this chapter, the results from the model slab tests are analysed with regards to the slab dynamic properties. Analytical models are derived to estimate the dynamic parameters after each alteration in the experiment. The test results are then compared with the estimated values and any implications are discussed. Particular attention is given to the effects on the slab dynamic characteristics after changes in prestressing, addition of false floors, addition of partitions, and the inclusion of high damping screed layers. Analyses of tests with TMDs and the effects of structure-human interaction are dealt with in chapters 7 and 8 respectively.

6.2 Effect of prestress

In this section, the effect of prestressing on the dynamic behaviour of the model slab is reported. The tensioning of the tendons was carried out in two stages of 100kN and 75kN (i.e. 57% and 100% of the design force). The resulting natural frequencies of the bare beam are presented and compared with estimated values, using two different approaches. A theoretical analysis is given to represent the changes. The derived damping ratios and their significance are also discussed.

6.2.1 Natural frequency

There is at present some dispute about the effect of prestressing force on natural frequencies of slabs and bridges. While some researchers regard prestressing as a direct influence on the natural frequency of the system [Saiidi et al. (1994)], others see the influence as an indirect effect related to level of cracking [Deák (1996), Jain and Goel (1996)]. Both these approaches are examined below

with respect to the model slab results. It is shown that incorporating the prestressing force as a direct factor in beam dynamics, leads to a poor agreement with experimental results. The results are best represented by consideration of cracking, using the effective cross-section. A theoretical discussion is presented to support these claims.

Slab with axially applied force

Here, the direct effect of prestressing force on natural frequency is investigated from the viewpoint of beam dynamics. It will be shown that in theoretical analyses, prestressing force has a minimal or negative influence on the natural frequency of beams.

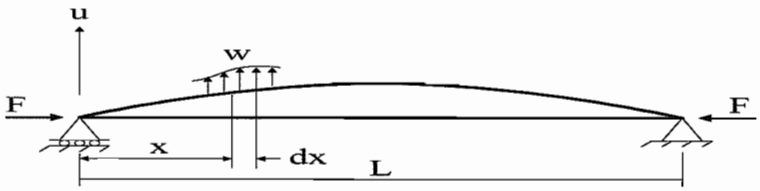

Figure 6.1: Effect of axial compression on beam vibration

Consider a vibrating homogeneous beam subjected to a compressive force, F, as shown in figure 6.1. The differential equation of deflection, under static loading, is derived by taking moments about a point at x:

$$EI\frac{d^2u}{dx^2} = M - Fu \tag{6.1}$$

where M denotes the bending moment produced by the loading of intensity w (i.e. $M = \frac{wx^2}{2}$). By double differentiation of equation 6.1, with respect to x, the following is obtained:

$$\frac{d^2}{dx^2}\left(EI\frac{d^2u}{dx^2}\right) = w - F\frac{d^2u}{dx^2} \tag{6.2}$$

Assuming the beam is uniform and in free vibration, the inertial force per unit length is substituted for w to give:

$$EI\frac{\partial^4u}{\partial x^4} + F\frac{\partial^2u}{\partial x^2} = -\rho A\frac{\partial^2u}{\partial t^2} \tag{6.3}$$

which is the equation of free transverse vibration. Assume a harmonic solution of the form:

$$u = \Phi(x)\cos(\omega t - \phi) \tag{6.4}$$

where $\Phi(x)$ is the assumed mode shape function. Substituting equation 6.4 into equation 6.3 gives:

$$EI\frac{d^4\Phi(x)}{dx^4} + F\frac{d^2\Phi(x)}{dx^2} = \omega^2\rho A\Phi(x) \tag{6.5}$$

For a simply supported beam, the mode shape, $\Phi(x)$, will be satisfied by:

$$\Phi_n(x) = \sin\frac{n\pi x}{L} \qquad (n=1,2,3,\ldots) \tag{6.6}$$

Substituting this expression into equation 6.5 gives the angular frequency of vibration:

$$\omega_n = \frac{n^2\pi^2}{L^2}\sqrt{\frac{EI}{\rho A}}\sqrt{1-\frac{FL^2}{n^2EI\pi^2}} \tag{6.7}$$

It can be deduced that the derived frequency expression yields smaller values than that for a simply supported beam without axial compression (i.e. when F=0), so that an increase in compressive force decreases natural frequencies. This is contrary to the experimentally derived values of natural frequency with increasing prestress (table 5.1, page 94). Thus, an opposite trend to theory is observed. Similar results were also found by Saiidi et al. (1994) in both field and laboratory conditions. They attributed the differences to a change in the rigidity, EI. Other reported tests have also found prestressed beams to possess higher natural frequencies than equivalent reinforced ones [James et al. (1964), Caverson (1992), Zaman and Boswell (1996)].

Dall'Asta and Dezi (1996) and Deák (1996) argued that equation 6.7 is not a true representation for a post-tensioned beam as the axial force is applied externally in the theory (figure 6.1). Such a force maintains its original line of action during the vibration of a member, thus being converted into an eccentric force with respect to the beam axis. This will reduce the natural frequency and may even lead to buckling. Such a situation does not apply to prestressing cables that are themselves anchored to the end faces of the beam, making the axial force an internal force within the system.

Hence, the effect of prestressing cables in concrete may be better represented by energy considerations. The fundamental mode shape of a simply supported uniform beam, with or without the axial force, can be assumed as sinusoidal (equation 6.6). Thus, its fundamental frequency can be obtained by equating the maximum kinetic energy to the maximum potential energy, under free vibration. Considering the beam of figure 6.1, its motion at the first mode can be expressed by combining equations 6.4 and 6.6:

$$u(x,t) = X\sin\left(\frac{\pi x}{L}\right)\cos(\omega t-\phi) \tag{6.8}$$

where X is the amplitude of vibration at midspan. Kinetic energy during the vibration may be expressed as:

$$KE = \int_0^L \frac{1}{2}\rho A\left(\frac{\partial u}{\partial t}\right)^2 dx = \frac{1}{4}\rho A\omega^2X^2L\sin^2(\omega t-\phi) \tag{6.9}$$

In the case of an externally applied force, potential energy in the beam will be due to flexural deformation minus the work done by the external force due to the movement of the two ends of

the beam [Jain and Goel (1996)]. It is given by:

$$PE = \int_0^L \frac{1}{2} EI \left(\frac{\partial^2 u}{\partial x^2}\right)^2 dx - F \int_0^L \frac{1}{2} \left(\frac{\partial u}{\partial x}\right)^2 dx = \left(\frac{\pi^4 EIX^2}{4L^3} - \frac{\pi^2 FX^2}{4L}\right) \cos^2(\omega t - \phi) \quad (6.10)$$

Equating maximum kinetic energy with maximum potential energy, for the case of the externally applied axial force, gives:

$$\omega^2 = \frac{\pi^4 EI}{\rho AL^4} - \frac{\pi^2 F}{\rho AL^2} \quad (6.11)$$

Note that equation 6.11 is the square of equation 6.7. Now consider the case of free vibration of a simply supported beam with internal prestress force. Motion at the first mode will still be given by equation 6.8, which again leads to the kinetic energy expression of equation 6.9. However, since there is no longer an externally applied axial force, the second term in equation 6.10 does not exist. For this case, equating maximum kinetic and potential energies, gives the fundamental frequency of a prestressed beam as:

$$\omega^2 = \frac{\pi^4 EI}{\rho AL^4} \quad (6.12)$$

which is the same as equation 2.8 for a simply supported beam without prestress. Hence, representing the prestressing force as an internal force, as opposed to external axial force, shows no effect on the natural frequency. This is again contrary to the experimental results, which show an increase in natural frequency with increased prestress (table 5.1, page 94).

The above analyses show that equations 6.7 and 6.12 do not provide a basis for theoretical prediction of the variation in natural frequency with changes in prestress. This has led to many researchers suggesting phenomena of different origins, such as cracking, where an increase in prestressing force closes the microcracks in the concrete, hence increasing the natural frequency as a result of higher stiffness. This effect has not been modelled adequately to date [Saiidi et al. (1994)]. An attempt at such a model is described in the following section.

Effect of prestress force on cracking

Table 6.1 shows the average natural frequencies of the slab in the fundamental mode with varying levels of prestress and dead load. With changes in the prestressing force, there was no discernible effect on the mode shapes. As explained in section 2.4.3, the level of cracking is an important factor in determining the stiffness and natural frequency of the floor. To investigate this effect, a theoretical method for predicting natural frequencies, due to level of prestress, was evaluated. The method takes account of the cracked and uncracked sections of the cross-section, at each stage of prestressing. The change in level of cracking will affect section modulus and second moment of area, thus altering the calculated value of natural frequency.

The effective second moment of area, I_e, of a cracked section, averaged over length, depends on the loss of effective depth due to cracking and is given by: [ACI (1995), Kong and Evans (1989)].

$$I_e = \left(\frac{M_{cr}}{M_a}\right)^3 I_u + \left[1 - \left(\frac{M_{cr}}{M_a}\right)^3\right] I_{cr} \tag{6.13}$$

where M_a is the maximum gross moment, I_u is the uncracked second moment of area, M_{cr} is the moment needed to start cracking, and I_{cr} is the cracked second moment of area at the most heavily loaded section. Here, I_{cr} is obtained by replacing the actual area of reinforcement with an equivalent concrete area located at the level of the steel, as shown in figure 6.2. By using this transformed section, I_{cr} is calculated from the position of the cracked neutral axis (see appen. C). Equation 6.13 is valid if M_{cr} is smaller than M_a, so that the moment needed to initiate cracking is not larger than the maximum possible moment on the slab. This also means that in a cracked section, I_e is always smaller than I_u, and no tensile strength is present in the cracked region.

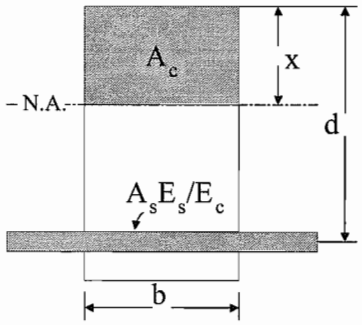

Figure 6.2: Cracked transformed section

The bending moment at the onset of cracking, M_{cr}, can be found by equating the concrete tensile stress, f_t, (dependent on the type of concrete section) with the tensile strength, σ_t, (found experimentally). For a reinforced beam, the maximum tensile stress at the onset of cracking occurs at the furthest distance from the neutral axis. Equating tensile stress and strength at this point gives:

$$f_t = \sigma_t = \frac{M_{cr} y_t}{I_u} \tag{6.14}$$

where y_t is the depth to the neutral axis. With prestressing force, the added compression in the tension zone reduces f_t, so that a higher moment is required to initiate cracking (see figure 6.3). Equating tensile stress and strength at the furthest point from the neutral axis gives:

$$f_t = \frac{M_{cr} y_t}{I_u} - \frac{P_t}{bh} - \frac{P_t e y_t}{I_u} \tag{6.15}$$

where P_t is the total prestressing force in tendons and e is the tendon eccentricity. Equation 6.15 also shows that if the section is already cracked, increasing the prestressing force has the effect of

reducing the level of cracking, due to the increased compression and an increase in M_{cr}. This will lead to stiffening of the system and an increase in its natural frequency. Typical calculations of M_{cr} and I_e in the uncracked, cracked, and partially cracked states are shown in appendix C.

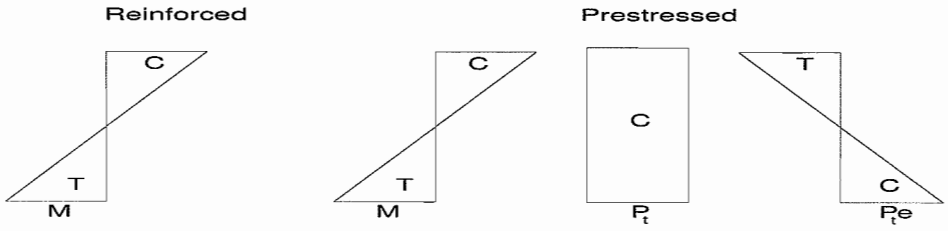

Figure 6.3: Stresses present in uncracked reinforced and prestressed sections

Once the effective second moment of area for each prestressing stage is obtained, it can be used to calculate fundamental frequency using the EBM, static deflection, or Concrete Society methods (see section 2.5.3). Typical calculations of the model slab fundamental frequency are shown in appendix D. Table 6.1 shows the experimental values as compared with predicted values, with and without consideration of cracking.

Table 6.1: Comparison of experimental and estimated fundamental frequencies

Slab State	σ_{av} **(MPa)**	f_0**(exp) (Hz)**	**Estimates of f_0 (Hz)**					
			EBM		**Static def.**		**Conc. soc.**	
			original	revised	org.	rev.	org.	rev.
Baseline case - bare slab full prestress	**5.2**	**8.0**	8.0	8.0	8.0	8.0	8.0	8.0
bare slab 57% prestress	3.0	7.6	8.0	8.0	8.0	8.0	8.0	8.0
bare slab no prestress	0	7.5	8.0	7.5	8.0	7.5	8.0	7.5
Extra live load of 0.25kN/m^2 full prestress	5.2	7.7	7.7	7.7	7.7	7.7	7.7	7.7

In their original form, the estimation methods assume the slab to be uncracked and give inaccurate predictions for cracked sections. By revising the methods to take cracking into account, acceptable agreement is observed between estimated and actual results. This indicates that the changes in natural frequency with level of prestress are due largely to changes in the amount of cracking. However, with the partially cracked case, the calculations in appendix C show that the entire section is effective and no cracking exists. This was not reflected in the experimental results. The reason could be the long duration of time between the prestressing stages, and possible prestress losses, leading to changes in the section properties of the slab. The theoretical estimates when fully prestressed and with no prestress, give a very good match with the experimental results when cracking is considered. Hence, it can be stipulated that by using the above mentioned method, the

fundamental frequency of a floor slab may be predicted approximately at a given prestressing level. However, more evidence is needed to qualify the theory.

6.2.2 Damping

The damping of the slab is greatly affected by the prestressing force, due to closing up of micro-cracks. Table 6.2 shows the average damping values obtained for each prestressing stage (from tables 5.1-5.2). With an increase in prestress and fewer cracks within the slab, there is less energy dissipation and hence lower damping. This is discussed more in section 2.6.3.

Table 6.2: Comparison of experimental damping values with effective second moment of area after cracking

Slab State	σ_{av} **(MPa)**	ζ **(exp) (% critical)**	**percent change**	I_e $(\times 10^{-4}$ m$^4)$	**percent change**
(i) Baseline case - bare slab full prestress	**5.2**	**1.1**	-	2.2	-
(ii) bare slab 57% prestress	3.0	1.7	+55% of (i)	2.2	no change
(iii) bare slab no prestress	0	1.9	+73% of (i) +12% of (ii)	1.9	-14% of (i)
(iv) Extra live load of 0.25kN/m^2 full prestress	5.2	1.2	+9% of (i)	2.2	no change

Table 6.2 also shows the percentage change in damping as a result of prestress, compared with the change in effective second moment of area calculated previously. An increase in the level of prestress has a severe detrimental effect on the damping of the slab, as compared with a small change in its effective section. This can be attributed to the actual number of cracks involved, rather than their individual depths. Again, the calculations show no change in I_e between the partially prestressed and fully prestressed stages. This is not reflected in the experimental results and is attributed mainly to prestress losses and the time spent between the prestressing stages, which could have the effect of increasing the number of cracks.

With the application of live load, the section modulus is unchanged but an increase in damping is observed, again due to increased bending and appearance of more microcracks in the tension zone.

6.3 Effect of false flooring

As explained in section 3.6.4, two false floor layouts were tested, differing in number of panels and their nature of installation. Full results are given in chapter 5 and appendix A. Table 6.3 shows the average slab fundamental frequencies and damping ratios with the two false floor configurations.

Table 6.3: Effect of false flooring on slab vibration properties (fundamental mode)

Slab configuration	Fundamental frequency (Hz)		Damping (% critical)	
	experimental	theoretical	experimental	% change
bare slab (fully tensioned)	8.0	8.0	1.10	-
Layout 1 total of 7 panels (all rigidly fixed)	7.9	7.8	1.17	+6
Layout 2 total of 14 panels (fixed at centres, loose at corners)	7.6	7.6	1.83	+66

It can be seen that in both cases the weight of the panels leads to reductions in natural frequency, depending on the number of panels used. This reduction may be derived theoretically, where the mass of the panels can be added to the overall mass of the slab. From table 6.3, the predictions agree well with experimentally derived values, indicating that the changes in natural frequency are consistent with the panels simply acting as uniform added mass.

Consideration of changes in damping, shows a small increase with layout 1 as compared with a 66% increase with layout 2 configuration. It thus appears that when rigidly attached, the floor panels add mass to the structure and do not introduce any significant additional stiffness or damping. However, when some edges simply rest on the pedestals, as in layout 2, there is a noticeable increase in damping. This is most likely caused by sliding and/or gapping between the panels and pedestals. It raises the possibility that false floors could be designed to allow this relative motion as a deliberate energy dissipation device. Note that with some false flooring systems, which use heavy panels typically made from timber, all the floor panels rest on the pedestals and rely on their self-weight for stability. In such cases, the overall damping of the slab could be further increased, as compared to layout 2 of the model tests.

6.4 Effect of non-structural partitions

As described in section 3.6, two types of partitions were tested, in the form of cantilever and full-height representations, to simulate those commonly used in offices. Full test results are included in chapter 5 and appendix A. Table 6.4 summarises the effects of the partitions on the model slab vibration parameters. The results suggest a wide difference between the effects of cantilever, as opposed to full-height, partitions. These are described separately in the following sections.

Table 6.4: Effect of partitions on slab vibration properties in the fundamental mode (see figure 3.12, page 60, for partition positions)

Slab configuration	**Fundamental frequency (Hz)**		**Damping (% critical)**	
	experimental	**% change**	**experimental**	**% change**
bare slab (fully tensioned)	8.0	-	1.10	-
Layout 1 five cantilever partitions (perpendicular to slab span)	7.7	-3.8	1.31	+19
Layout 2 three cantilever partitions (parallel to slab span)	8.0	0	1.10	0
Layout 3 five perpendicular and three parallel to slab span	7.8	-2.5	1.69	+54
Layout 4 one full-height partition (perpendicular to slab span)	20.3	+154	1.95	+77
Layout 5 five cantilever and one full-height (all perpendicular to slab span)	20.3	+154	1.96	+78

6.4.1 Effect of full-height partitions

Table 6.4 shows a significant change in the slab vibration parameters, after the addition of full-height partitions at the underside of the model slab. Considering the case of one partition at midspan, when rigidly attached at top and bottom, it effectively acts as a line support giving the slab fundamental mode shape of figure 6.4. When compared with the mode shape of the bare slab (figure 5.4, page 96), the added stiffness at the midspan can be seen. This is confirmed by the measurements of fundamental frequency, where an increase of over 150% was observed.

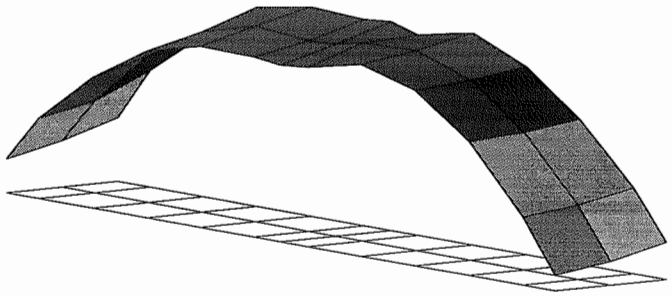

Figure 6.4: Fundamental mode shape of slab with a full-height partition at midspan

To assess the behaviour of the partition itself, its horizontal response was measured. Figure 6.5 shows a typical transfer function of the partition at its centre, compared with that of the slab. Note that the fundamental frequencies are identical and the transfer functions are broadly similar in shape, which indicates that the slab and partition act compositely at all frequencies. In addition, figure 6.6 shows the first two measured mode shapes of the full-height partition, indicating a bowing action. Hence, the experiments show that the changes to the slab dynamic behaviour are due to

the partition acting as a flexible, vertical support whose primary mode of deformation is lateral bowing under the vertical load, as shown in figure 6.7.

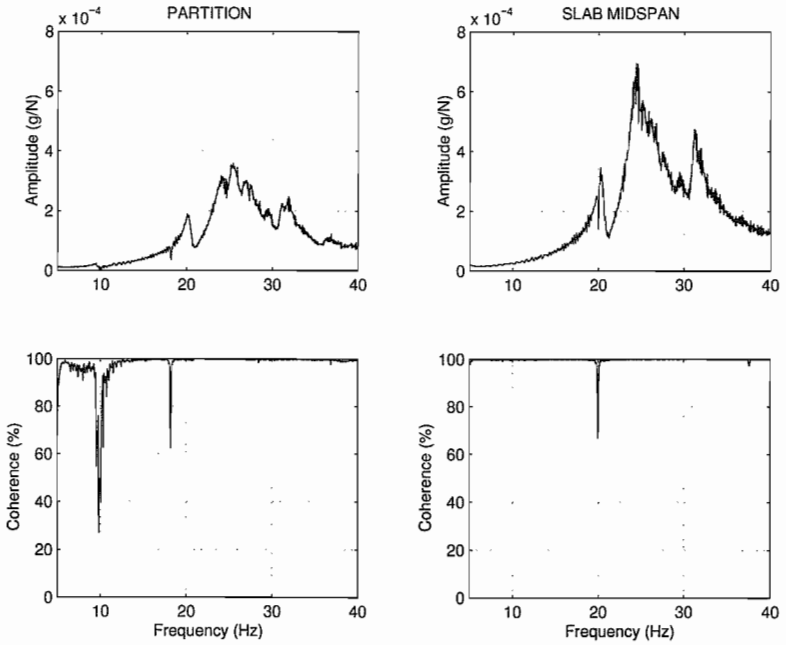

Figure 6.5: Comparison between FRF of full-height partition in horizontal direction with that of slab in vertical direction

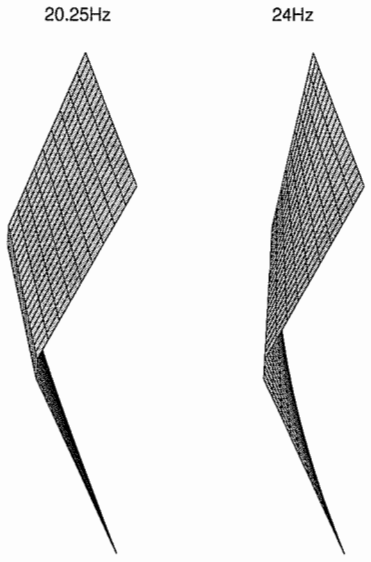

Figure 6.6: First two mode shapes of full-height partition

These results illustrate that some non-structural additions on a floor can in fact behave in a structural way and add extra stiffness to the main system, as well as increase the inherent damping. If well designed, this is an inexpensive way of alleviating annoying vibrations on a problematic floor.

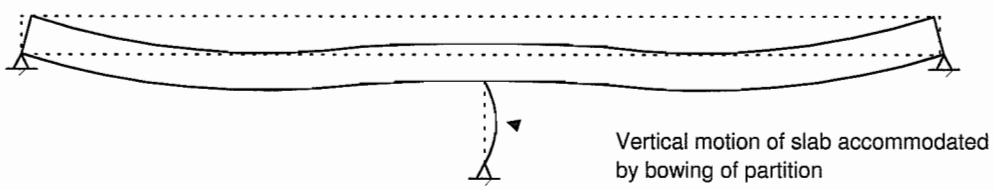

Figure 6.7: Slab with full-height partition

Analytical model approximation

To create an analytical model for the effect of a full-height partition, consider the added slab stiffness by representing the partition as a spring with stiffness, k_p, placed at a distance, (a), from the support. This leads to the slab behaving as a *constrained structure* as shown in figure 6.8.

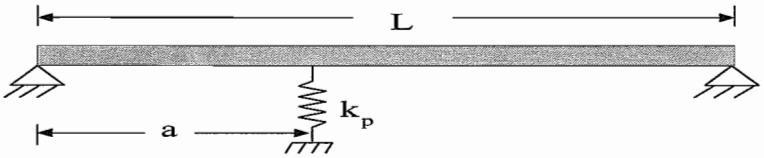

Figure 6.8: Analytical model approximation of a full-height partition

A common approach for defining the response of a constrained structure is to formulate the problem in terms of *generalised co-ordinates* and use the mode summation technique. First, the normal modes and mode shapes of the unconstrained structure (without partition/spring) are used to derive the generalised parameters, and then the effect of the spring is taken into account.

Unconstrained beam

Consider a simply supported beam with applied loading of $p(x,t)$, as shown in figure 6.9. The overall deflected shape of the structure, $u(x,t)$, can be approximated as the sum of n mode shapes, $\Phi_i(x)$, multiplied by a time coefficient, $q_i(t)$:

$$u(x,t) = \sum_{i=1}^{n} \Phi_i(x) q_i(t) \tag{6.16}$$

where $q_i(t)$ is called the *generalised co-ordinate*, which is effectively the vibration amplitude at a point on the structure (e.g. the midspan of a simply supported beam).

The generalised co-ordinate can be used to analyse the problem by considering the beam as a SDOF system (figure 6.9) with the governing equation:

$$M_i^* \ddot{q}_i + K_i^* q_i = F_i^* \tag{6.17}$$

In order for the SDOF system to be equivalent to the continuous structure, appropriate values must be chosen for the generalised mass, M_i^*, stiffness, K_i^*, and force, F_i^*. This can be achieved using

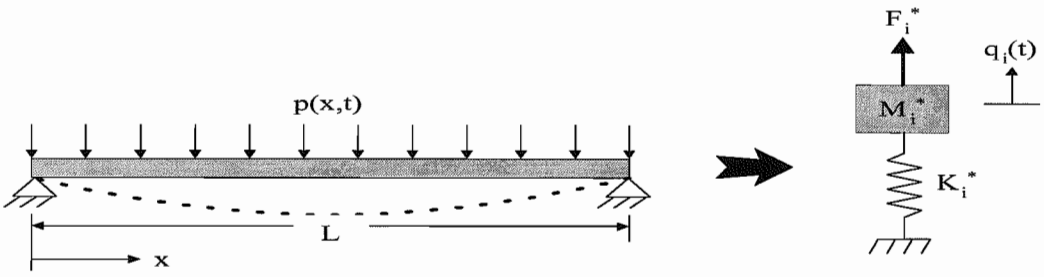

Figure 6.9: Unconstrained beam

energy considerations. For derivation of M_i^*, the kinetic energy of the mass of the beam is found over its entire length: (see equation 2.11, page 24)

$$KE = \int_0^L \frac{1}{2} w \dot{u}^2 dx = \sum_{i=1}^{n} \frac{1}{2} \dot{q}_i^2 M_i^* \qquad \text{where} \qquad M_i^* = w \int_0^L \Phi_i^2 dx \tag{6.18}$$

Similarly, K_i^* is found by considering the strain or potential energy in the structure over its length: (see equation 2.12, page 24)

$$PE = \int_0^L \frac{1}{2} EI u''^2 dx = \sum_{i=1}^{n} \frac{1}{2} q_i^2 K_i^* \qquad \text{where} \qquad K_i^* = EI \int_i^L \Phi_i''^2 dx \tag{6.19}$$

Note that $\dot{u}$ denotes differentiation with respect to t and u' denotes differentiation w.r.t x. Finally, for the unconstrained beam with uniformly applied load, $p(x,t)$, F_i^* is derived from the work done by the force:

$$WD = \int_0^L pu dx = \sum_{i=1}^{n} q_i F_i^* \qquad \text{where} \qquad F_i^* = p \int_0^L \Phi_i dx \tag{6.20}$$

For equations 6.18-6.20, the exact modes, ω_i, and mode shapes, Φ_i, can be calculated by considering the beam as a continuous system. These can be written as: (see equation 2.8, page 23)

$$\omega_i = i^2 \pi^2 \sqrt{\frac{EI}{wL^4}} \qquad \text{and} \qquad \Phi_i(x) = \sin\left(\frac{i\pi x}{L}\right) \tag{6.21}$$

Constrained beam

At this stage, the effect of the full-height partition can be introduced by considering the force, due to the spring in figure 6.8, as a concentrated point load applied at (a) (see figure 6.10). In such a case, the generalised mass and stiffness of the beam are unaffected but the generalised force, F_i^*, must be updated from a distributed load to a concentrated point load, $F_{p_i}^*$.

Consideration of the work done at (a), due to the point load, gives:

$$\begin{aligned} \Delta WD &= p(a,t)\, \Delta u(a,t) = p(a,t) \textstyle\sum_{i=1}^{n} \Phi_i(a)\, \Delta q_i(t) \\ \Rightarrow \quad F_{p_i}^* &= \frac{\Delta WD}{\Delta q_i} = p(a,t)\, \Phi_i(a) \end{aligned} \tag{6.22}$$

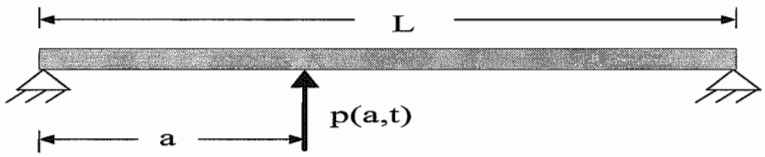

Figure 6.10: Constrained beam

In terms of spring stiffness, k_p, equation 6.22 can be expressed as:

$$\begin{aligned} p(a,t) &= -k_p u(a,t) = -k_p \textstyle\sum_{i=1}^{n} \Phi_i(a)\, q_i(t) \\ \Rightarrow \quad F_{p_i}^{*} &= -k_p \Phi_i(a) \textstyle\sum_{i=1}^{n} \Phi_i(a)\, q_i(t) \end{aligned} \tag{6.23}$$

Note here that for the case of the constrained beam, the same modes are used as for the unconstrained structure. This is justified since the spring is treated as an external load and it therefore has no influence on the beam free vibration characteristics. Hence, the response of the beam with the spring is thought of as a linear combination of the modes of the beam without the spring. Substituting equations 6.18, 6.19 and 6.23 into equation 6.17 and rearranging gives:

$$\ddot{q}_i(t) + \omega_i^2 q_i(t) = \frac{1}{M_i^*}\left[-k_p \Phi_i(a) \sum_{i=1}^{n} \Phi_i(a)\, q_i(t)\right] \tag{6.24}$$

where the terms outside the summation refer to the behaviour of the ith mode of the unconstrained beam, and for the constrained beam, the ith mode is the summation of all the modes of the unconstrained beam. By assuming that the SDOF system vibrates at some frequency, Ω, related to the spring stiffness, and that the response is harmonic, the solution can be written in the form:

$$q_i = \bar{q}_i e^{i\Omega t} \tag{6.25}$$

Substituting into equation 6.24 and rearranging gives:

$$\bar{q}_i = \frac{1}{M_i^*\left(\omega_i^2 - \Omega^2\right)}\left[-k_p \Phi_i(a) \sum_{i=1}^{n} \Phi_i(a)\, \bar{q}_i\right] \tag{6.26}$$

In equation 6.26, with n modes, there will be n values of $\bar{q}_i$ and n equations. The determinant formed by the coefficients of $\bar{q}_i$ will lead to the natural frequencies of the constrained modes. The mode shapes of the constrained structure are then found by substituting the $\bar{q}_i$ into equation 6.16. Equation 6.26 is simplified by substituting for Φ_i from equation 6.21:

$$\bar{q}_i = \frac{1}{M_i^*\left(\omega_i^2 - \Omega^2\right)}\left[-k_p \sin\left(\frac{i\pi a}{L}\right) \sum_{i=1}^{n} \sin\left(\frac{i\pi a}{L}\right) \bar{q}_i\right] \tag{6.27}$$

For the purposes of this discussion, the fundamental mode is the only mode of interest, and hence for a single mode approximation, equation 6.27 reduces to:

$$M_1^*\left(\omega_1^2 - \Omega^2\right) = -k_p \sin^2\left(\frac{\pi a}{L}\right) \tag{6.28}$$

from which the first natural frequency of the constrained beam can be found, where:

$$\Omega^2 = \omega_1^2 + \frac{k_p}{M_1^*} \sin^2\left(\frac{\pi a}{L}\right) \tag{6.29}$$

In the experimental programme, the partition was placed at the slab midspan, so taking $a=\frac{L}{2}$, M_1^*=806kg (see appendix B), ω_1=(2π×8.0)rads/s (table 6.4), and k_p=7.52×10^{6}N/m (see appendix E), equation 6.29 gives a value for the constrained slab frequency of 17.3Hz. This compares with the experimentally derived value of 20.3Hz. The difference can probably be attributed to the relatively large error range in k_p (see below and appendix B).

The main assumption in the model is that the base of the partition is fixed to the ground without allowance for any ground motion. In real buildings, the partition would be fixed to the floor above, which would itself be prone to vibrations. Hence, there would be some ground motion at both ends of the partition. In the experimental tests, the difference in mass between the supporting ground and the slab was large, hence the ground could be assumed as completely fixed.

Application of the model

The simulated full-height partition, used in these experiments, had a total height of 400mm with an average derived axial stiffness of 7.52×10^{6}N/m. In real floors, the partition height would be expected to range from say 2m to 3.5m. Assuming the change in stiffness is linearly proportional to partition length, (as found experimentally in appendix B to within 15%), this would lead to a reduction in stiffness. Table 6.5 gives typical suggested values for the stiffness of gypsum plasterboard partitions. The figures given are purely based on a few experimental results and should only be taken as a rough guideline. The error ranges given are in accordance with those found experimentally. The material properties of plasterboard are dependent on many factors, including handling history, internal damage, quality of gypsum, and the manufacturing process.

Table 6.5: Suggested values of axial stiffness for gypsum plasterboard partitions

Partition thickness (mm)	**Partition height (mm)**	**Predicted stiffness (N/m) (±15%)**
9	2000	1.5×10^6
	3500	8.6×10^5
12	2000	2.0×10^6
	3500	1.1×10^6
18	2000	3.0×10^6
	3500	1.7×10^6
25	2000	4.2×10^6
	3500	2.4×10^6

Refering to figure 6.8, for any simply supported slab, equation 6.29 can be further simplified to:

$$f_{0_c}^2 = f_0^2 + \frac{k_p}{2\pi^2 \rho b h L} \sin^2\left(\frac{\pi a}{L}\right) \tag{6.30}$$

where f_{0_c} is the constrained fundamental frequency with the partition, and f_0 is the fundamental frequency without the partition. Figure 6.11 gives plots of equation 6.30 for the model slab at quarter and midspan points. Note the effect of partition stiffness on the overall slab frequency.

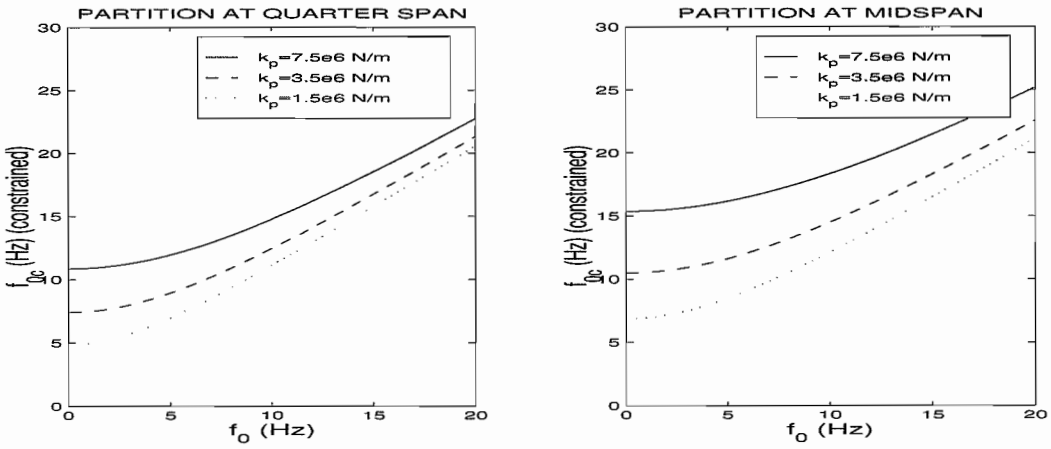

Figure 6.11: Plot of equation 6.30 for the model test slab

Proposed design guideline

Given a particular floor, a simple design guideline can be utilised to assess the effects, on the floor fundamental frequency, of adding full-height partitions. The suggested design steps are:

Step 1: Find the slab fundamental frequency, f_0, by experiment or calculation.

Step 2: Decide on the target fundamental frequency of the slab, f_{0_c}, after the addition of full-height partitions. For man-induced vibrations, table 2.5 (page 44) gives recommended values.

Step 3: Knowing the position along the span at which the partition is to be placed, (a), use equation 6.30 to arrive at a desirable stiffness, k_p, for the partitions.

Step 4: For gypsum partitions, table 6.5 gives suggested thicknesses for a given height. With knowledge of their axial stiffness, the use of other types of partition can also be investigated.

- For two-way slabs, the span to be considered is the one perpendicular to the partition
- If using more than one partition, the added stiffness would be higher than in equation 6.30 and f_{0_c} will be expected to be increased.

- The steps given above can be used in reverse form, where the type and dimensions of the partitions would be known, leading to a value of stiffness from table 6.5. The increase in slab frequency can then be derived from equation 6.30.

6.4.2 Effect of cantilever partitions

Table 6.4 shows that the direction of the cantilever partitions, with respect to the slab span, affects their contribution to slab vibration. When positioned parallel to the slab span, they were seen to have no effect on the vibration behaviour of the floor. When positioned perpendicular to the span, a noticeable increase in damping was observed. This is most likely due to the dissipation of energy through axial deformations and swaying of the partitions. The biggest increase in damping was observed when the partitions were placed in both directions and joined together.

To investigate the behaviour of individual partitions during vibration, response readings were taken at five points on each partition. In these tests, sine-sweep and single sine-wave excitations were imposed on the slab and the accelerometer was placed on the partitions in both vertical and horizontal directions. Figure 6.12 shows a typical transfer function in the horizontal direction as compared with that of the slab in the vertical direction. Note that the partition exhibits a mode at the fundamental frequency of the slab. The other peaks for the partition are not present in the slab. This indicates that at the slab fundamental frequency, the cantilevers act compositely with the floor, whereas in other modes, they act as separate systems sitting on the floor.

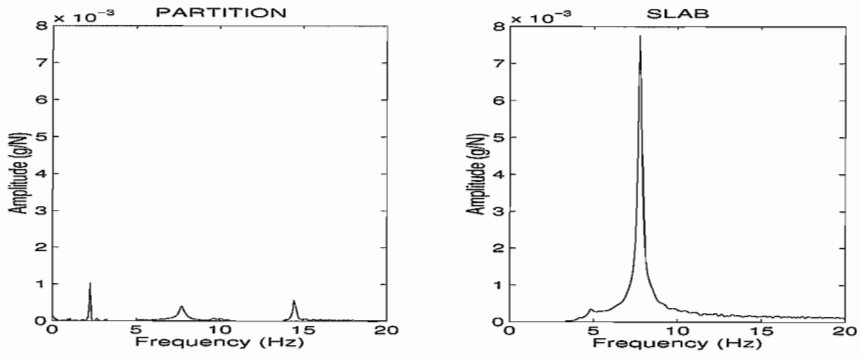

Figure 6.12: Comparison between FRF of cantilever partition in horizontal direction (partition 3, layout 1) with that of slab in vertical direction, following sine-sweep loading applied on the slab

Figure 6.13 shows the horizontal acceleration responses of all partitions measured at the free edge (i.e. top of the partitions). Here, it is observed that swaying takes place at all partitions and is

more apparent for partitions which are away from midspan, where the rotation of the slab is highest (i.e. partitions 1 and 5 in figure 3.12).

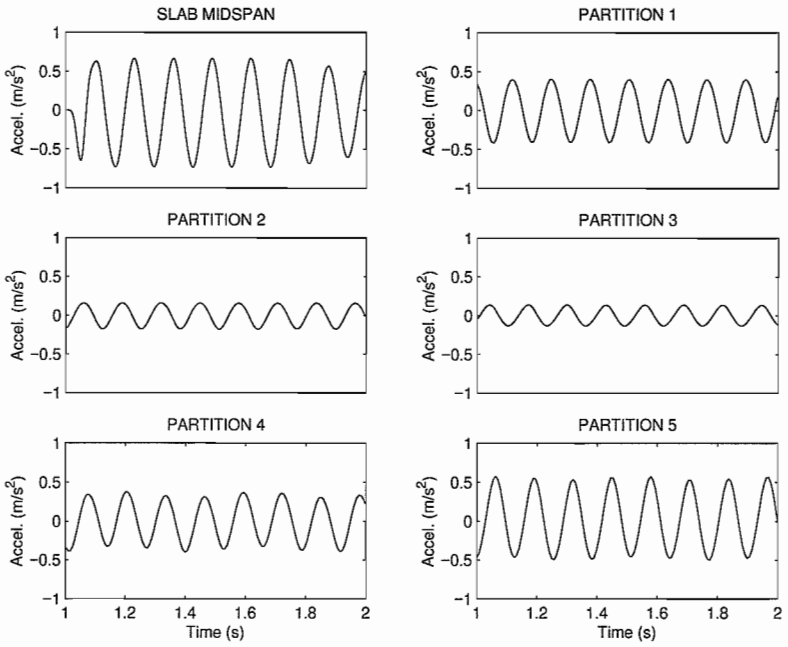

Figure 6.13: Acceleration responses at free edge of cantilever partitions (layout 1 of table 6.4), following single sine-wave loading of slab at its fundamental frequency. [see figure 3.12, page 60 for partition positions]

Figure 6.14 shows the acceleration responses of the partitions when arranged as layout 3 (table 6.4), where the individual perpendicular partitions are joined by parallel ones. This has the effect of the plasterboard acting as a single unit and aids the transfer of energy between the partitions. Hence, it is observed that the acceleration responses of individual partitions are significantly increased, when compared with layout 1. This leads to increased swaying of all partitions and, as a result of added energy dissipation, the overall damping of the slab is significantly increased.

The axial deformations of the partitions were investigated by measuring the response at the top of the partitions in the vertical direction. These effects were found to be minimal and were ignored.

Analytical model representation

In general, cantilever partitions are very light compared to the slab and so are unlikely to have a significant effect on the slab's natural frequencies and mode shapes. This was observed by comparing the slab mode shapes with and without the cantilever partitions, which were identical. Also, from table 6.4, the effect of the cantilever partitions on slab fundamental frequency can be

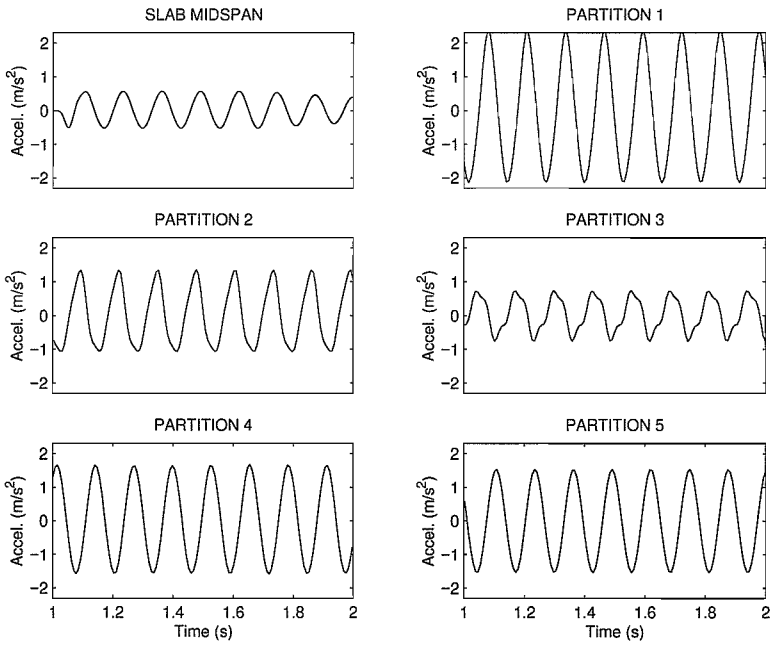

Figure 6.14: Acceleration responses at free edge of cantilever partitions (layout 3 of table 6.4), following single sine-wave loading of the slab at its fundamental frequency. [see figure 3.12, page 60 for partition positions]

seen to be minimal. However, the experimental results show some swaying of the partitions, which will dissipate energy and hence will add to the overall damping of the system.

In this section, it is assumed acceptable to model the partition in isolation rather then modelling the entire system. This is justifiable because of the very large mass difference, as explained above. Hence, the motion of a cantilever partition can be analysed by considering a fixed-free beam with a sinusoidal rotation applied at the base. As shown in figure 6.15, such a beam can be divided into a cantilever undergoing free vibration, and a rigid beam undergoing base rotation. In the following section, the response of the beam in figure 6.15(c) is derived using generalised coordinates and the mode summation procedure.

The undamped free vibration equation of motion of such a system, figure 6.15(a), is derived by considering the forces acting on an elemental length of the beam, giving:

$$EI\frac{\partial^4 u_f}{\partial x^4} + \rho A\frac{\partial^2 u_f}{\partial t^2} = 0 \tag{6.31}$$

where u_f is the free vibration displacement. Taking the rigid beam of figure 6.15(b), with a rotation at base of $\theta = \bar{\theta}\sin(\Omega t)$, the displacement of the beam at a point x will be:

$$y = \theta x = \bar{\theta} x \sin(\Omega t) \tag{6.32}$$

Hence, with the inclusion of this base rotation, (figure 6.15(c)), equation 6.31 becomes:

$$EIu'''' + \rho A\left[\ddot{y} + \ddot{u}\right] = 0 \tag{6.33}$$

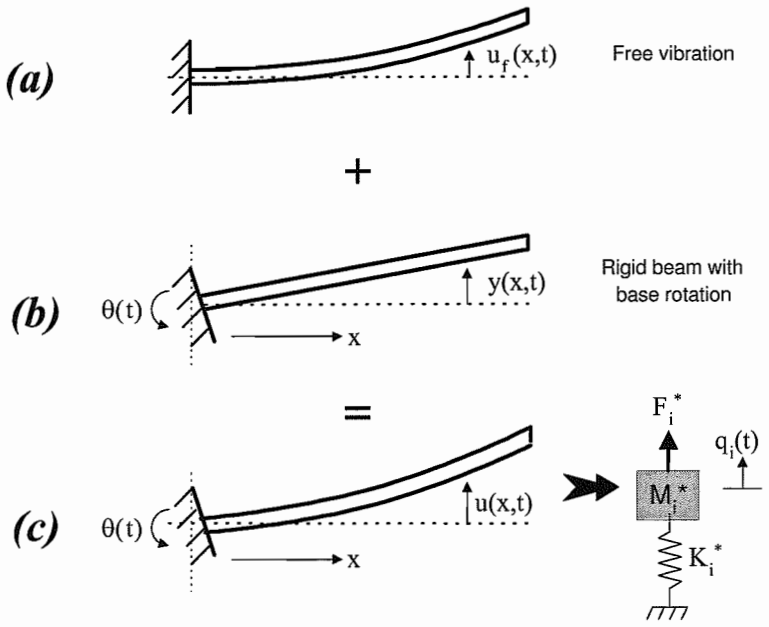

Figure 6.15: Approximation of cantilever partitions with base motion

where u' and $\dot{u}$ imply differentiation with respect to x and t respectively. Rearranging equation 6.33 gives:

$$EIu'''' + \rho A\ddot{u} = -\rho A\ddot{y} \tag{6.34}$$

This can be solved by approximating the overall response of the beam, $u(x,t)$, as the sum of n mode shapes, $\Phi_i(x)$, multiplied by a time function, $q_i(t)$ (see equation 6.16). For a cantilever beam, the mode shapes are given by:

$$\Phi_i(x) = C\left\{\cosh(\beta_i x) - \cos(\beta_i x) - \alpha_i\left[\sinh(\beta_i x) - \sin(\beta_i x)\right]\right\} \tag{6.35}$$

where C is an arbitrary amplitude constant and

$$\beta_i^4 = \frac{\omega_i^2 \rho A}{EI} \qquad \text{and} \qquad \alpha_i = \frac{\cosh(\beta_i L) + \cos(\beta_i L)}{\sinh(\beta_i L) + \sin(\beta_i L)} \tag{6.36}$$

As for full-height partitions, the principle of generalised coordinates can be used, where the beam is approximated to an equivalent SDOF system, (figure 6.15), represented by equation 6.17. The generalised mass, M_i^*, is derived from equation 6.18 and the generalised force is: (see equation 6.20)

$$F_i^* = \int_0^L -\rho A\ddot{y}(t)\Phi_i(x)dx = \int_0^L -\rho A\ddot{\theta}x\Phi_i(x)dx \tag{6.37}$$

Hence, substituting M_i^* and F_i^* into equation 6.17 and rearranging, gives the equation for the generalised coordinate q_i:

$$\ddot{q}_i + \omega_i^2 q_i = \frac{F_i^*}{M_i^*} = \frac{\rho A\Omega^2\bar{\theta}\sin(\Omega t)}{M_i^*}\int_0^L x\Phi_i(x)dx \tag{6.38}$$

which can be written as:

$$\ddot{q}_i + \omega_i^2 q_i = J_i \sin(\Omega t) \qquad \text{where} \qquad J_i = \frac{\rho A \Omega^2 \bar{\theta}}{M_i^*} \int_0^L x\Phi_i(x)dx \tag{6.39}$$

Using integration by parts and equation 6.35, the term in the integral is:

$$\int_0^L x\Phi_i(x)dx = \frac{C}{\beta_i}\left[\left(-L\alpha_i - \frac{1}{\beta_i}\right)\left(\cosh(\beta_i L)+\cos(\beta_i L)\right) + \left(L+\frac{\alpha_i}{\beta_i}\right)\sinh(\beta_i L) - \left(L-\frac{\alpha_i}{\beta_i}\right)\sin(\beta_i L) + \frac{2}{\beta_i}\right] \tag{6.40}$$

The steady-state solution of equation 6.39 will be harmonic and can be expressed as: $q_i = Q_i \sin(\Omega t)$. Its substitution into equation 6.39 yields:

$$Q_i = \frac{J_i}{\omega_i^2 - \Omega^2} \qquad \text{hence:} \qquad q_i = \frac{J_i}{\omega_i^2 - \Omega^2}\sin(\Omega t) \tag{6.41}$$

To express response in terms of acceleration, substitution of equation 6.41 into 6.39 gives:

$$\ddot{q}_i = J_i \sin(\Omega t)\left(1 - \frac{\omega_i^2}{\omega_i^2 - \Omega^2}\right) \tag{6.42}$$

so that the total acceleration response of the partition, due to a rotation at the base, is given by:

$$\ddot{u}(x,t) = \sum_{i=1}^{n} \ddot{q}_i(t)\Phi_i(x) = \sum_{i=1}^{n} J_i \Phi_i(x)\sin(\Omega t)\left(1 - \frac{\omega_i^2}{\omega_i^2 - \Omega^2}\right) \tag{6.43}$$

For the experimental gypsum plasterboard, four-point loading tests gave an average EI value of 1671Nm^2, and the density of the partitions was obtained from their mass to be 584kg/m^3. These values had an error range of approximately $\pm 10\%$. Figure 6.16 shows a typical model response at the free end, assuming the vibration history of the slab as the applied rotation. Note that the frequency of the response is dominated by the frequency of slab vibration. Figure 6.17 shows the response profile of the partition, as derived by the model.

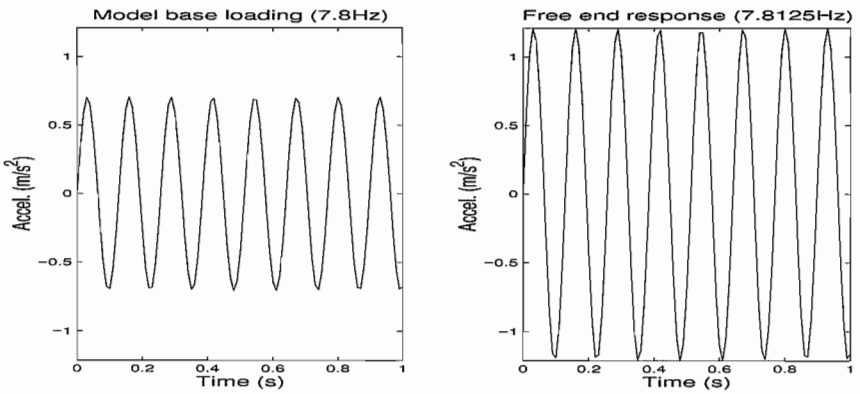

Figure 6.16: Model response at the free end of cantilever with base motion

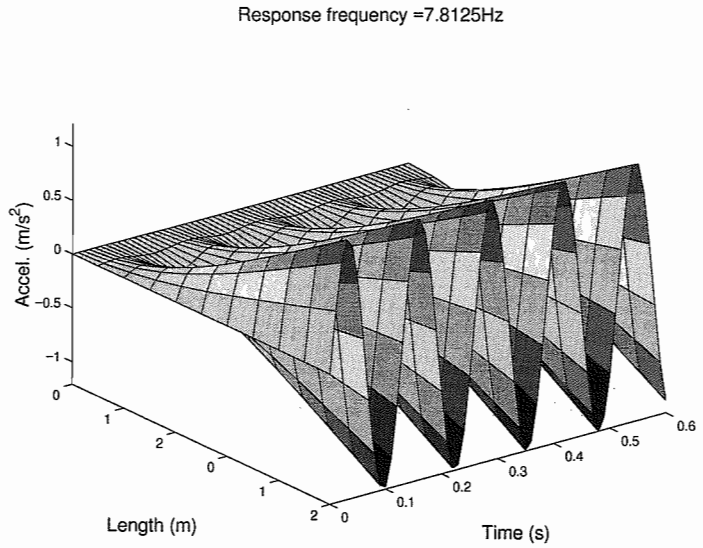

Figure 6.17: Model response profile of cantilever beam with base motion

To further investigate the effect of base motion, the free vibration response of a cantilever beam, with identical material properties, was derived using equation 6.35 as the mode shape. Figure 6.18 shows a comparison of the FFTs of the beam with and without base motion. Notice that the frequency of the slab, Ω, governs the vibration response of the partition.

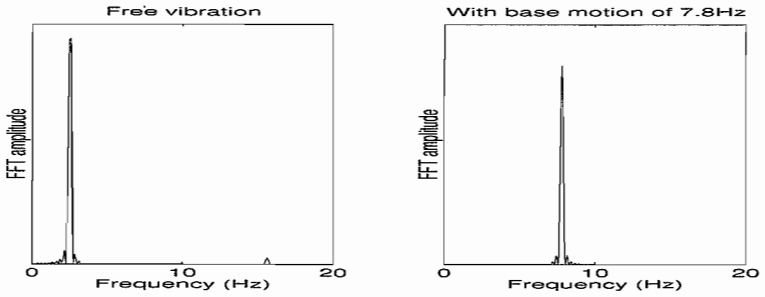

Figure 6.18: FFTs of the partition response at its free end

With respect to the experimental results, as illustrated in figure 6.19, the amplitude of base rotation is dependent on the position of the partition along the slab. This can be found from the measured vertical acceleration response of the slab. Assuming a mode shape function for the slab in the form $\Phi(x) = \sin\frac{\pi x}{L}$, and that the slab displacement response is given by $u = U\sin\omega t$, the response at any point, x, along the slab would be $v = u\sin\frac{\pi x}{L}$. Hence, the rotation of the slab at x is dependent on the slope and can be expressed as:

$$\theta = v' = \frac{u\pi}{L}\cos\frac{\pi x}{L} = \frac{U\pi}{L}\cos\frac{\pi x}{L}\sin\omega t \qquad \text{so that} \qquad \bar{\theta} = \frac{U\pi}{L}\cos\frac{\pi x}{L} \tag{6.44}$$

where U can be found from the measured acceleration responses of the slab at midspan. From equation 6.44, it can be deduced that at slab midspan (i.e. $x = \frac{L}{2}$), the motion is purely vertical with no apparent rotation amplitude (i.e. $\bar{\theta}$=0). At other points along the slab, the rotation applied at the base of each partition can be derived.

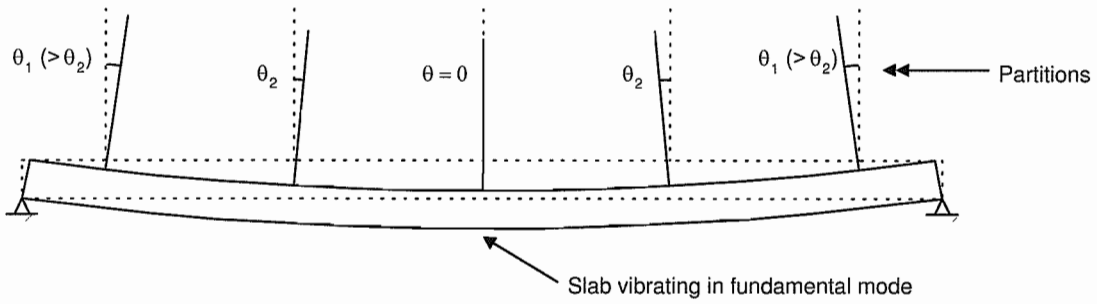

Figure 6.19: Effect of slab mode shape on base rotations of partitions

Given the midspan vibration amplitude for the slab of figure 6.13, the base rotation applied to each cantilever partition and the model acceleration response of the partition at its free edge are shown in figure 6.20. For comparison, the experimentally measured responses of figure 6.13 are also plotted for each partition. It can be seen that the model prediction of the responses is generally satisfactory, with best agreement obtained for partitions 4 and 5. Possible causes for discrepencies in the results could be the range of variability of the measured plasterboard stiffness and density values, and the representation of fixed boundary conditions in the experiments. Note that for the partition at midspan, part 3, although the model gives zero response, experiments show some swaying of the partition. This could be because the partition was not exactly at slab midspan, hence experiencing a small amount of base rotation.

From the above results, this model is seen to be capable of predicting, to an acceptable degree, the amount of swaying which can take place as a result of an applied rotation at the base of the cantilever partition. The applied rotation is itself dependent on the slab response and the positioning of the partition with respect to the fundamental mode shape of the slab.

From the experimental and model results, it is evident that the placement of the cantilever partitions along the slab has an influence in their lateral swaying response. The larger the response, the higher the energy dissipation and the greater the liklihood of increased overall slab damping, as seen in table 6.4. The results have also shown that the response of the cantilever partitions is greater at a point on the slab where higher rotational base motion is applied. The analytical model has shown that the frequency of slab vibration has a governing influence on the natural modes of the partitions. Finally, experiments have shown that if the cantilever partitions are connected to each

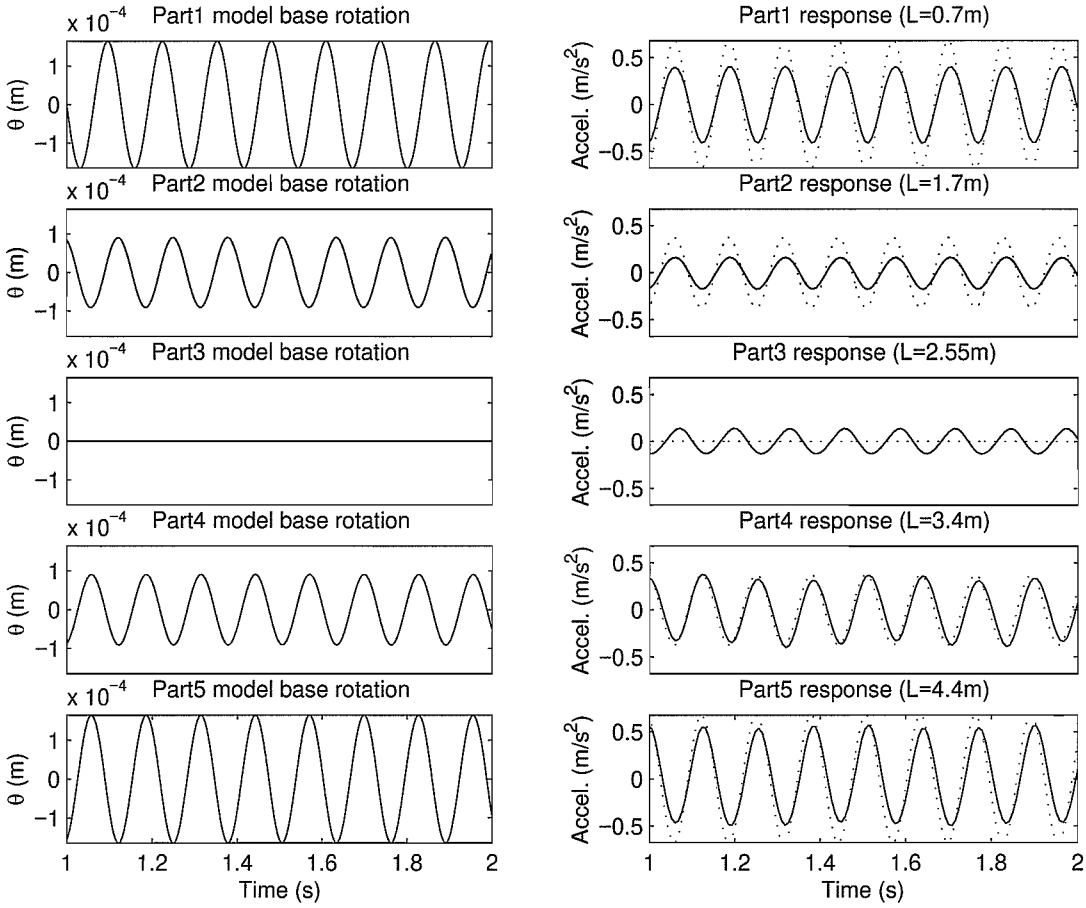

Figure 6.20: Comparison of model beam response with experimental results at the free end of the partitions (model responses drawn as dotted lines)

other, transfer of energy takes place from ones with higher response to ones with lower response, increasing the overall energy absorption of the whole partition system. This increase is seen to be higher than the responses of the partitions when not connected (see figures 6.13 and 6.14).

6.5 Effect of viscoelastic screed layers

As explained in section 3.6.7, two 25mm layers of concrete screed, treated with Concredamp viscoelastic additive, were cast on the model slab. In this section, results from vibration tests on the treated slab are presented. An analytical model is devised to represent the changes following the addition of the layers. First, the material characteristics of the treated concrete are presented.

6.5.1 Screed layer properties

As with the model slab, cube and cylinder samples were cast following the mixing of the Concredamp screed layers. Table 6.6 illustrates the results obtained, which show a reduction in strength depending on the concentration of Concredamp and the amount of water in the mix. Reductions in Young's modulus and density were also observed. During measurements of Young's modulus for the first screed layer, it was found that the specimen cylinder was defective, hence readings for this case were inaccurate and are not included in table 6.6.

The low values of concrete strength and Young's modulus were attributed to problems encountered in the casting process (see section 3.6.7, page 63). Although this was also observed by others [Weiss (1989), O'Rourke & Son Ltd. (1993)], they conducted trials and managed to obtain the correct mix of lower strength but the right Young's modulus. This was not achieved during these tests and the difference in results described here bear no reflection on the useability of Concredamp, but may mainly be due to the casting and pouring procedures used in the laboratory.

In addition, vibration tests were conducted on sample beams to derive their damping characteristics. These tests are explained in section 4.7 and the results are presented in table 6.6, which show an increase in damping following the addition of Concredamp, depending on concentrations used.

Table 6.6: Concrete properties and damping characteristics of concrete treated with viscoelastic admixture (Concredamp)

Test	Average concrete cube strength (N/mm^2)	Average Young's modulus (kN/mm^2)	Average density (kg/m^3)	Average beam damping (% critical)
(i) untreated concrete (as per model slab)	45	25.6	2340	4.65
(ii) screed layer 1 Concredamp conc. of $50l/m^3$	20	not available	1980	4.78 [+3% of (i)]
(iii) screed layer 2 Concredamp conc. of $85l/m^3$	29	17.8	2160	4.92 [+6% of (i)]

6.5.2 Effect on model slab vibration

Results of tests, with the screed layers on the slab, are given in chapter 5 and appendix A. Table 6.7 is a summary of the average natural frequency and damping measurements. Note that the screed has the effect of increasing the cross-sectional area of the slab, and hence may be regarded as a structural addition. This is clearly seen by the increase in natural frequency, which is consistent with predicted values using the EBM (see appendix D).

Table 6.7: Effect of screed layers on slab vibration properties in the fundamental mode

Slab configuration	Fundamental frequency (Hz)		Damping (% critical)	
	experimental	theoretical	experimental	% change
(i) bare slab (fully tensioned)	8.0	8.0	1.10	-
(ii) bare slab with first screed layer	8.8	9.0	1.15	+5% of (i)
(iii) bare slab with first and second screed layers	10.1	10.2	1.25	+14% of (i)

The theoretical values in table 6.7 are based on the screed layers being fully structural integrated onto the slab; the section was then transformed to that of the slab. The material properties used for both layers are that of the second layer, given in table 6.6. Experimentally, the screed layers have differing properties and the bond between the screed and the main slab was not fully established, which leads to a reduction in natural frequency, since the screed acts as dead load. The assumption that the screed layers are exactly 25mm thick, could also lead to differences between predicted and experimental frequencies. In reality, the thickness varied along the slab by ±10mm.

Also from table 6.7, it is observed that the damping values of the slab increase as a result of screed addition. However, the increase is less than was expected. This may be due to the properties of the treated concrete mix used in the tests. In the following section, a model is derived to represent the addition of viscoelastic layers on a concrete floor slab.

6.5.3 General considerations and theoretical model

Possible types of viscoelastic treatment

The behaviour of a viscoelastic material may be explained by considering the properties of elastic and viscous materials separately. In a perfectly elastic material, stress is proportional to strain ($\sigma = E\epsilon$) so that the system is conservative and the energy stored is independent of the rate of loading. In a perfectly viscous material, however, stress is a function of the rate of change of strain ($\sigma = k\dot{\epsilon}$) so the energy stored depends on the rate of loading. In an actual material, the stress is a combination of the elastic and viscous behaviour ($\sigma = E\epsilon + k\dot{\epsilon}$). Here, $k\dot{\epsilon}$ is a measure of the damping of the system. Normally $k\dot{\epsilon}$ is small and it is common to assume a structure to act elastically with some inherent viscous damping, hence the term $k\dot{\epsilon}$ is ignored. However, in some materials, the viscous term can be substantial and should not be neglected. These types of material are known as viscoelastic and possess high internal damping. When viscoelastic materials are used for vibration control, they are mainly applied in layers and are subjected to shear or direct strains.

The use of viscoelastic layers to increase damping is mainly confined to mechanical engineering applications, which involve high intensity sources of wide frequency band excitation, such as rocket or jet aircraft noise. Most practical configurations may be considered as variations of two basic arrangements. In the first case, the viscoelastic (dissipative) material is applied in a uniform layer to a sheet or bar of a relatively nondissipative material, such as metal. When the composite is bent, the viscoelastic layer deforms essentially in extension and compression. Thus, it stores energy and supplies damping, due primarily to this mechanism. This type of viscoelastic layer is called a *free* or *unconstrained* layer and its damping action is termed extensional damping. It is the type attempted on the model concrete slab, although the viscoelastic behaviour of the screed layers was seen to be minimal due to the reasons explained in the previous section. The second type of treatment can be more effective, with higher composite damping, and is termed *constrained* layer or shear damping. Here, a viscoelastic layer lies between, and is rigidly connected to, two elastic structures. Bending of this composite causes the viscoelastic layer to deform primarily in shear.

Application of viscoelastic treatment in civil engineering to damp vibrations is not very common, mainly because the amplitudes are small. In cases where it has been utilised, excellent results have been obtained [Nelson (1968), Farah et al. (1977), Ibrahim and Farah (1978)]. For floor slabs, the constrained layer treatment has been adopted on composite construction only, where the viscoelastic material has been applied at the bottom flange of the steel beams. The case of free layer treatment on concrete floors is less common and only one successful application has been reported [Moiseev (1991)]. In the following section, a theoretical analysis, using energy considerations, is presented to assess the effectiveness of such treatment on concrete floor slabs.

Free layer damping analysis

Figure 6.21 shows an elementary length of a two layered composite structure with different material properties for each layer. Layer 2 in the figure can be regarded as the screed in the model tests, while layer 1 can represent the model concrete slab. As the tests showed the screed to have relatively little viscoelastic behaviour (see section 6.5.1), the following analysis assumes both layers to undergo elastic deformation with some inherent viscous damping. Hence, the energy stored due to the bending of each layer is assumed to be elastic strain energy only, with pure viscous behaviour ignored.

Assuming full bonding between the two layers of figure 6.21, the neutral axis CC of the composite

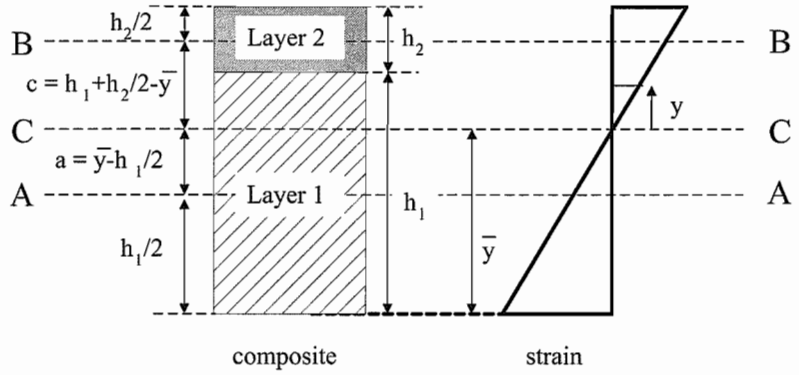

Figure 6.21: A two layered composite structure showing the neutral axis (CC) and the centroidal axis of each component (AA for layer 1 and BB for layer 2)

system is given by:

$$\bar{y} = \frac{h_1 b\frac{h_1}{2} + \frac{E_2}{E_1}h_2 b\left(h_1 + \frac{h_2}{2}\right)}{h_1 b + \frac{E_2}{E_1}h_2 b} = \frac{\frac{E_1 h_1^2}{2} + E_2 h_2\left(h_1 + \frac{h_2}{2}\right)}{E_1 h_1 + E_2 h_2} \tag{6.45}$$

Under bending, the strain at a point y in the composite is expressed as $\epsilon = \frac{y}{R}$, where R is the radius of curvature. Similarly, the stress at y is given by $\sigma = E\epsilon = \frac{Ey}{R}$. Hence, the stored strain energy at y due to the bending of an elementary volume dV is:

$$S = \int \frac{1}{2}\sigma\epsilon dV = \int \frac{1}{2}\frac{Ey^2}{R^2}dV \tag{6.46}$$

Now consider the energy stored in each individual layer where:

$$S_1 = \int_{-\bar{y}}^{h_1-\bar{y}} \frac{1}{2}\frac{E_1 y^2}{R^2}bLdy \rightarrow \frac{S_1}{L} = \frac{1}{2}\frac{E_1}{R^2}\int_{-\bar{y}}^{h_1-\bar{y}} y^2 dA = \frac{1}{2}\frac{E_1 I_1}{R^2} \tag{6.47}$$

and

$$S_2 = \int_{h_1-\bar{y}}^{h_1+h_2-\bar{y}} \frac{1}{2}\frac{E_2 y^2}{R^2}bLdy \rightarrow \frac{S_2}{L} = \frac{1}{2}\frac{E_2}{R^2}\int_{h_1-\bar{y}}^{h_1+h_2-\bar{y}} y^2 dA = \frac{1}{2}\frac{E_2 I_2}{R^2} \tag{6.48}$$

where the second moments of area are about the neutral axis CC of the composite section. With reference to figure 6.21, these are:

$$I_1 = I_{1,CC} = I_{1,AA} + bh_1 a^2 \qquad \text{and} \qquad I_2 = I_{2,CC} = I_{2,BB} + bh_2 c^2 \tag{6.49}$$

Having obtanied the energy stored in each layer, the overall damping of the composite can be taken as a weighted average of the damping ratios of the individual elements [Ungar (1963)], such that:

$$\zeta = \frac{\sum(\zeta_i S_i)}{\sum S_i} \tag{6.50}$$

where S_i is the energy stored by the ith component and ζ_i is its damping ratio. Substitution of equations 6.47 and 6.48 into 6.50 will give the overall damping of the two layered composite as:

$$\zeta = \frac{\zeta_1 E_1 I_1 + \zeta_2 E_2 I_2}{E_1 I_1 + E_2 I_2} \tag{6.51}$$

In the context of the experimental Concredamp screed layers, equation 6.51 can be regarded as a representation of the two screed layers on the slab. From table 6.6, assuming both layers to have properties equal to those of screed layer 2, figure 6.22 shows the original slab with and without the screed layers and a summary of the values involved in the analysis. In the figure, ζ_2 is extrapolated from the given values of tables 6.6 and 6.7.

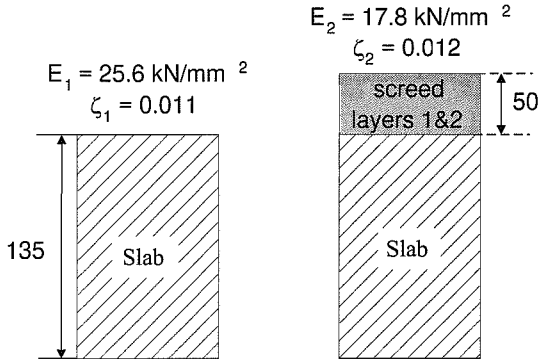

Figure 6.22: Summary of slab and screed layer properties

Substituting the relevant parameters into equation 6.51, gives an overall damping with both screed layers of 1.12% critical. This compares with an experimentally derived value of 1.25% (table 6.7). The relatively large discrepency would be expected, as this analysis does not account for the effects of cracking due to the addition of the screed layers. The extra mass of the layers would increase the microcracks in the main slab, hence increasing its overall damping (see section 6.2.2). Other reasons for the difference in the values could be due to imperfect bonding of screed layer and slab, and the variations in the thicknesses of the layers. In addition, difficulties encountered in the casting process of the Concredamp layers could affect the results (see section 6.5.1).

Ideally, for the dissipative layer to be fully effective it must possess viscoelastic behaviour such that ζ_2 would be much larger than ζ_1, hence increasing the overall damping of the composite. A far better method, than the free layer treatment, is the use of a constrained viscoelastic layer between the slab and another elastic layer. In this way, use can be made of energy loss due to shear. The use of such systems has had particular attention in mechanical engineering applications [Kerwin (1959), Mead and Markus (1969), Rao (1978)]. However, no reports are available on the implementation of a constrained viscoelastic layer to damp vibrations of concrete slabs. This can lead to the possibility of research on such an application, and is described further in section 10.4.

6.6 Model slab accelerations

In this section, the derived acceleration measurements of chapter 5 are analysed, with respect to current perceptibility guidelines, and the different floor configurations are classified. The response of the model floor was measured following three types of loading, namely: continuous sinusoidal vibration at the fundamental frequency, heeldrop, and walking excitations. For each test, the acceleration readings are plotted in the CSA (1989) and [ISO2631/2 (1989), BS6472 (1984), ANSI S3.29 (1983)] vibration perceptibility graphs (see section 2.2.2).

6.6.1 Continuous vibration tests

These tests are explained in section 5.7.1, where the slab was excited at its fundamental frequency with a loading of more than 20 cycles. It can hence be regarded as a continuous vibration in the perceptibility guidelines. The derived acceleration amplitudes are given in table 5.8 (page 98), for each tested slab configuration. For most cases, the excitation was imposed at two differing amplitudes, varying from $\pm$5N to $\pm$30N (see table A.35, appendix A). To obtain a representative acceleration response, a loading of $\pm$15N is assumed for the perceptibility guides of this section. In this way, a consistent set of acceleration readings may be derived for each slab configuration.

Figures 6.23-6.29 show the results obtained by plotting the slab accelerations in the two guidelines at each stage. The values of fundamental frequency are average readings taken from tables 5.1-5.6, (page 94). In the CSA (1989) guide, readings above the continuous vibration iso-perceptibility line are deemed to cause unsatisfactory vibration. In the ISO/BSI/ANSI curves, the acceptability of the floor is dependent on type of use, and hence reference must be made to table 2.2 (page 15), for classification of the slab.

Note that the slab was originally designed as a slender structure, exhibiting annoying vibrations. Figures 6.23-6.27 show that when fully tensioned, the slab is classified as unsatisfactory by both guides. The effect of prestressing can be seen in figure 6.23, where the acceleration response increases by 385% due to an increase of prestressing force of 75%. This illustrates the detrimental effect of post-tensioning on the vibration serviceability of concrete floors.

After each change to the slab configuration, the addition of non-structural components is seen to reduce the acceleration amplitudes by varying amounts. Figure 6.24 shows that false floor layout 2, with some loose panels, reduces response by 73% as opposed to 35% for layout 1 with rigid panels. Note that layout 2 has double the mass of layout 1. By far the most significant improvement to

response is seen following the addition of full-height partitions (figure 6.25), where in both guides the slab becomes acceptable for residential use. Significant improvement is also observed with a stationary occupant on the slab (figure 6.26). Some combinations of components are also given in figures 6.28 and 6.29, which again show improvements to slab acceptability.

The overall impression from figures 6.23-6.29 is that apart from the case of full-height partitions, the model floor falls in the unsatisfactory range in both guides, for the particular loading case. However, the level of unacceptability varies between the two guides. The CSA (1989) guide is essentially relevant to quiet or residential occupancies, while the ISO/BSI/ANSI guide applies to occupancies ranging from critical working areas (base curve) to workshops (8×base curve) and as such, the classification of the floor lies within a large range.

In general, the effect of continuous vibration should be dealt with at the source. The perceptibility guides become more useful when considering occupant activities on a floor, such as walking or jumping, which are intermittent or transient vibrations. Hence, the acceleration readings, given for continuous vibration at the slab fundamental frequency, will be much higher than those encountered within the structure due to occupant activities. Since the loading amplitude of ±15N has a significant effect on the response, these results should be viewed more with respect to the changes caused by non-structural components, than with the response readings.

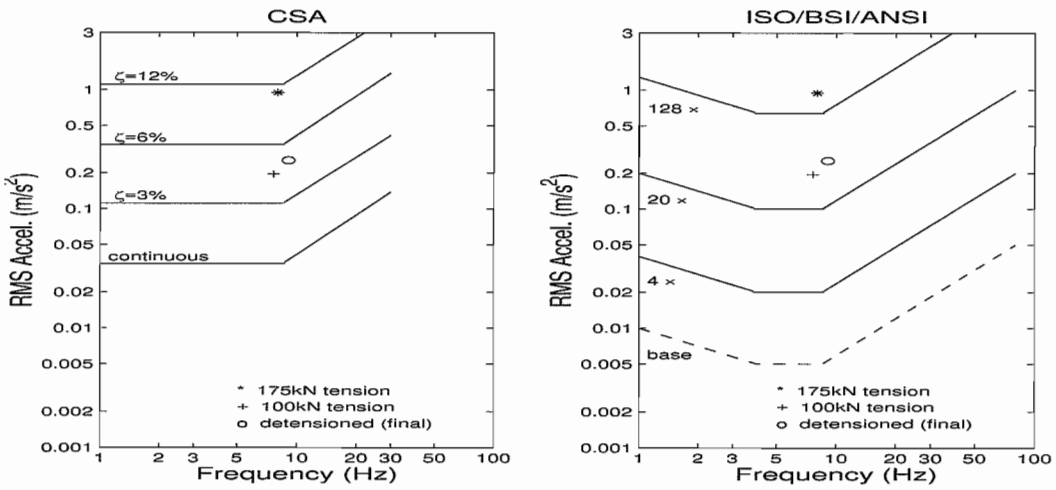

Figure 6.23: Assessment of the effect of prestressing force in perceptibility guides

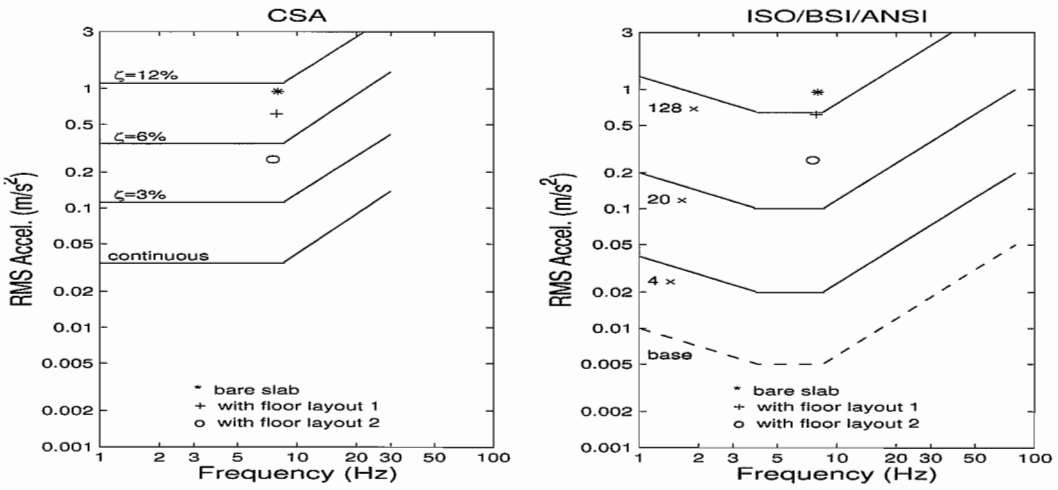

Figure 6.24: Assessment of the effect of false flooring in perceptibility guides

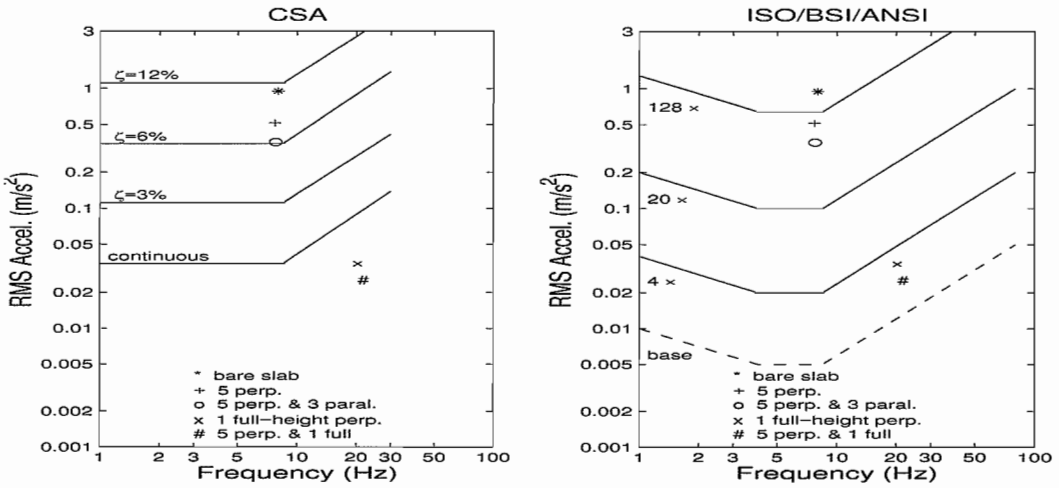

Figure 6.25: Assessment of the effect of partitions in perceptibility guides

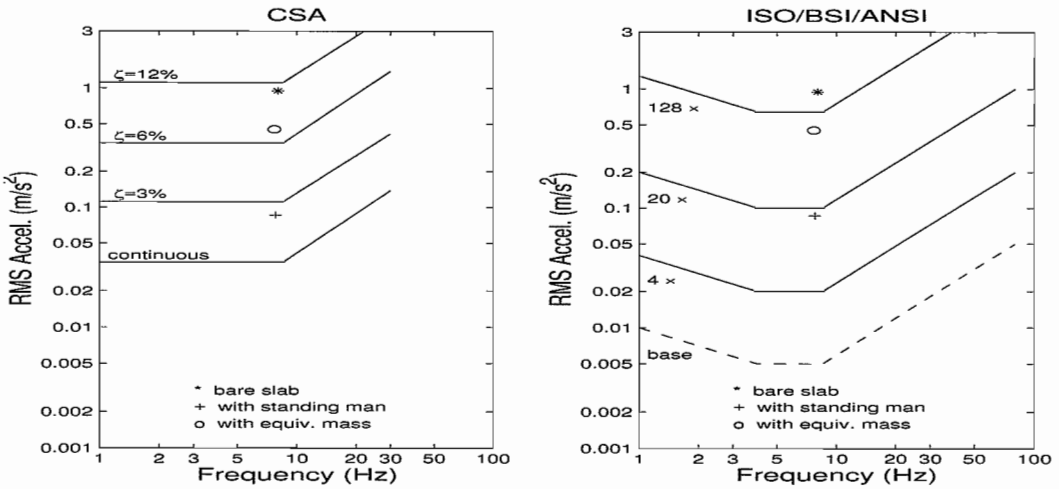

Figure 6.26: Assessment of the effect of stationary occupant in perceptibility guides

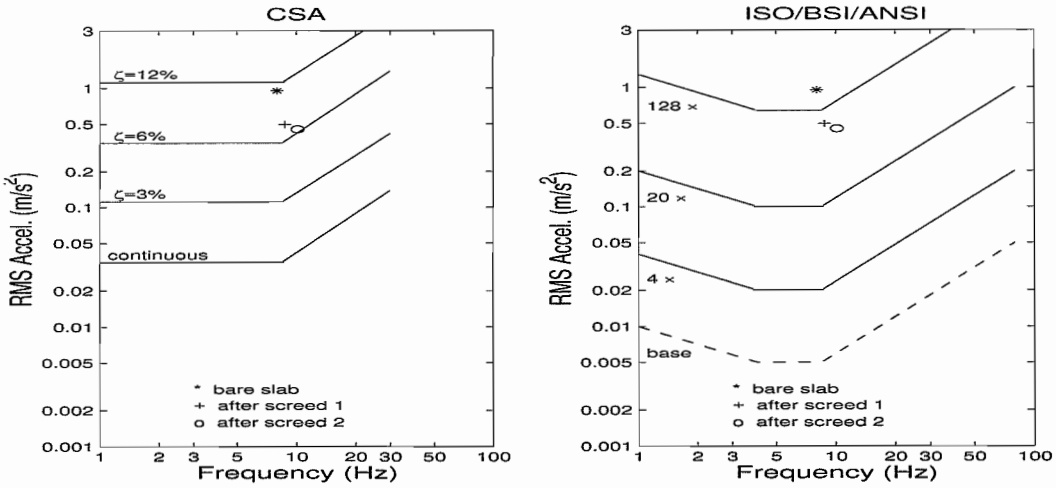

Figure 6.27: Assessment of the effect of screed layers in perceptibility guides

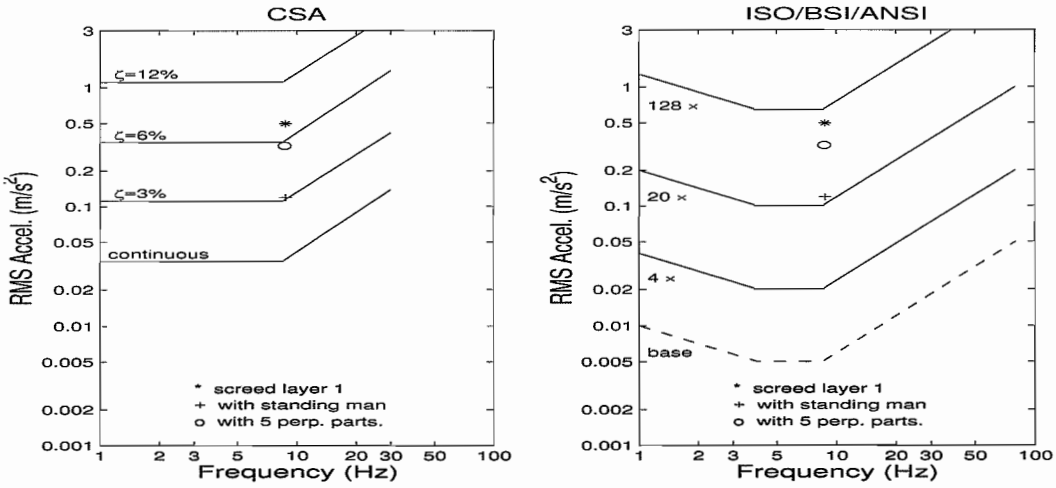

Figure 6.28: Assessment of perceptibility due to combination of components on first screed layer

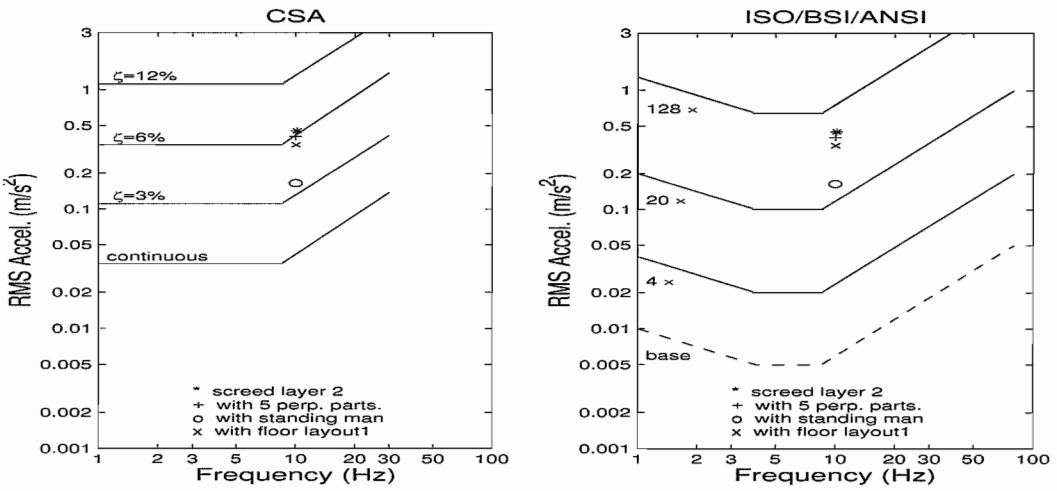

Figure 6.29: Assessment of perceptibility due to combination of components on second screed layer

6.6.2 Walking vibration tests

As explained in section 5.7.2, these tests were conducted as horizontal walking and on-the-spot walking. The resulting RMS acceleration amplitudes are given in tables 5.9 and 5.10 (page 99), and plotted in the perceptibility guides in figures 6.30 and 6.31. Note that in general, slightly higher responses are recorded as a result of walking on-the-spot. This would be expected as a larger vertical force component is being input onto the slab. In the CSA scales, the slab damping iso-perceptibility lines can be used, as the walking was generally less than 10 paces. Taking an average damping for the model slab of ζ=1.5%, it is observed that the slab is classified as unsatisfactory for two of the four conditions in these scales.

With reference to table 2.2 (page 15), the ISO/BSI/ANSI curves give a range of occupancy for the floor before its vibration performance can be classified. Assuming walking as an intermittent vibration source, these scales are seen to be more severe than the CSA scales. This is because the CSA scales are based on heeldrop loading, which imposes a larger force compared to walking. In general, the ISO/BSI/ANSI curves are seen to be a more suitable assessment method for walking as they take account of the loading, and are applicable to different occupancy types.

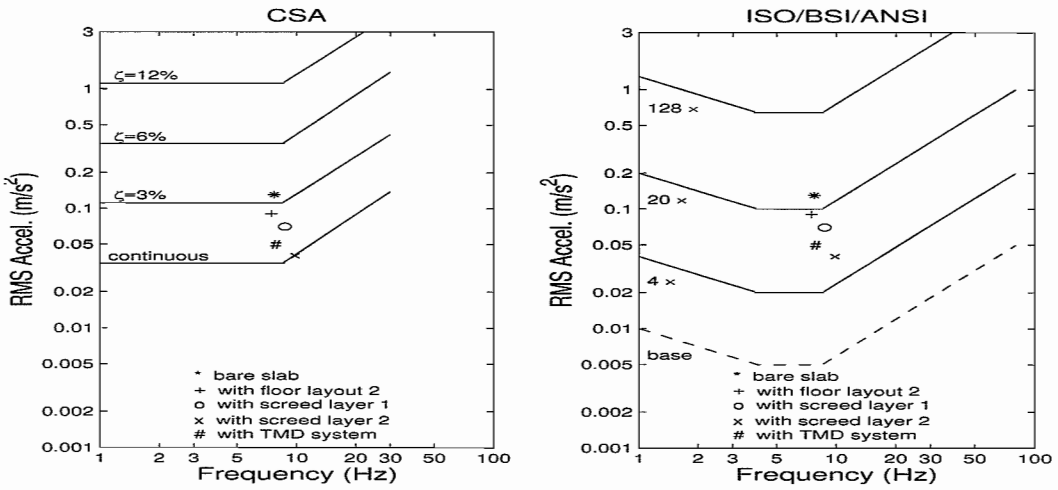

Figure 6.30: Classification of perceptibility scales from horizontal walking

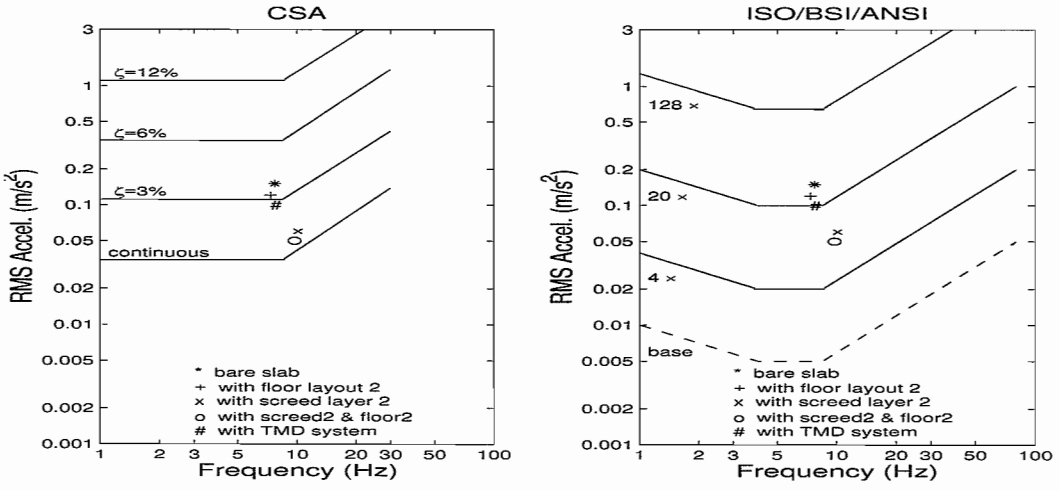

Figure 6.31: Classification of perceptibility scales from walking on the spot

6.6.3 Heeldrop loading tests

This is a transient type of vibration on which the CSA (1989) curves are based. The floor response results following heeldrop loadings are given in table 5.7 (page 97). Figure 6.32 shows these measurements plotted in the perceptibility guides. Again, the CSA guide classifies the slab as unsatisfactory for residential or quiet occupancies. From table 2.2 (page 15), for transient loading, the ISO/BSI/ANSI curves classify the slab as satisfactory for office and workshop environments and also for some residential occupancies during daytimes. Hence, the biggest difference in the classification of the two scales, is observed in the heeldrop tests. For the ISO/BSI/ANSI curves, table 2.2 shows that a large range exists for the acceptability due to transient loading, particularly for residential occupancies. The choice of a suitable base curve weighting factor depends on the location and the amount of outside activity, and as such can be very arbitrary.

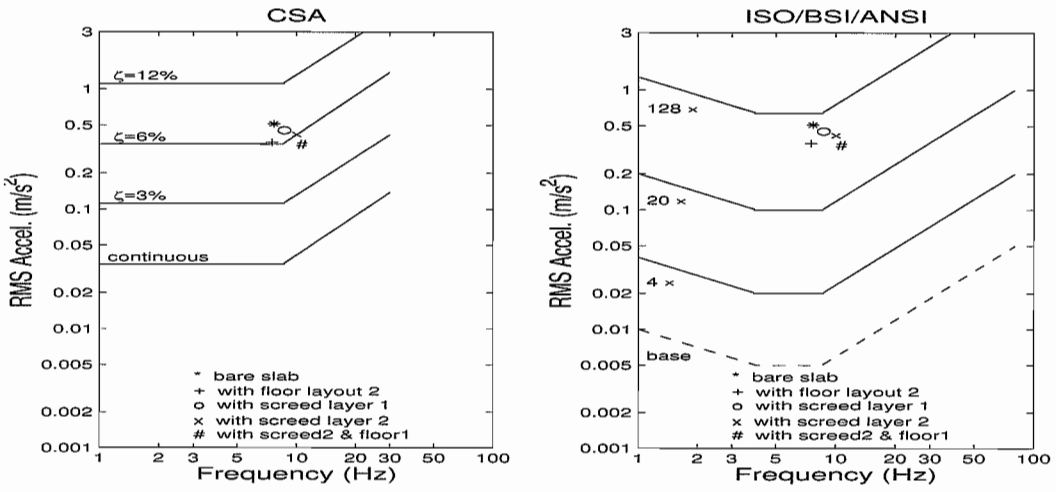

Figure 6.32: Classification of perceptibility scales from heeldrop loading

Chapter 7

A simple TMD for concrete floors

7.1 Introduction

As explained in section 2.6.5, tuned mass dampers, TMDs, have mainly been used in buildings and bridges [McNamara (1977), Bachmann (1992a)]. For maximum effect, the use of TMDs would be recommended in situations where the primary structure has high displacement amplitude and low damping and where annoying vibrations occur due to the forcing frequency being in resonance with one distinct mode of the structure only. Many floor slabs, however, exhibit closely spaced modes of vibration with relatively low displacement. In addition, since the TMD consists of a mass that should be placed near the point of maximum displacement (i.e. middle of simply supported floor), this raises problems with its location on a floor. Hence, the application of TMDs on floor slabs has not been widespread and problematic floors have generally been treated by stiffening the structure. Some applications of TMDs on floors have been reported [Setareh and Hanson (1992b), Webster and Vaicaitis (1992)] with reductions in vibration amplitude of up to 78%. However, almost all of these cases have involved cantilever type floors, such as balconies, with high displacement at the free end. In these cases, the TMD was placed in a cabinet at the free edge.

In the research programme described herein, experiments have been performed in an attempt to apply a TMD system on a simply supported slab at its mid-span. The idea was originally proposed by Allen and Pernica (1984) for composite slabs and is modified and extended here for post-tensioned concrete floors. The results show acceptable levels of vibration reduction, as described in section 7.3. Two possible mathematical models for such a system are also proposed, which take the form of a numerical time-stepping method and a closed-form analytical solution. Predictions of the experimental results, using these models, were seen to be acceptable to varying degrees. Following correlations between the experimental and model results, a possible design guideline is presented, which is applicable to any problematic floor.

7.2 Description of the proposed TMD system

The vibration absorbers used were in the form of flat plywood sheets simply supported from the underside of the slab, with weights on top. The weights were placed at the mid-span of the plywood, where maximum displacement occured. The TMD configurations used were:

- one sheet (1.2m×1m×10mm) hereafter referred to as **'wideply'**
- two sheets of wideply on top of each other with nothing in-between
- two sheets of wideply on top of each other with polythene in-between
- two sheets of wideply on top of each other with hard rubber in-between
- one sheet (1.2m×0.3m×10mm) hereafter referred to as **'narrowply'**
- two sheets of narrowply on top of each other with nothing in-between
- two sheets of narrowply on top of each other with polythene in-between
- two sheets of narrowply on top of each other with hard rubber in-between

The purpose of having different material in-between sheets of ply was to assess the changes in damping that may occur as a result of altering the friction between the layers.

7.2.1 Effect of TMDs on floor vibration

A vibration absorber is an oscillator of much smaller mass, m_2, than that of the floor structure, m_1, but with the same natural frequency. Figure 7.1 shows the resulting natural vibration of an idealised floor system following an initial velocity on the slab, equivalent to a single footstep impulse. Figure 7.1(a) shows the undamped natural vibration of the idealised floor system without a vibration absorber. When a vibration absorber is attached to the floor and tuned to its troublesome frequency, the energy of natural vibration of the floor is transferred back and forth between the floor and the absorber. Figure 7.1(b) shows this transfer of energy for an undamped system with a tuned TMD, which shows that a *beating* vibration of the slab is produced due to this energy transfer.

All real TMDs exhibit some amount of damping. If the damping in the absorber, ζ_2, is the same as the damping in the floor, ζ_1, no more energy is dissipated than would be without the absorber and although a better performance is observed, the maximum vibration amplitudes during beating are not decreased, (figures 7.1(c)and(d)). If the damping in the absorber is greater than that in

the floor, more energy is dissipated between beats and the absorber becomes much more effective in damping the vibration of the floor, as shown in figure 7.1(e). If damping in the absorber is very large, however, it resists displacement of the absorber mass and therefore prevents the transfer of vibration energy into the absorber, i.e. the absorber again becomes ineffective (figure 7.1(f)).

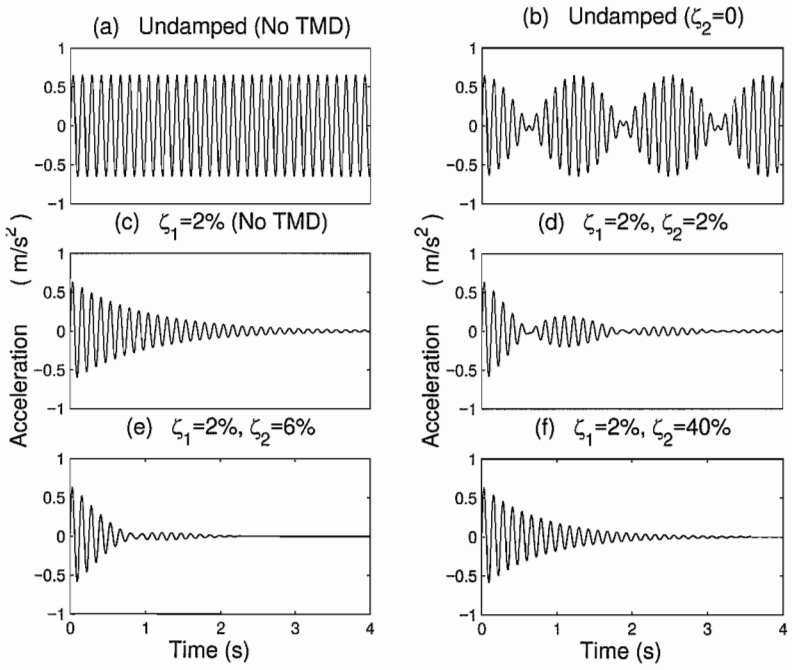

Figure 7.1: Effect of TMD on natural vibration of slab

7.2.2 Design of the proposed plywood TMDs

In general, floor slabs with fundamental frequencies of between 3-12Hz are prone to annoying vibrations due to normal human activities. For fundamental frequencies greater than this, natural vibration from footsteps is generally not annoying, because it decays very rapidly. Below this range, TMDs become less effective, because they cannot control the gradual build-up of vibration due to resonance between footstep frequency and natural frequency. The factors involved in the design of the plywood TMD system are described below.

Estimation of floor properties

The properties of the floor, in terms of theoretical lumped mass and stiffness parameters, are first calculated from known values of the concrete material properties and slab dimensions. To find the generalised lumped mass, M_1^*, and stiffness, K_1^*, of the slab, the *principle of virtual displacements*

can be used where a generalised co-ordinate describes the system. Hence, by idealising the slab as a simply supported beam with an assumed fundamental mode shape, $\Phi = \sin(\pi x/L)$, generalised slab mass and stiffness can be written as:

$$M_1^* = \int_0^L \rho A \Phi^2 dx = \rho A \frac{L}{2} \tag{7.1}$$

$$K_1^* = \int_0^L EI\Phi''^2 dx = \frac{EI\pi^4}{2L^3} \tag{7.2}$$

and the estimate of the slab natural frequency is simply $\omega_0 = \sqrt{\frac{K_1^*}{M_1^*}}$. For the model slab, M_1^* and K_1^* are calculated in appendix B.

Estimation of TMD properties

These properties can be found from the value of mass ratio, ($\mu = \frac{M_2^*}{M_1^*}$), where M_2^* is the generalised mass of the absorber. The mass ratio can typically vary within a range of 0.01 to 0.1 depending on the mass of the absorber and the required overall slab damping ratio. In general, a heavier absorber can be more effective in the reduction of floor vibrations, but there exists a limit at which any increase in TMD mass has little effect on the vibration reduction. In the experiments described, adding weights on the plywood could alter M_2^*, hence the value of μ could be changed. By assuming a starting arbitrary μ, the generalised mass of the absorber is derived by $M_2^* = \mu M_1^*$. Since it is required for the absorber to have a natural frequency equal to that of the slab (i.e. $\frac{K_1^*}{M_1^*} = \frac{K_2^*}{M_2^*}$), the value of generalised TMD stiffness, K_2^*, can also be found.

Damping in slab and absorber

In designing sophisticated TMDs for buildings and bridges, an optimum damping ratio for the absorber is derived, which depends on the chosen mass ratio. Adequate viscous or Coulomb damping material will then be added within the TMD system to provide the required value of damping. For the simple plywood TMD system described here, it would be difficult to provide known values of damping in the TMD. It must however be possible to achieve this using viscous damping material in-between layers of plywood, but this was not tried here. In these tests, using plywood sheets of different size and number altered the damping of the TMD system. In cases where two layers of plywood were used, friction between planks was assumed to increase damping in the absorber. The level of friction was altered by placing polythene or hard rubber between the sheets.

Design of planks

After estimation of the absorber weight, the chosen plank stiffness should ensure that the natural frequency of the absorber is equal to the troublesome floor frequency. By assuming the plywood as simply supported with the weights at mid-span, an estimate of mid-span deflection can be made using standard formulae. When related to natural frequency, (equation 2.6, page 23) gives:

$$\Delta_s = \left(\frac{15.76}{f_0}\right)^2 \tag{7.3}$$

where Δ_s is the mid-span deflection in mm. If the absorber mass is uniformly distributed, the relationship becomes:

$$\Delta_s = \left(\frac{17.75}{f_0}\right)^2 \tag{7.4}$$

Hence, having already obtained a value for f_0, coarse tuning of the absorber can be carried out by placing weights on the plywood, in order to achieve a deflection within the range of equations 7.3 and 7.4. During the experimental procedure, it was found that placing weights at mid-span of the plywood sheets gave better results if the weights were evenly spread by equal amounts across the width of the TMD.

Tuning of the TMD

Once coarse tuning of the TMD was accomplished, according to equations 7.3 and 7.4, fine tuning could be carried out by adjusting weights and checking the absorber frequency in one of two ways. The first is by observing the FRF of the slab when subjected to a sine-sweep. By comparing the FRFs at different weights, the best TMD mass can be obtained. The second method is to shake the slab at its natural frequency so that if the TMD is properly tuned, resonance vibrations may be observed. It would in fact be better to shake the TMD and look for resonance vibration of the slab, but the experimental apparatus at hand did not make this option a possibility.

7.3 Experimental results

An extensive experimental programme was carried out on the model post-tensioned concrete floor slab, in order to test the viability of the proposed TMD system. As explained in section 7.2, two different sizes of plywood were used with different configurations of single and double layered TMDs. Table 7.1 gives an outline of the different TMD arrangements, and the masses required at mid-span to tune them. The loading used was in the form of heel-drop and sine-sweep excitations.

The responses were taken on several points on the slab and TMD, at each configuration and loading condition. The given values represent averages of these points at each test.

Table 7.1: Masses needed for tuning of the plywood TMDs

TMD configuration	Mass of plywood (kg)	Mass at midspan (kg)	Generalised TMD mass (kg)	Mass ratio (generalised)	TMD centre deflection (mm)
[Test 1] one layer of wideply (1.2m×1m×10mm)	10	20	25	0.031	3
[Test 2] two layer wideply (nothing in-between)	19.5	bad tuning	-	-	-
[Test 3] two layer wideply (polythene in-between)	19.5	25	34.75	0.043	5
[Test 4] two layer wideply (rubber in-between)	19.5	23	32.75	0.040	5
[Test 5] one layer of narrowply (1.2m×0.3m×10mm)	3.7	10	11.85	0.015	3
[Test 6] two layer narrowply (nothing in-between)	7.4	20 (bad tuning)	23.7	0.029	3
[Test 7] two layer narrowply (polythene in-between)	7.4	20	23.7	0.029	3
[Test 8] two layer narrowply (rubber in-between)	7.4	15	18.7	0.023	3

Note that in cases where two layers of plywood were used with nothing in-between, the TMD could not be tuned satisfactorily. This maybe due to the high amount of friction that exists between these layers, which does not allow sufficient energy dissipation in the TMD. This is because the vibration forces on the TMD are smaller than the limiting friction force between the two layers. By putting polythene or rubber between the sheets, a reduction in friction force was achieved, which allowed energy dissipation. Here, the experimental results are discussed.

***Test 1* - One layer of Wideply:** Figure 7.2 shows FRF plots of the bare slab without TMD, and the application of a TMD in the form of wideply. These plots were obtained from sine-sweep loading tests on the slab, as explained in section 4.5. It can be seen from figures 7.2(a) and 7.2(b) that the transfer function magnitude decreases by nearly 70% as a result of the TMD addition. Figure 7.2(c) shows that the response of the TMD itself is seven times greater than that of the slab. Figure 7.2(d) illustrates the slab response with an out-of-tune TMD. A 10% change in TMD mass leads to approximately 20% rise in response.

The responses of the slab and TMD to heel-drop loading are shown in figure 7.3. It can be seen from figure 7.3(a) that the inclusion of the TMD noticeably increases the damping capacity of the slab. In comparing the responses of the TMD and the slab, figure 7.3(b), note that the vibration amplitude of the TMD is around six times that of the floor.

***Test 2* - Two layers of wideply (nothing in-between):** As mentioned in table 7.1, it was not possible to arrive at a satisfactorily tuned TMD for this case. It was observed, however, that with higher weights the amplitude of response was greatly reduced.

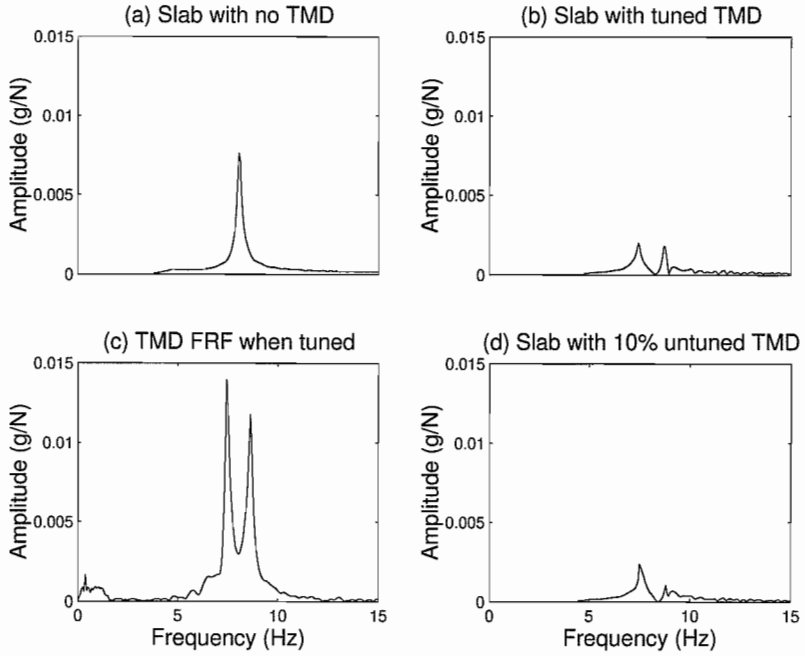

Figure 7.2: FRF plots of TMD as one layer of wideply (Test 1)

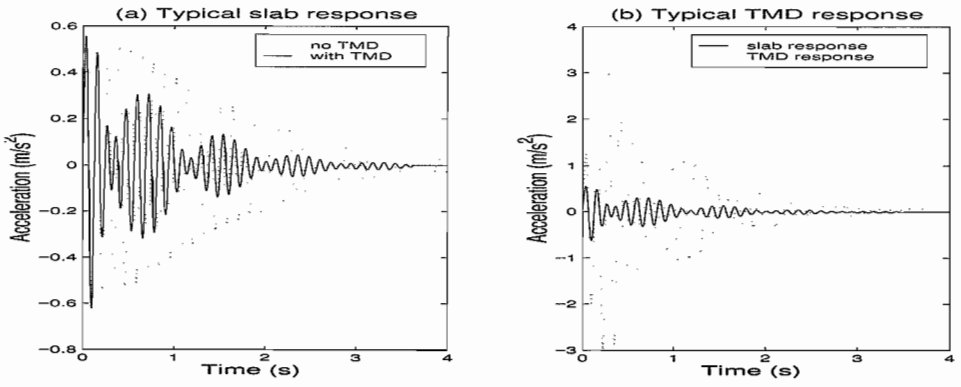

Figure 7.3: Heeldrop responses with one layer wideply TMD (Test 1)

***Test 3* - Two layers of wideply (polythene in-between):** FRF plots of this case are shown in figure 7.4. Figure 7.4(c) shows that more damping is taking place within the TMD system leading to a faster decay of slab response, as also observed from the heel-drop plots of figure 7.5. In assessing the sensitivity to accurate tuning, figure 7.4(d), it is seen that a 20% change in TMD mass leads to approximately 25% increase in slab response.

***Test 4* - Two layers of wideply (hard rubber in-between):** In this case, the slab response was seen to decrease six fold at the fundamental frequency, and the damping decay of the slab increased in the same way as with the polythene. The TMD response was around four times as much as that of the slab.

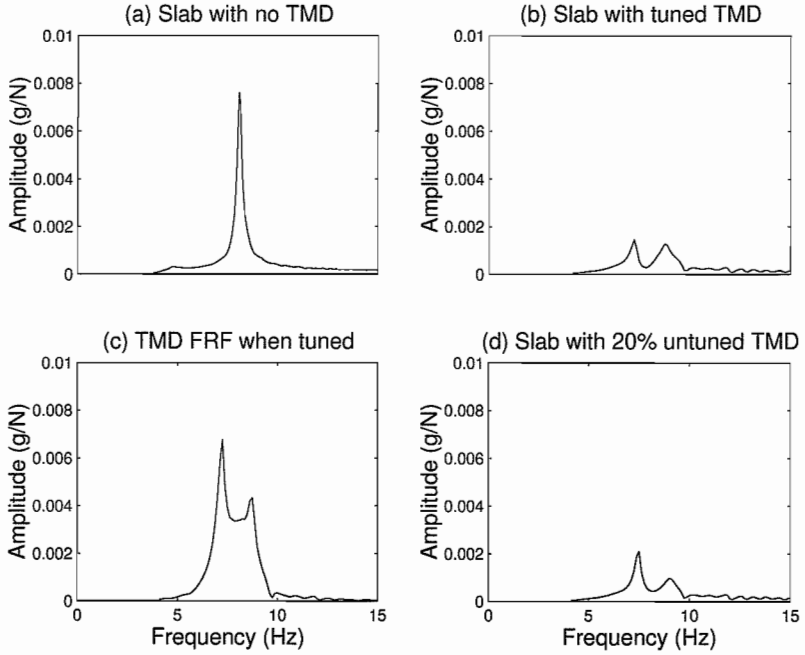

Figure 7.4: FRF plots of TMD as two layers of wideply with "polythene" in-between (Test 3)

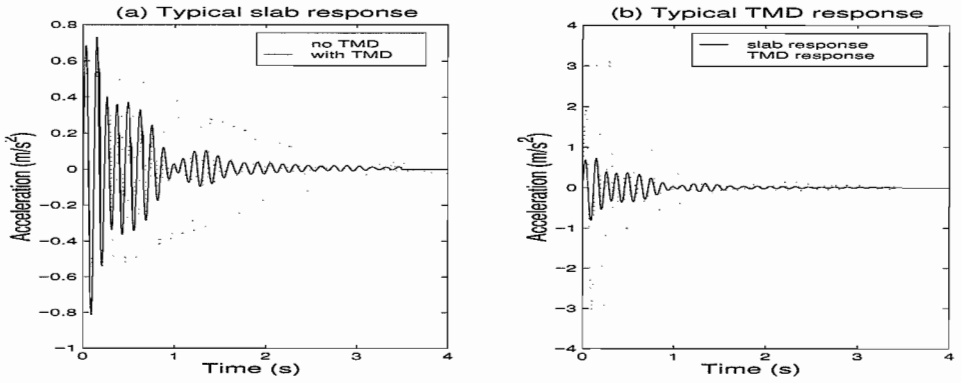

Figure 7.5: Heeldrop responses with two layers of wideply (polythene in-between) TMD (Test 3)

***Test 5* - One layer of Narrowply:** With shortening the width of the plywood, the value of mass ratio is reduced, since less weight is needed for TMD tuning. Figure 7.6 shows that the slab response is reduced as before, but that the TMD response is much higher than with wideply. The sensitivity analysis of figure 7.6(d) shows that a 10% change in tuning weight leads to a 20% increase in slab response. Heel-drop plots of figure 7.7 also show a high TMD response and relatively low damping.

***Test 6* - Two layers of narrowply (nothing in-between):** As with wideply, the TMD could not be satisfactorily tuned for this case. However, with 20kg of weight, it was possible to reduce the vibrations by around 70%.

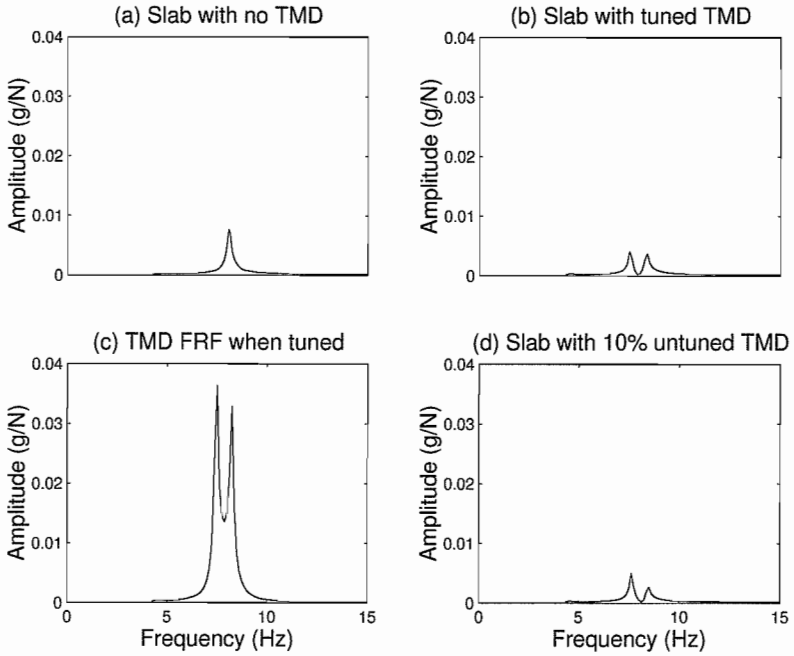

Figure 7.6: FRF plots of TMD as one layer of narrowply (Test 5)

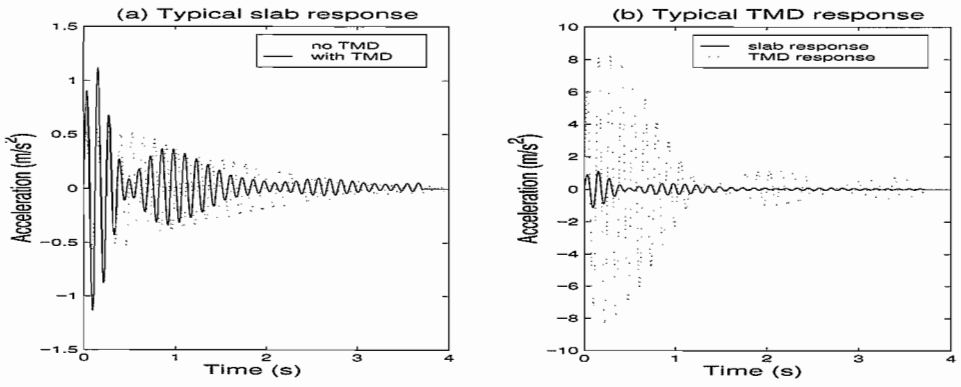

Figure 7.7: Heeldrop responses with one layer of narrowply TMD (Test 5)

***Test 7* - Two layers of narrowply (polythene in-between):** The results for this case are shown in figures 7.8 and 7.9, where the tuning of the TMD was more satisfactory. This is illustrated by the sensitivity analysis of figure 7.8(d). Also, the width of the tuned peak is very broad suggesting that the polythene has aided slippage between the plywood layers, increasing energy dissipation. This leads to an increase in damping at the TMD, as shown in figure 7.9(b).

***Test 8* - Two layers of narrowply (hard rubber in-between):** Less weight was required to tune the TMD for this case, as shown in table 7.1. Comparisons with other cases are made in the following section.

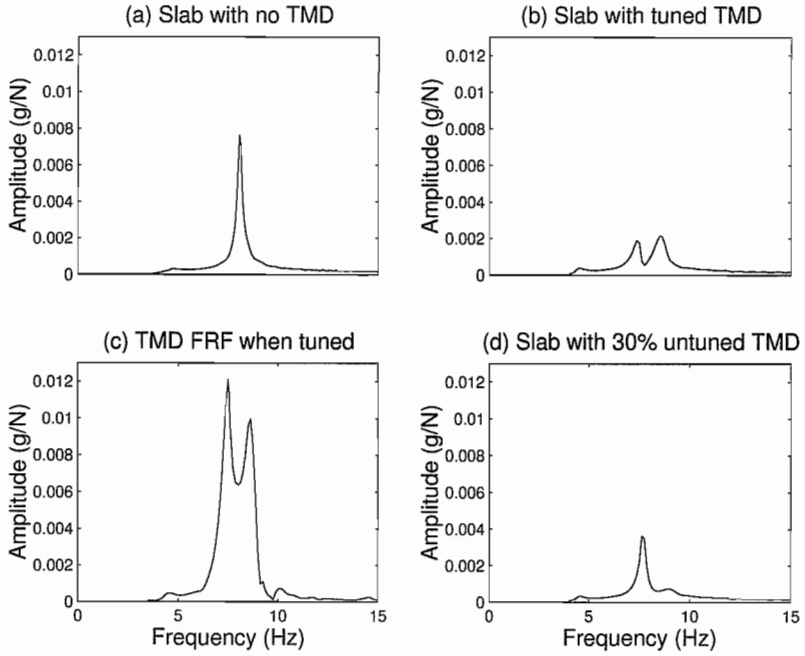

Figure 7.8: FRF plots of TMD as two layers of narrowply with "polythene" in-between (Test 7)

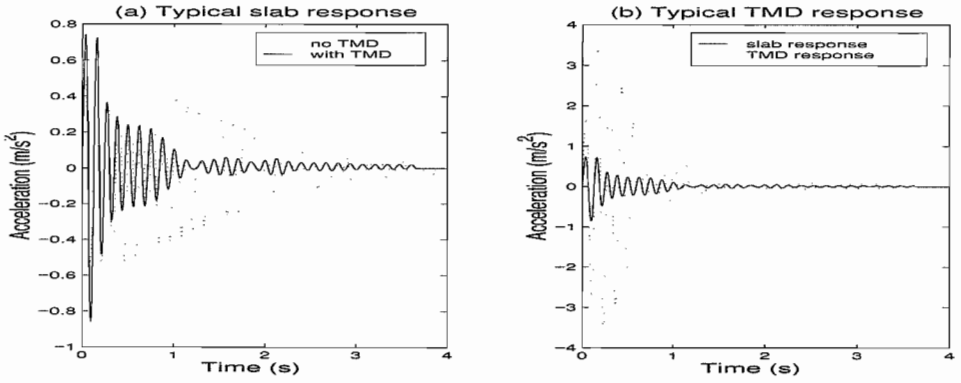

Figure 7.9: Heeldrop responses with two layers of narrowply (polythene in-between) TMD (Test 7)

7.3.1 Comparisons of TMD configurations

***Case A* - One or two layers?** Figure 7.10(a) shows a heel-drop plot of slab response when it has one layer of TMD superimposed on a graph of a two layer configuration with polythene in-between. It is deduced that for both wideply and narrowply, the slab response decays faster with a two layer TMD. This is evident since a two-layered TMD has been shown to have higher inherent damping, as seen in figure 7.10(b).

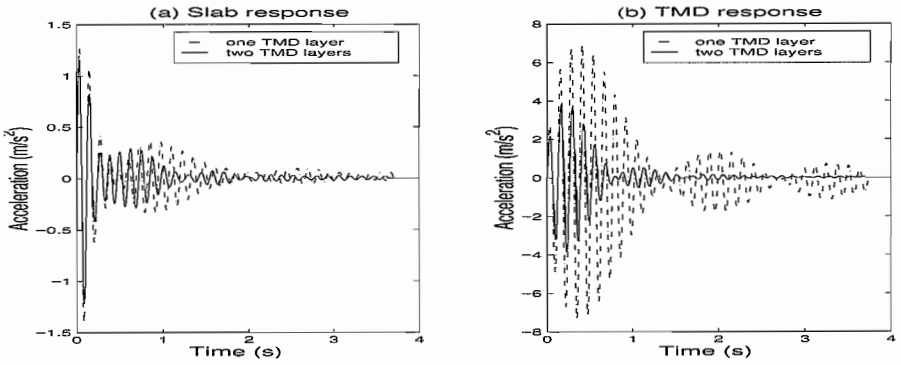

Figure 7.10: Comparison of one and two layer TMD configurations on response to heeldrop (Case A)

***Case B* - Wideply or Narrowply?** Wideply and narrowply TMDs are compared in figure 7.11, where for the slab response with wideply there is smaller initial peak and faster decay of vibrations. The difference in response of the plywood in each case is very significant. Figure 7.11(b) shows that the amplitude of vibration for the wideply case is more than half of that for the lighter TMD, and the transfer period of energy is also much shorter. This energy transfer is dependent on the mass ratio, where with a lower μ, it takes longer for the transfer to occur.

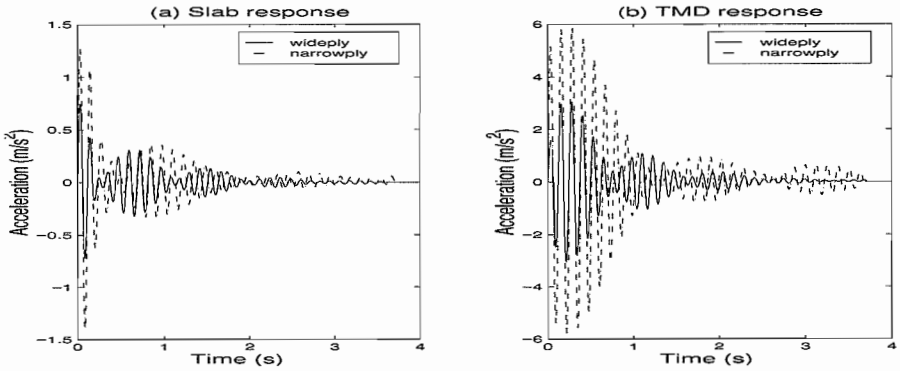

Figure 7.11: Comparison of wideply and narrowply TMD configurations on response to heeldrop (Case B)

***Case C* - Nothing or polythene between two layers of ply?** This comparison is made in figure 7.12. It can be seen that with polythene, the decay is marginally increased. This is attributed to more movement at the contact surface, causing more energy dissipation. The polythene in effect aids the damping of the two-layered TMD.

***Case D* - Nothing or rubber between two layers of ply?** With rubber in-between, figure 7.13(a) shows a marginally faster decay of vibrations on the slab level. On the TMD response of figure 7.13(b), there is no significant difference.

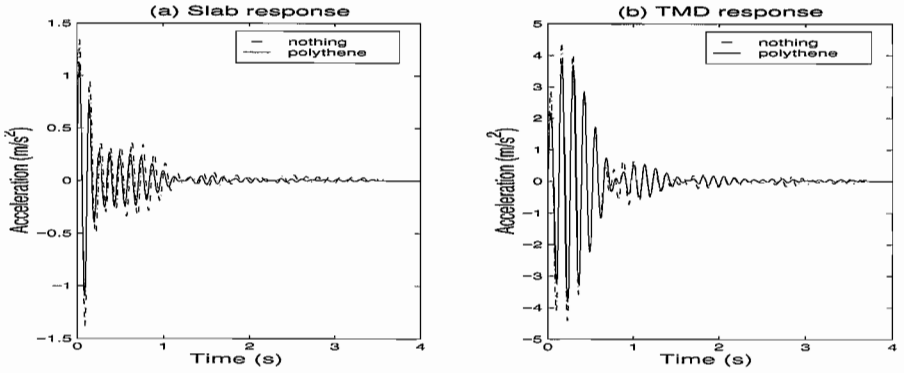

Figure 7.12: Comparison of having "nothing" or "polythene" between two layers of TMD (Case C)

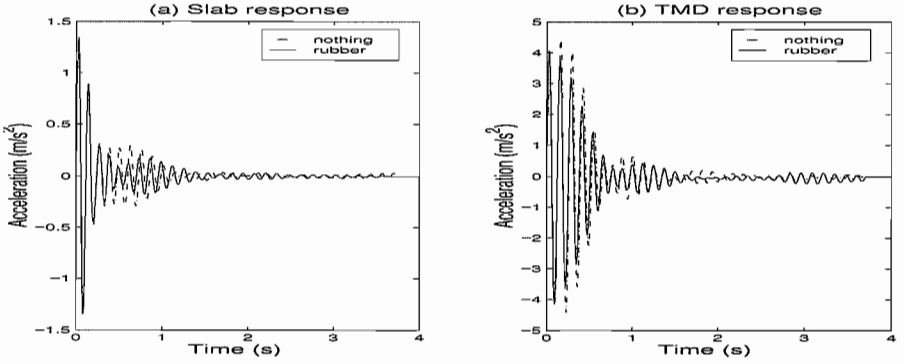

Figure 7.13: Comparison of "nothing" or "hard rubber" between layers (Case D)

***Case E* - Polythene or rubber between two layers of ply?** Figure 7.14 shows the slab and TMD response due to these two conditions. No significant difference is observed and any small changes may be due to the difference in masses needed to tune the TMD, see table 7.1.

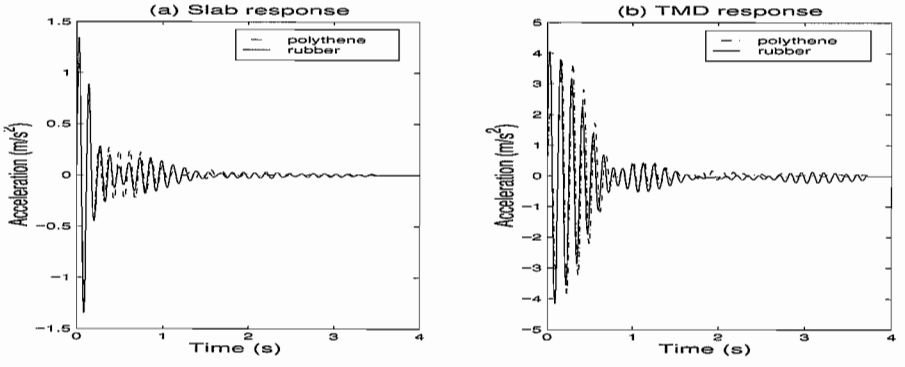

Figure 7.14: Comparison of "polythene" or "hard rubber" between layers (Case E)

Summary of experimental results

- two layers of ply give faster decay
- wideply shows faster decay of slab vibrations as opposed to narrowply
- narrowply has twice the response at TMD level compared to wideply
- with polythene between, slab decay is marginally faster than with nothing in-between
- with rubber in-between, as opposed to nothing, marginally faster rate of decay is observed at both slab and TMD
- polythene and rubber have similar effect on decay of slab and TMD

7.4 Structure-TMD models

Here, two theoretical models are presented in order to simulate the behaviour of the slab and the TMD. These are in the form of a closed form solution of a 2DOF damped lumped mass system, and a numerical time-stepping analysis of the same problem. Diagrammatic representation of the structure-TMD system, used in the models, is shown in figure 7.15. Comparisons are made with the experimental results to validate each model. The time-stepping model is seen to best represent the experimental results. Hence, it is updated to other slab configurations and used to propose a design guideline for the plywood TMD system.

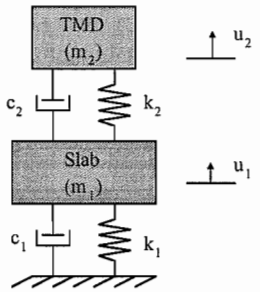

Figure 7.15: 2DOF lumped mass-spring-damper model of slab-TMD system

7.4.1 Closed-form solution

The free vibration equation of motion of the system in figure 7.15 is given in matrix form by: [Timoshenko et al. (1974)]

$$\begin{bmatrix} m_1 & 0 \\ 0 & m_2 \end{bmatrix} \begin{bmatrix} \ddot{u}_1 \\ \ddot{u}_2 \end{bmatrix} + \begin{bmatrix} c_1 + c_2 & -c_2 \\ -c_2 & c_2 \end{bmatrix} \begin{bmatrix} \dot{u}_1 \\ \dot{u}_2 \end{bmatrix} + \begin{bmatrix} k_1 + k_2 & -k_2 \\ -k_2 & k_2 \end{bmatrix} \begin{bmatrix} u_1 \\ u_2 \end{bmatrix} = \begin{bmatrix} 0 \\ 0 \end{bmatrix} \tag{7.5}$$

where subscripts 1 and 2 represent the slab and TMD respectively. Now assume solutions of the general form:

$$u_1 = X_1 e^{st} \qquad \text{and} \qquad u_2 = X_2 e^{st} \tag{7.6}$$

where s is the complex frequency. Substitution of equations 7.6 and their derivatives into equation 7.5, results in the following eigenvalue problem:

$$\begin{bmatrix} m_1 s^2 + (c_1 + c_2)s + (k_1 + k_2) & -c_2 s - k_2 \\ -c_2 s - k_2 & m_2 s^2 + c_2 s + k_2 \end{bmatrix} \begin{bmatrix} X_1 \\ X_2 \end{bmatrix} = \begin{bmatrix} 0 \\ 0 \end{bmatrix} \tag{7.7}$$

For a non-trivial solution, the determinant of the matrix in equation 7.7 must be zero, leading to a fourth degree polynomial:

$$\begin{aligned} m_1 m_2 s^4 + [m_1 c_2 + m_2 (c_1 + c_2)]\, s^3 + [m_1 k_2 + c_1 c_2 + m_2 (k_1 + k_2)]\, s^2 \\ + (c_1 k_2 + c_2 k_1)\, s + k_1 k_2 = 0 \end{aligned} \tag{7.8}$$

For the system to vibrate freely, damping must be small and all nonzero roots of equation 7.8 will be complex. They occur in conjugate pairs that may be expressed as:

$$s_{11}, s_{12} = -\zeta_1 \omega_1 \pm i\omega_1 \qquad \text{and} \qquad s_{21}, s_{22} = -\zeta_2 \omega_2 \pm i\omega_2 \tag{7.9}$$

By substituting the roots of equation 7.9 into equation 7.7, the corresponding amplitude ratios can be obtained:

$$r_{ij} = \frac{c_2 s_{ij} + k_2}{m_1 s_{ij}^2 + (c_1 + c_2) s_{ij} + (k_1 + k_2)} = \frac{m_2 s_{ij}^2 + c_2 s_{ij} + k_2}{c_2 s_{ij} + k_2} \tag{7.10}$$

where i=1 or 2 and j=1 or 2. The resulting ratios r_{11}, r_{12} and r_{21}, r_{22} are complex conjugate pairs. The complete solution can then be written as:

$$\begin{aligned} u_1 &= r_{11} X_{11} e^{s_{11} t} + r_{12} X_{12} e^{s_{12} t} + r_{21} X_{21} e^{s_{21} t} + r_{22} X_{22} e^{s_{22} t} \\ u_2 &= X_{11} e^{s_{11} t} + X_{12} e^{s_{12} t} + X_{21} e^{s_{21} t} + X_{22} e^{s_{22} t} \end{aligned} \tag{7.11}$$

in which the coefficients X_{11}, X_{12} and X_{21}, X_{22} are complex conjugate pairs determined from initial conditions. The first two terms of u_2 in equation 7.11 can be converted into equivalent trignometric expressions by writing:

$$X_{11} e^{s_{11} t} + X_{12} e^{s_{12} t} = e^{-\zeta_1 \omega_1 t} (C_1 \cos \omega_1 t + C_2 \sin \omega_1 t) \tag{7.12}$$

where $C_1 = X_{11} + X_{12}$ and $C_2 = i(X_{11} - X_{12})$ are real constants. Similarly for u_1, the amplitude ratios can be expressed in terms of their real and imaginary parts:

$$r_{11} = a + ib \quad , \quad r_{12} = a - ib \quad , \quad r_{21} = c + id \quad , \quad r_{22} = c - id \tag{7.13}$$

giving the first two terms of u_1 as:

$$r_{11}X_{11}e^{s_{11}t} + r_{12}X_{12}e^{s_{12}t} = e^{-\zeta_1\omega_1 t}\left[(C_1a - C_2b)\cos\omega_1 t + (C_1b + C_2a)\sin\omega_1 t\right] \tag{7.14}$$

This conversion process can be repeated throughout equation 7.11 giving the total solution to the problem as:

$$\begin{aligned} u_1 &= e^{-\zeta_1\omega_1 t}\left[(C_1a - C_2b)\cos\omega_1 t + (C_1b + C_2a)\sin\omega_1 t\right] \\ &\quad + e^{-\zeta_2\omega_2 t}\left[(C_3c - C_4d)\cos\omega_2 t + (C_3d + C_4c)\sin\omega_2 t\right] \\ u_2 &= e^{-\zeta_1\omega_1 t}\left[C_1\cos\omega_1 t + C_2\sin\omega_1 t\right] + e^{-\zeta_2\omega_2 t}\left[C_3\cos\omega_2 t + C_4\sin\omega_2 t\right] \end{aligned} \tag{7.15}$$

where $C_1 \rightarrow C_4$ are determined from initial conditions. For the case of a floor subjected to footsteps, a heel-drop excitation is a suitable representation of loading. Here, the heeldrop is applied as an initial velocity, V, on the model slab. Hence, the initial conditions to equation 7.15 are:

$$u_1 = u_2 = \dot{u}_2 = 0 \qquad \text{and} \qquad \dot{u}_1 = V \qquad \text{at} \quad t = 0 \tag{7.16}$$

With application of these conditions, the solutions for $C_1 \rightarrow C_4$ can be obtained:

$$\begin{aligned} C_1 &= \tfrac{C_2b + C_4d}{a - c} & C_2 &= \frac{-\alpha_4 C_4}{\alpha_3} \\ C_3 &= -C_1 & C_4 &= \frac{\alpha_3 V}{\alpha_3\alpha_2 - \alpha_1\alpha_4} \end{aligned} \tag{7.17}$$

where $\alpha_1 \rightarrow \alpha_4$ are constants depending on the natural frequencies and damping ratios:

$$\begin{aligned} \alpha_1 &= \frac{\omega_1 b^2 - \zeta_1\omega_1 ab - \omega_2 bd + \zeta_2\omega_2 bc}{a - c} + \omega_1 a + \zeta_1\omega_1 b \\ \alpha_2 &= \frac{\omega_1 bd - \zeta_1\omega_1 ad - \omega_2 d^2 + \zeta_2\omega_2 cd}{a - c} + \omega_2 c + \zeta_2\omega_2 d \\ \alpha_3 &= \frac{b\left(\zeta_2\omega_2 - \zeta_1\omega_1\right)}{a - c} + \omega_1 \\ \alpha_4 &= \frac{d\left(\zeta_2\omega_2 - \zeta_1\omega_1\right)}{a - c} + \omega_2 \end{aligned} \tag{7.18}$$

A MATLAB programme was written to evaluate this solution. Figure 7.16 shows plots of this model using experimental values of m_1, k_1, m_2, k_2 and ζ_1 with different values of ζ_2 and a fixed value of V. Notice that with increased TMD damping, the slab response decays faster until a limit of optimum TMD damping is reached. This is the limit of useability of this model, since the model is only valid for low damping values and the response ceases to be vibratory with high damping.

7.4.2 Numerical model

Having shown that cases of high TMD damping cannot be clearly defined by a closed form solution, a numerical time-stepping method was hence implemented. The model is still a damped 2DOF

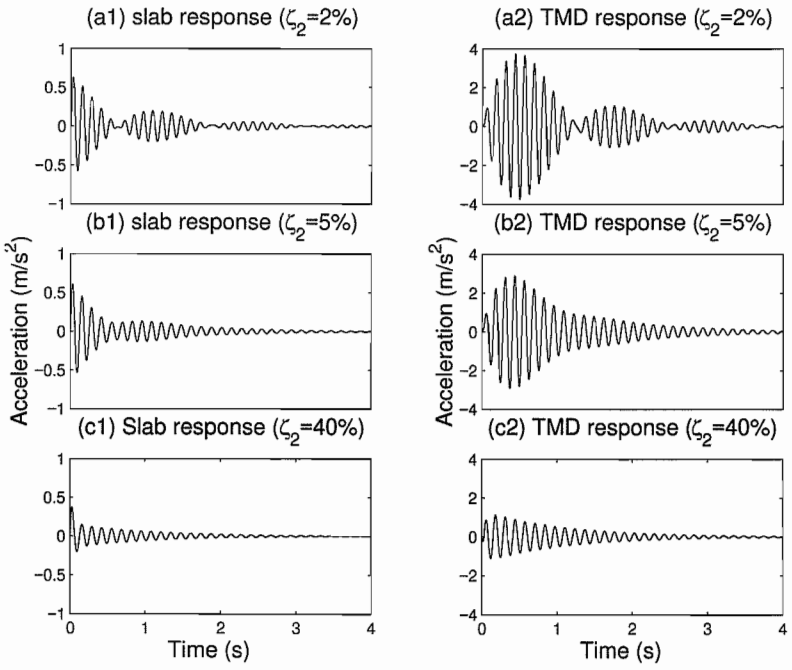

Figure 7.16: Analytical model plots of slab and TMD responses with different values of TMD damping (ζ_2)

lumped mass system of figure 7.15 but this time the equations of motion are solved using the *linear acceleration method* [Clough and Penzien (1993)]. The equations of motion can be written in incremental form as:

$$\begin{bmatrix} m_1 & 0 \\ 0 & m_2 \end{bmatrix} \begin{bmatrix} \Delta\ddot{u}_1 \\ \Delta\ddot{u}_2 \end{bmatrix} + \begin{bmatrix} c_1 + c_2 & -c_2 \\ -c_2 & c_2 \end{bmatrix} \begin{bmatrix} \Delta\dot{u}_1 \\ \Delta\dot{u}_2 \end{bmatrix} + \begin{bmatrix} k_1 + k_2 & -k_2 \\ -k_2 & k_2 \end{bmatrix} \begin{bmatrix} \Delta u_1 \\ \Delta u_2 \end{bmatrix} = \begin{bmatrix} 0 \\ 0 \end{bmatrix} \tag{7.19}$$

where i = 1,2 to denote slab or TMD. The method assumes acceleration to vary linearly over a time-step, giving the resultant velocity and displacement expressions shown in figure 7.17. By rearranging these and substituting into equation 7.19, the response of the system is written as:

$$\begin{bmatrix} \frac{6m_1}{\Delta t^2} + \frac{3(c_1+c_2)}{\Delta t} + (k_1 + k_2) & -\frac{3c_2}{\Delta t} - k_2 \\ -\frac{3c_2}{\Delta t} - k_2 & \frac{6m_2}{\Delta t^2} + \frac{3c_2}{\Delta t} + k_2 \end{bmatrix} \begin{bmatrix} \Delta u_1 \\ \Delta u_2 \end{bmatrix} =$$
$$\begin{bmatrix} m_1\left(\frac{6\dot{u}_1}{\Delta t} + 3\ddot{u}_1\right) + c_1\left(3\dot{u}_1 + \frac{\ddot{u}_1\Delta t}{2}\right) + c_2\left(3\dot{u}_1 + \frac{\ddot{u}_1\Delta t}{2} - 3\dot{u}_2 - \frac{\ddot{u}_2\Delta t}{2}\right) \\ m_2\left(\frac{6\dot{u}_2}{\Delta t} + 3\ddot{u}_2\right) + c_2\left(-3\dot{u}_1 - \frac{\ddot{u}_1\Delta t}{2} + 3\dot{u}_2\frac{\ddot{u}_2\Delta t}{2}\right) \end{bmatrix} \tag{7.20}$$

Equation 7.20 can be solved in stepwise form using the initial conditions given earlier in equation 7.16. A MATLAB programme was written to carry out the solution using a time-step of two milliseconds. Figure 7.18 shows plots of this model for an arbitrary value of V, and different values of ζ_2. In this case, it is observed that with high TMD damping, the model is still valid (see figure 7.18(c1)). Figure 7.19 illustrates a comparison between the numerical model and the analytical one for same values of all variables. It can clearly be seen that at low values of ζ_2, both models give very similar responses (see figure 7.19(a)). With higher values of ζ_2, the predictions of response become different.

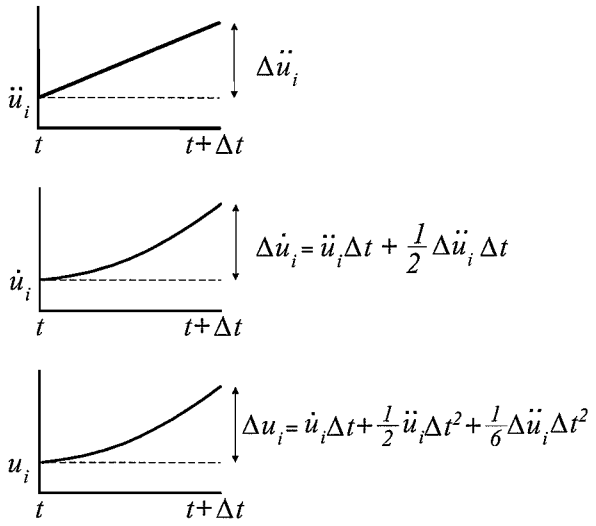

Figure 7.17: Expressions used in the *linear acceleration method*

Typical comparisons of the numerical model with the experimental results are shown in figure 7.20, where a satisfactory agreement is observed, even at high values of μ and ζ_2. This solution method was adopted for the remainder of the analysis to obtain generalised values of V and ζ_2.

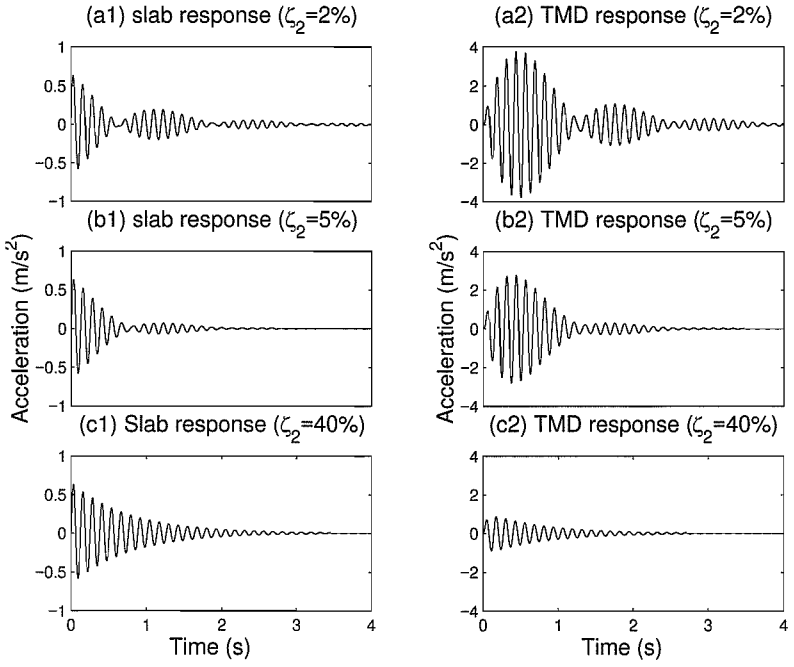

Figure 7.18: Numerical model plots of slab and TMD responses with different values of TMD damping (ζ_2)

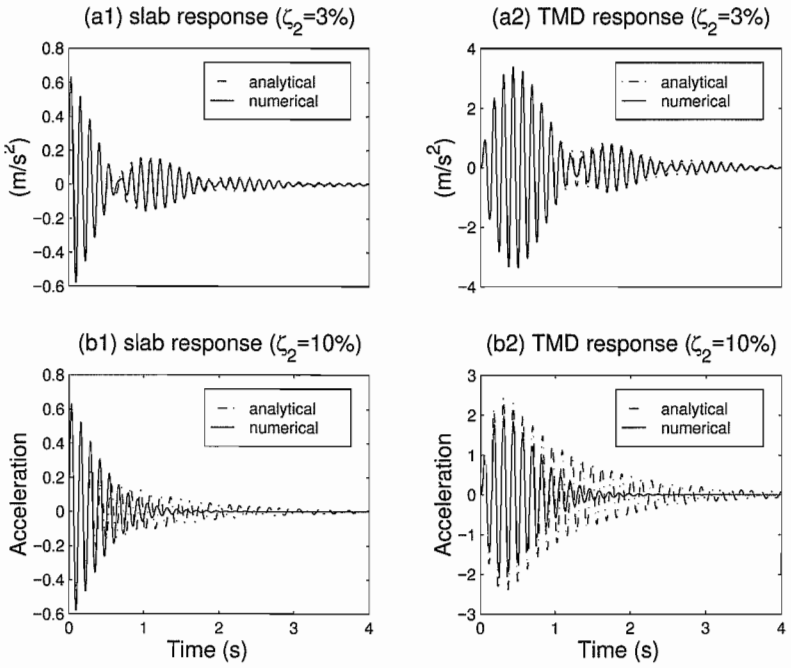

Figure 7.19: Comparisons between analytical and numerical models

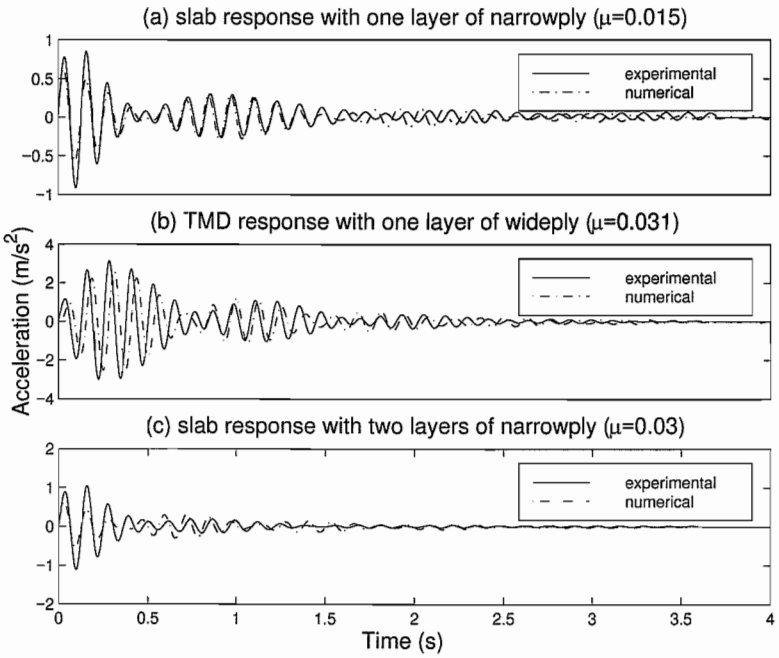

Figure 7.20: Comparisons between experimental and numerical model results

Derivation of Initial Velocity

To update V in the model, a plot of the model was superimposed on top of an experimental plot and the value of V was iterated until its initial peak best fitted the particular experimental case. A MATLAB programme was written to derive the best value of initial model response amplitude at each test. The range of the derived values for V was different due to variations in heeldrop impacts. In this way, an average value could be derived from many experimental plots to represent a typical initial velocity due to heeldrop. This is discussed in section 7.4.3.

Derivation of TMD damping

Here, once the best model initial velocity was derived, an extensive MATLAB programme was written, which would iterate through a range of values for ζ_2 and by comparing with the experimental data, would suggest the best numerical value to fit the data. The programme first assumed an arbitrary value for ζ_2 and plotted the resultant numerical graph on top of the equivalent experimental one. By correlating the peaks of the two graphs, ζ_2 was incremented within a given range and a value was obtained, which best fitted the particular experimental case. This procedure was carried out for every TMD configuration at every point tested, giving a large number of values for ζ_2, which could be averaged to obtain a general figure.

7.4.3 Generalisation of the model

Table 7.2 summarises the averages of the derived values for ζ_2 and V, which best fit the experimental data at each TMD configuration. It also includes approximate reductions in experimental slab vibrations. With all other parameters in the system remaining constant, the two variables of TMD damping and mass ratio are the only factors which can affect the performance of the plywood TMD.

In the following sections, a typical value for the initial velocity, V, is first deduced and used in a generalisation study of the two key parameters of mass ratio and TMD damping. The model is applied to different slab configurations and best starting values of ζ_2 and μ are derived, which could be assumed to be effective for any slab. In carrying out these optimisations, suggested acceleration amplitude limits, given by Allen (1990a) and Bachmann (1992b), are used. For ease of presentation, the responses are plotted for the rest of this section as peak responses only, see figure 7.21.

Table 7.2: Summary of derived model values

TMD configuration	Average ζ_2	Average V m/s	Mass ratio (μ)	Approx. experiment vibration reduction
one layer wideply	0.023	0.013	0.031	70%
two layer wideply (polythene in-between)	0.034	0.013	0.043	80%
two layer wideply (rubber in-between)	0.034	0.013	0.040	80%
one layer narrowply	0.014	0.020	0.015	50%
two layer narrowply (nothing in-between)	0.021	0.011	0.029	75%
two layer narrowply (polythene in-between)	0.020	0.011	0.029	70%
two layer narrowply (rubber in-between)	0.020	0.009	0.023	70%

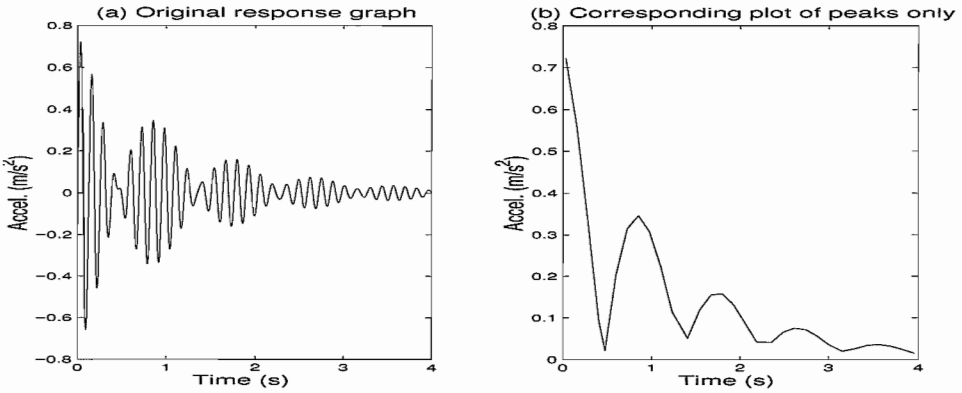

Figure 7.21: Representation of responses as their peaks

Choice of initial velocity

From table 7.2, it can be seen that the range of values for V is fairly close. This indicates that when averaging many cases of heeldrop loading, a good estimate of the heel-impact can be derived, particularly if the heeldrop is performed by the same person. Hence it is possible to consider a fixed value of V for all the TMD configurations, and simplify the model accordingly to a typical heeldrop impulse. The value recommended for these tests is taken as 0.015m/s. Note that from table 7.2, this value is a conservative one leading to an initial acceleration amplitude of $0.7\text{m/s}^2(\approx 7\%g)$, see figure 7.21. Since heeldrop is already regarded as a severe loading, the resultant model accelerations are assumed to be higher than would occur normally.

Generalisation of mass ratio

Table 7.2 clearly shows that the mass of the TMD directly dictates the amount of reduction in the slab vibration response. The higher the TMD mass, the greater the reduction in slab response. However, it is not always possible to use a large or heavy TMD, as constraints may exist in the placement of the plywood. In addition, the size of the planks and the tuning weights may also

dictate the size of the TMD system for a particular floor. Hence in any design, account must be taken of a possible range of mass ratios, which can be used for a particular slab.

Figure 7.22 shows an idealised model slab response without a TMD system, subjected to a typical heel impact. Note that the acceleration amplitude is slightly above acceptable limits of 0.5-1m/s^2(5-10%g) for active occupancies, and well above the limits for offices (see table 2.3, page 15). In the following discussion, a single limit of acceptance of 4%g is used to account for an average structure.

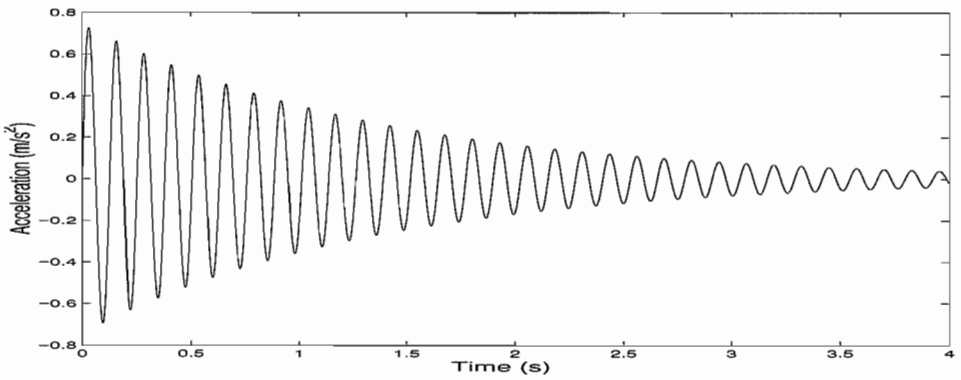

Figure 7.22: Single heeldrop on model slab without TMD

Taking a typical value for TMD damping ratio of 3% critical, figure 7.23 shows the model slab response with TMD systems of varying mass ratios. It is evident that the initial peak amplitude is unaffected by the addition of the TMD system. However, response is seen to decrease noticeably with higher mass ratios, until an optimum value is reached. Here, the optimum μ for the model slab is taken as 0.04, since at higher values a significant vibration reduction is not observed, and in some cases the secondary peaks may cause annoyance, as they can exceed 4%g. Hence, from figure 7.23 for a given TMD damping, any mass ratio within the range 0.01-0.04 can be very effective.

Other slab configurations

In order to support the values of mass ratio given above, two typical flat slab configurations, taken from field tests, were input into the model and their vibration behaviour after addition of TMDs was observed. These two slabs are described briefly below.

Slab 1 Taken from Caverson (1992), this is a loose representation of the Vantage West car park comprising a cast-in-place post-tensioned flat slab with unbonded tendons. A typical panel has dimensions of 8.4 × 7.2m with a slab thickness of 225mm. Slab damping ratio is 4.6% critical with fundamental frequency of 8.5Hz. Assuming the concrete properties to be similar to the model experiment, these values were input into the numerical model and found to be

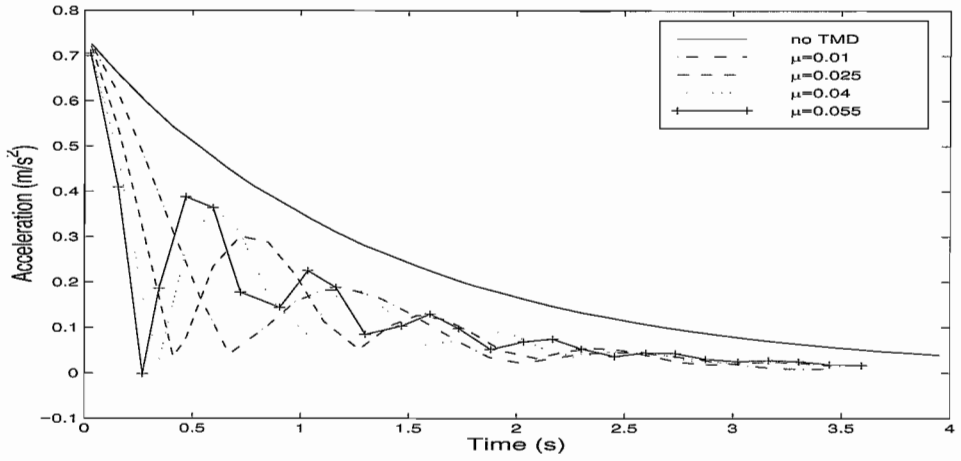

Figure 7.23: Model slab response with variations in mass ratio

acceptable and below 4%g. For the sake of this example, the slab was made more flexible and its damping reduced to 2% critical to make it more problematic. The model was then implemented with an arbitrary TMD damping of 3% critical, which is fairly conservative. Figure 7.24 shows the resultant responses without TMD and with TMD of varying mass ratios. In this case, a suitable range of μ, for fast reduction of vibration below 4%g, is between 0.01-0.025. The limit of amplitude taken here is conservative for a car park.

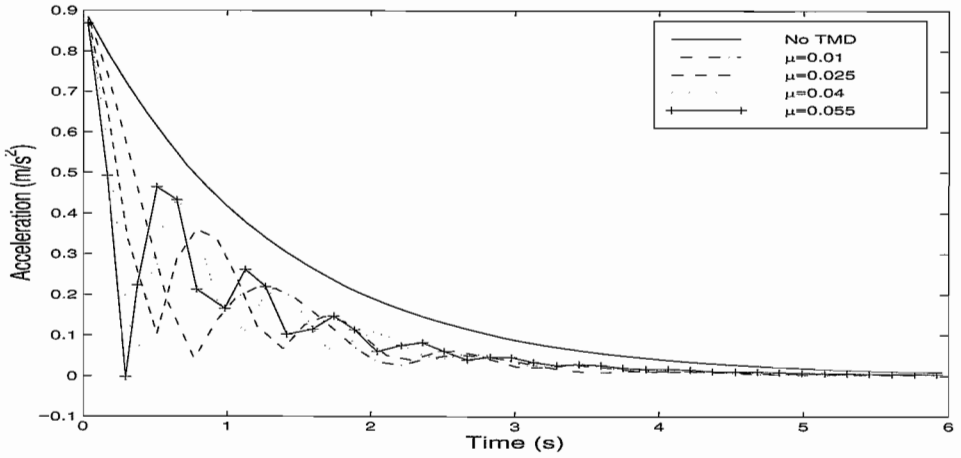

Figure 7.24: slab 1 (Vantage West) response with variations in mass ratio

Slab 2 Taken from Bachmann (1992a), this is a loose representation of a problematic gymnasium floor, supported on reinforced concrete beams. A typical panel has dimensions of 7×6m with a slab thickness of 250mm. Slab damping ratio is 2.4% critical with fundamental frequency of 7.5Hz. The responses at different mass ratios are shown in figure 7.25, using model slab concrete properties and a TMD damping of 2.5% critical. The range of mass ratios to reduce vibrations to acceptable levels is seen to be 0.01-0.04.

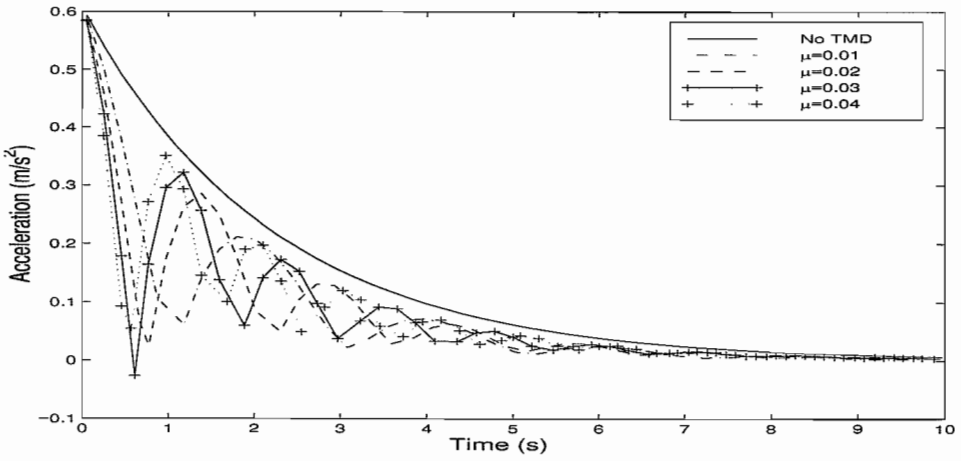

Figure 7.25: Slab 2 response with variations in mass ratio

Summary

Higher mass ratios for TMDs lead to quicker decay of vibration amplitudes. There exists an optimum ratio where any increase in μ does not greatly affect the response. A typical range of mass ratios for reducing vibrations to acceptable limits is 0.01-0.04, where a balance exists between having a lower μ with lighter TMD and a higher μ with heavier TMD but faster decay.

Generalisation of TMD damping

For the experimental slab, the response is plotted at an average mass ratio of 0.02 against varying values of ζ_2, figure 7.26. As expected, the higher the TMD damping, the faster the decay of slab vibrations. To reduce the vibration below $4\%g$ at the second peak, a TMD damping of 0.015 or above is required. Notice that this is the value of the slab damping ratio, so that for the TMD to be fully effective, it should have greater damping capacity than the slab. From table 7.2, it can be seen that all TMD configurations would satisfy this requirement, although with two layers of wideply having polythene or rubber in-between, the highest value of ζ_2 is achieved.

Other slab configurations

The range of TMD damping was observed against the two field slabs described above, using an average mass ratio of 0.02, and the following results were obtained.

Slab 1 Figure 7.27 shows variations of ζ_2 for the Vantage West slab. An acceptable TMD damping for reducing vibration below $4\%g$ is 3% critical or higher.

Slab 2 Figure 7.28 gives the variations of ζ_2 for the gymnasium floor with minimum acceptable value being 1.5% critical for vibration reduction below $4\%g$ at the second peak.

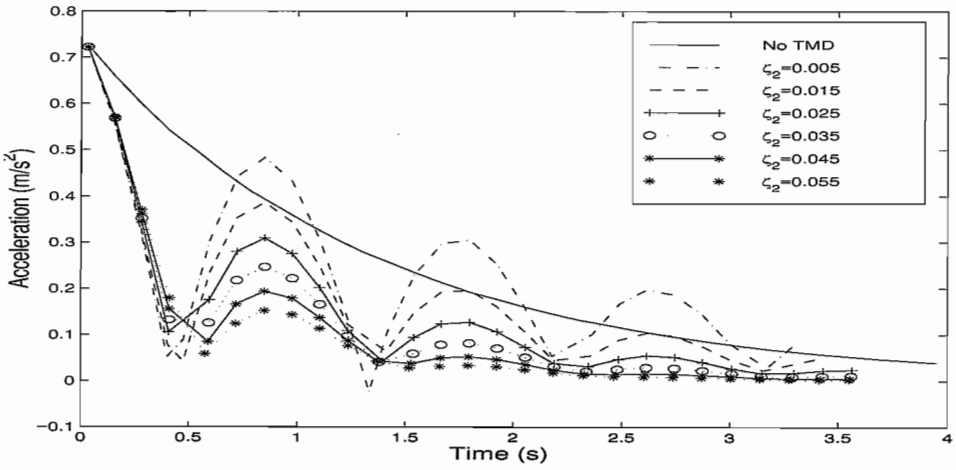

Figure 7.26: Model slab response with variations in TMD damping

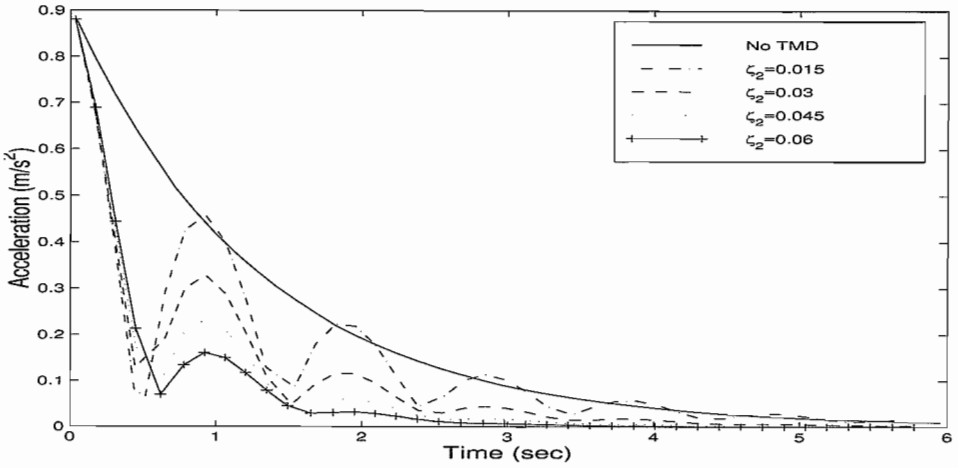

Figure 7.27: Vantage West slab response with variations in TMD damping

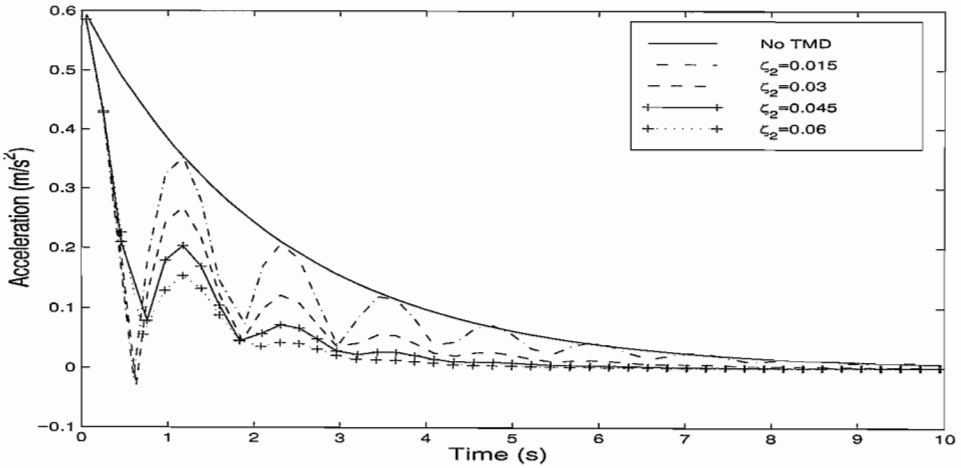

Figure 7.28: slab 2 response with variations in TMD damping

Summary

For a given mass ratio, the higher the TMD damping, the more effective the system and the faster the vibration decay. If ζ_2 becomes too large, the displacement of the TMD is inhibited, hence less energy can be dissipated. A minimum value for reducing vibrations due to a heel impact is around 2% critical for a typical slab. This value could be reduced with an increase in mass ratio if possible.

7.4.4 Extension of the model to walking vibrations

Until now, heeldrop loading was used as the impact on a typical slab giving a design criterion for a TMD system. This is acceptable as a heeldrop impact represents a very severe loading, so that the design for remedying the resulting vibrations can be considered as conservative. Here, consideration is given to intermittent vibrations, such as walking. Depending on the walking frequency, the loading is simulated as several heel impacts occurring after each other. This is shown in figure 7.29, where a comparison is made between simulating walking as successive heeldrops and an actual signal taken from Bachmann et al. (1995). It can be seen that limitations exist in representing walking in this way. Firstly, the impacts are very severe, particularly at higher harmonics, and in effect closer to rhythmic jumping, leading to greater slab response amplitude. Secondly, there is no horizontal walking momentum and in effect the person is considered as walking on spot. Hence, both these limitations make the model rather conservative and therefore it may be feasible to increase the acceptable acceleration limits for a given floor subjected to such loading. Here, these limits are increased from an average of $4\%g$ to $6\%g$.

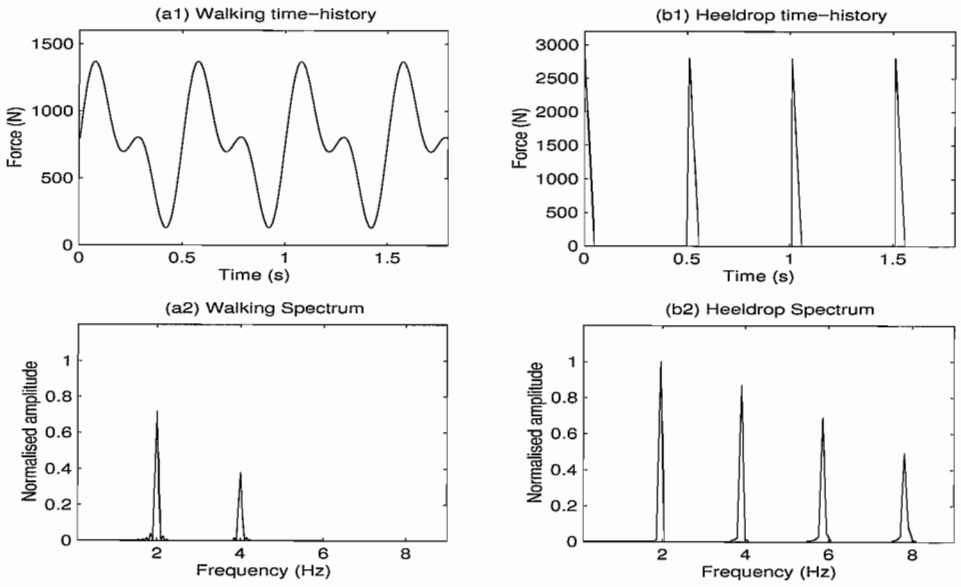

Figure 7.29: Simulated and actual walking time-histories and frequency spectra for walking at a frequency of 2Hz

Figure 7.30(a) shows the experimental model slab subjected to four simulated heeldrop footsteps at 2Hz. Similarly, figure 7.30(b) shows the model slab, with TMD, subjected to the same walking load. It can be seen that without the TMD, the responses to successive footsteps overlap, leading to a build-up of acceleration amplitudes up to around 20%g after four steps. In comparison, with a suitable TMD system designed for the floor, there is only one peak that may cause annoyance. By assuming an acceleration limit of 6%g, with a TMD the slab vibration becomes acceptable after 0.3 seconds, as compared with over 3 seconds without a TMD system.

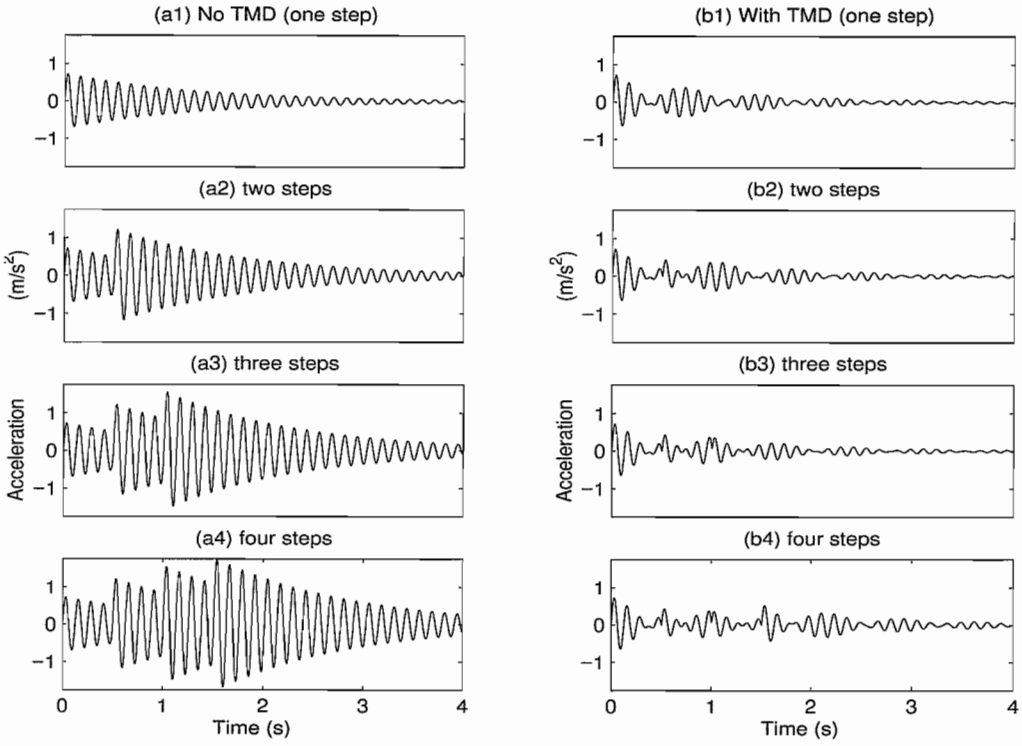

Figure 7.30: Walking simulations with and without TMD at 2Hz

Similar results are obtained with walking vibrations of different frequencies, as shown in figure 7.31, where only the peaks are plotted for clarity. Hence, it is seen that the proposed TMD system is very effective for walking vibrations as well as transient. Notice here that the TMD is more effective for certain walking frequencies than others. In the case of 3.6Hz footstep frequency, the vibration reduction is less significant. This is because 3.6Hz may not be a multiple of the slab fundamental frequency. However, this problem can be overcome by using multiple TMD systems, as explained in section 10.4. The effectiveness of the designed TMD system, in the model slab tests, is shown in figures 5.7 and 5.8 (pages 100-101) for horizontal and vertical walking respectively.

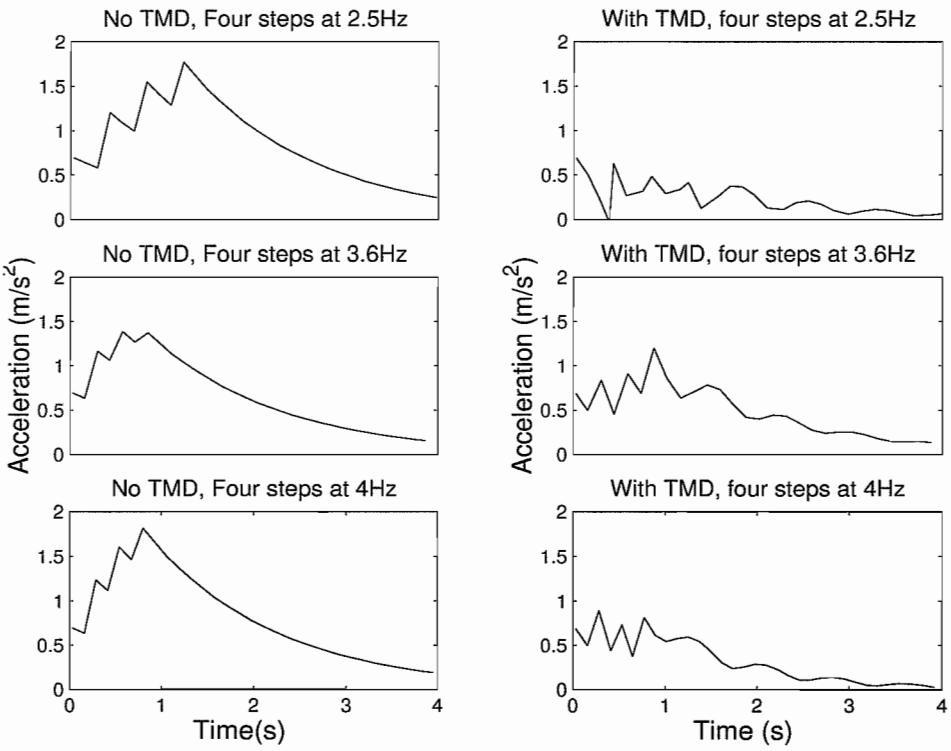

Figure 7.31: Walking simulations with and without TMD at other pacing frequencies

7.5 Sensitivity analyses

Having obtained a suitable model for a slab-TMD system, a sensitivity analysis was carried out to verify its ranges of usability. Here, the sensitivity to variations in each of the main variables was investigated separately, as follows:

Slab dimensions: Alterations to these parameters, particularly slab length, L, and depth, d, will affect the value of the model natural frequency. This is very significant as the tuning of the TMD is based on an accurate estimate of slab natural frequency. Figure 7.32 shows that with small changes in d, there is a significant change in slab frequency so that the model simulation becomes out of phase and the decay amplitudes are affected (N.B: as expected $f \propto d^2$). Similarly, figure 7.33 illustrates the importance of choosing the correct boundary conditions so that the model slab length is the distance undergoing displacement. This is particularly important in design, where one might want to estimate the *equivalent* simply supported span, taking into account effects of support stiffness and continuity. It would be advisable for the model to have values of slab dimensions within $\pm 10\%$ of real values.

Mass ratio (μ): Figure 7.34 shows how a change in mass ratio can affect the model simulation. It can be seen that the amplitude and decay rate of vibration are dependent on the mass

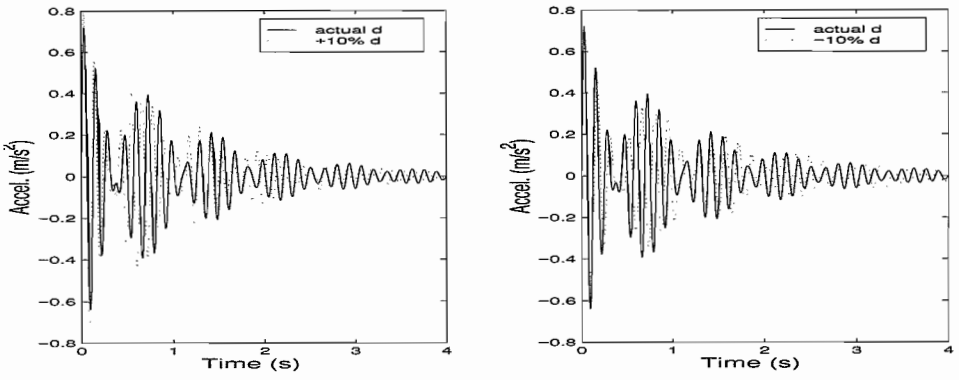

Figure 7.32: Sensitivity of model to variations in slab thickness

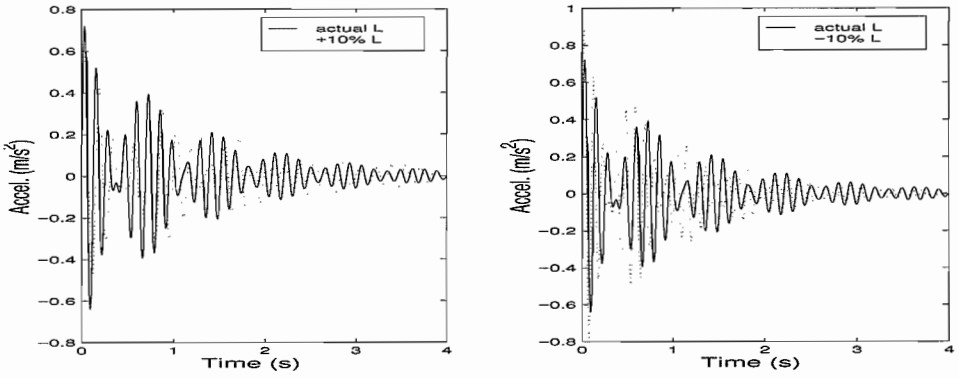

Figure 7.33: Sensitivity of model to variations in slab length

ratio. As explained in section 7.2.2, the larger the TMD mass, the faster the rate of decay.

TMD damping ratio (ζ_2): Average values of ζ_2 for each TMD stage are given in table 7.2. The sensitivity of the model to these values is illustrated in figure 7.35 for three values within a large range. Notice how this parameter affects amplitude of decay of the slab and must be included in any TMD design. It does not however affect slab natural frequency.

Summary

In addition to the above variables, sensitivity of the model to variations in Young's modulus, slab width, slab damping ratio, and initial applied velocity were also checked. In general, the proposed model can be acceptably used with given parameters within 10% of actual values, hence the model is not severely sensitive. It is however important to note that variations in the key parameters of mass ratio and TMD damping do not have any effect on the initial peak acceleration amplitudes of the slab. The TMD's effectiveness is only observed once the energy has been transferred from the primary to the secondary mass in the model.

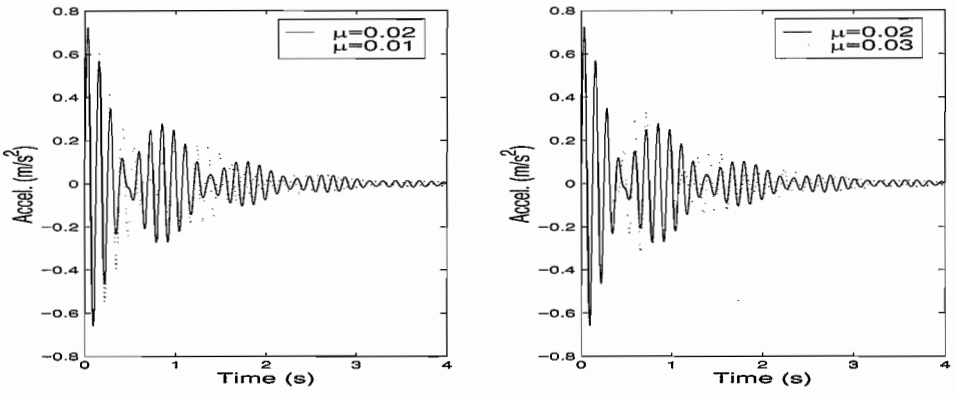

Figure 7.34: Sensitivity of model to variations in mass ratio

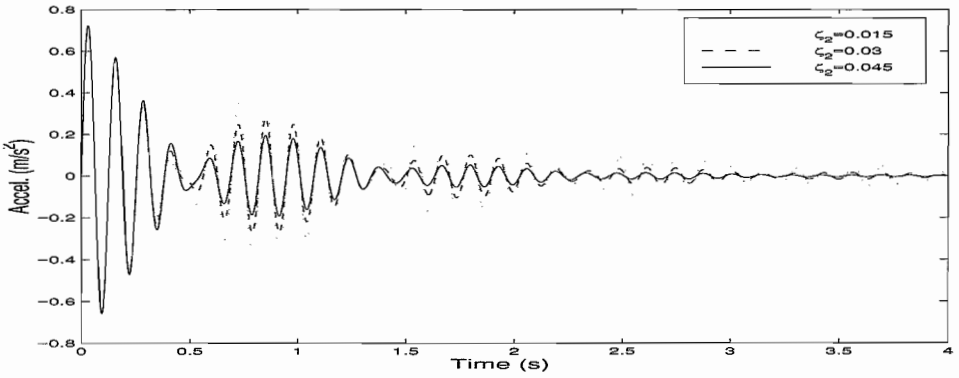

Figure 7.35: Sensitivity of model to variations in TMD damping ratio

7.6 Application of the model

Here, a design guideline is proposed which could be applied to a given slab. The guideline in its present form is at its early stages and perhaps somewhat too complex for use by designers. However, it is envisaged that with more application and practical results, various data can be accumulated, leading to suggested values for parameters and hence simplifying the guideline for designers. This is particularly relevant in steps 3 and 4 below.

7.6.1 Proposed design guideline

For a given floor with specified usage, indicating acceleration limit and loading type, it is possible to follow a few steps and arrive at a suitable plywood TMD system, which can be used to reduce the vibrations of the floor. These steps can be followed as below for heeldrop or walking excitations:

step 1 Adapt the model such that the natural frequency of the primary mass becomes equal to the measured fundamental frequency of the given slab. This is very important, since the boundary

conditions of real slabs can rarely be modelled and their effect on natural frequency cannot easily be predicted. For example, in cases where a slab is supported on edge-beams, the connection between the slab and the beams is such that the boundary condition is between a simply supported and a fixed state. Hence, it is necessary to adapt the model parameters (particularly slab length) to arrive at an *equivalent span*, at which the model fundamental frequency matches that of the measured slab value.

step 2 Establish the type of floor, in terms of its occupancy and usage, and decide on a value of limiting vibration amplitude. Here, the suggested values in table 2.3 (page 15) can be used. Furthermore, by looking at the floor span and type of activity, arrive at some possible loading patterns, including the worst possible case (e.g. several consecutive steps). From these, derive the highest response peak amplitude for the slab, either by assuming successive heeldrops (section 7.4.4), or using one of the methods of section 2.7.1.

step 3 Keeping the TMD damping constant at 3% critical, investigate the slab response due to the worst loading case of step 2, with a range of mass ratios, and arrive at a suitable value for μ.

step 4 Keeping mass ratio constant at the value derived in step 3, investigate the slab response due to a range of TMD damping ratios and arrive at a suitable value for ζ_2.

step 5 Having arrived at optimum values for μ and ζ_2, determine the overall performance of the slab with the TMD system installed, due to worst and normal cases of loading.

step 6 With the derived mass ratio and TMD damping, use table 7.2 to suggest the best plywood TMD configuration and by calculating the mass of the TMD, arrive at a suitable size for the plywood and the mass needed to tune the TMD.

A detailed design example, using the above steps, is given in appendix F for a typical floor slab.